CR-152270

TRW REPORT NO. 30584-6001-RU-00

(NASA-CR-152270) EVALUATION OF THE DISCRETE VORTEX WAKE CROSS FLOW MODEL USING VECTOR COMPUTERS. PART 1: THEORY AND APPLICATION (TRW Defense and Space Systems Group) 102 p HC A06/MF A01 CSCL 01A G3/02

N79-22048

Unclas 25233

EVALUATION OF THE DISCRETE VORTEX WAKE CROSS FLOW MODEL USING VECTOR COMPUTERS

Part I — Theory and Application

F. D. Deffenbaugh

Prepared for
Ames Research Center
Under
CONTRACT NAS2-9579
JANUARY 1979

TRW
DEFENSE AND SPACE SYSTEMS GROUP

TRW REPORT NO. 30584-6001-RU-00

EVALUATION OF THE DISCRETE VORTEX WAKE CROSS FLOW MODEL USING VECTOR COMPUTERS

Part I – Theory and Application

F. D. Deffenbaugh
TRW Defense and Space Systems Group
One Space Park
Redondo Beach, California 90278

Prepared for
NASA/Ames Research Center
Moffet Field, California 94305
and
U.S. Army Missile Research and Development Command
Redstone Arsenal, Alabama 35809
Under
Contract NAS2-9579
January 1979

TRW®
DEFENSE AND SPACE SYSTEMS GROUP

TABLE OF CONTENTS

NOMENCLATURE

$a(t)$	Two dimensional circular cylinder radius, $\frac{d}{2\tilde{a}}\ R(Z)$
$\tilde{a}$	Characteristic length of two dimensional unsteady flow, d/2 for constant afterbodies.
c	Constant in Thwaites shape factor equation, = 5.1.
C_d	Sectional normal force coefficient, $\frac{\text{Normal Force Per Unit Length}}{q_\infty\ d}$
C_ℓ	Sectional side force coefficient, $\frac{\text{Side Force Per Unit Length}}{q_\infty\ d}$
CN	Normal force coefficient, $N/q_\infty\ S$
CY	Side force coefficient, $Y/q_\infty\ S$
C_{m_o}	Pitching moment about the nose, $M/q_\infty\ S\ell$
C_m	Pitching moment about $(0, 0, \lambda)$
C_{n_o}	Yawing moment about the nose, $MY/q_\infty\ S\ell$
C_n	Yawing moment about $(0, 0, \lambda)$
C_{p3D}	Three dimensional coefficient of pressure, $P-P_\infty/q_\infty$
C_p	Two dimensional coefficient of pressure, $p-p_\infty/q$
C_D	Two dimensional drag coefficient, $D/2\tilde{a}q$
C_L	Two dimensional lift coefficient, $L/2\tilde{a}q$
d	Maximum body diameter
D	Drag
f	Fineness ratio, ℓ/d
ℓ	Body length

m	Distance from cylinder surface at which vortices are introduced into the outer flow.
M	Pitching moment
N	Normal force
P	Three dimensional pressure
q_∞	Free Stream dynamic pressure, $1/2\rho V^2$
q	Cross flow dynamic pressure, $1/2\rho U^2$
R	Three dimensional body radius
r_c	Vortex core radius
S	Frontal area, $\pi d^2/4$
t	Nondimensional time, $Ut^*/\tilde{a}$
U	Cross flow velocity, V sin α
V	Free stream velocity
W	Axial component of free stream velocity, V Cos α
[u, v]	Boundary layer polar velocity components
$[\bar{u}, \bar{v}]$	Cartesian velocity components
$[u_\theta , v_r]$	Polar velocity components
$[u_o, v_o]$	Polar velocity components at the cylinder surface
[X, Y, Z]	Three dimensional coordinate system, Z positive along the axis from the missile nose.
[x, y]	Two dimensional coordinate system
$[r, \theta]$	Two dimensional polar coordinate system

GREEK

α	Angle of attack
Γ	Circulation
λ	Moment arm, $\frac{\text{moment center distance from nose}}{\ell}$

ε	Coalescence radius
ρ	Density
σ	Vortex strength factor
Φ	Potential function
Ψ	Stream function
ω	Vorticity

Sub- and Superscript

$( )^*$	Dimensional
$( )_n$	Point vortex n

1.0 INTRODUCTION AND SUMMARY

The increased performance requirements of current aircraft and missile designs has caused a resurgence of interest in the aerodynamics of bodies at high angles of attack. In the past most aerodynamic design considerations were for angles of attack less than about 30 degrees where either linear thoery applied (α < 5-7°) or the vortex formations due to boundary layer separation were symmetric and could be adequately handled using available empirical theories. New missile and aircraft designs, however, require consideration of angles of attack up to 180 degrees. Asymmetric vortex development for angles of attack greater than about 30 degrees require techniques for predicting the resulting side forces and moments.

Once flow separation occurs on the lee side of an aerodynamic body the assumptions of inviscid flow and linearized theory are invalid and the only general approach is to solve the Navier-Stokes equations. The numerical solution of the three dimensional Navier-Stokes equations is not at hand for general missile or aircraft shapes.

Other approaches to the problem must be sought for the present. One alternative to solving the full equations of motion entails the use of the viscous cross flow analogy. It was noted by early investigators that for angles of attack where the flow is assumed to be steady, if the flow is viewed in a cross flow plane, it appears similar to that of the time-development of flow behind a two-dimensional circular cylinder started impulsively from rest. This similarity is the basis of the viscous cross flow analogy in which the flow field and forces and moments on a missile are predicted from the analogous two dimensional time-dependent cylinder flow. Virtually all of the existing methods for predicting the aerodynamic characteristics of missile configurations at high angle of attack are based on the use of the viscous cross flow analogy. The methods have met with varying degrees of success.

On the simplest level, the steady state value of cylinder drag suitably corrected for Mach number and Reynolds number effects is used

to compute the normal force distribution. This procedure was initially proposed by Allen (1) but has been extended by Jorgensen (2, 3, 4) and by Saffel (5) who have applied it from subsonic to supersonic flow for bodies of noncircular cross section, for angles of attack up to 180 degrees, and for wing-body-tail configurations. Thompson (6) has taken the analogy one step further and uses Sarpkays's (7) experimental impulsive flow circular cylinder data to represent the viscous contribution to normal force. Correction tables allow for Mach number, effect of nose shape, and transition from laminar to turbulent flow to be accounted for.

The most recent cross flow models are those which replace the separated shear layer with a number of free point vortices which are allowed to roll up to form a concentrated vortex. Angelucci (8) and Marshall and Deffenbaugh (9) used this model for symmetric shedding. Wardlaw (10) and Deffenbaugh and Koerner (11) have extended the work to include asymmetric vortex development.

If a large number of point vortices is used to model the wake computer time can become prohibitive. Only a limited number of test cases have been run using a large number of point vortices at high angles of attack for medium fineness ratio bodies ($f \sim 10.0$).

The objective of the current program is to modify the discrete vortex wake method of Reference (11) to efficiently compute the aerodynamic forces and moments on high fineness ratio bodies. The approach is to increase computational efficiency by structuring the program to take advantage of new computer vector software and by developing new algorithms when vector software can not efficiently be used.

An efficient program was written and substantial time savings achieved. However, greater time savings were realized by using efficient FORTRAN programming techniques and by developing new algorithms than by vectorization. Several test cases were run for fineness ratios up to $f = 16.0$ and angles of attack up to 50 degrees. Prior to running the test cases a parametric investigation was carried out on an ogive nose fineness ratio, $\ell_n/d = 2.598$, afterbody fineness ratio, $\ell/d = 7.754$, body. The parameters varied involved numerical and empirical parameters

used in the discrete vortex wake method. The results clearly point out limits of the method and its advantages and will be useful to anyone using this or similar methods involving discrete vortex wake approximations.

2.0 TIME DEPENDENT VISCOUS CROSS FLOW

For aerodynamic bodies at small angles of attack, the boundary layer remains attached except in the base region. For this situation, the boundary layer may be ignored allowing for an inviscid flow approximation and for slender bodies, application of linearized theory. For higher angles of attack regions of vorticity caused by flow separation along the body form on the lee side. Depending on the angle of attack these body vortices may be symmetric or asymmetric. Asymmetric vortex development can lead to large side forces and is currently the problem of most interest.

An empirical method known as the cross flow analogy has been in use for several years and forms the basis for most of the high angle of attack prediction techniques used today. The difference in cross flow methods lie in the determination of the cylinder lift and drag coefficients. In the present study the time dependent flow about the circular cylinder is determined by coupling an inner boundary layer solution with an outer potential flow solution which models the wake using a large number of discrete vortices.

2.1 CROSS FLOW TRANSFORMATIONS

The geometry transformations for the cross flow analogy are obtained by considering the transformation

$$(X^*, Y^*, Z^*, T^*) = (x^*, y^*, z^* + W\,t^*, t^*) \qquad (2\text{-}1)$$

and considering the flow in the $z^* = 0$ plane. The basic cross flow assumption is that the flow in the X^*, Y^* plane of the body at some Z^* is equivalent to the flow development at time t^* around a two dimensional circular cylinder of radius where

$$t^* = Z^*/W \qquad (2\text{-}2)$$

(from (2-1) taking $z^* = 0$.).

If the following nondimensional variables are defined

$$Z = Z^*/\ell, \qquad a = a^*/\tilde{a}, \qquad R = 2R^*/d, \qquad t = \frac{Ut^*}{\tilde{a}}$$

where U is the cross flow velocity ($U = V \cos \alpha$), ℓ is body length, d is maximum body diameter, and $\tilde{a}$ is a characteristic length of the two dimensional problem, then the basic cross flow equations become

$$t = Z \frac{\ell}{\tilde{a}} \tan \alpha \tag{2-3}$$

$$a(t) = \frac{d}{2} R(Z) \tag{2-4}$$

For most missile shapes $\tilde{a}$ may be defined as d/2. However, for some shapes such as an ellipsoid which have decreasing afterbody diameters it may be more convenient to choose $\tilde{a}$ as an average of the body radius, $\tilde{a} = \frac{1}{\ell} \int_0^{\ell} R^* (Z^*) \, dZ^*$.

2.2 FORCE TRANSFORMATIONS

The normal force, N, and pitching moment, M, on the three dimensional body of revolution are to be obtained by integration of the normal force per unit length dN/dZ* over the body length, where dN/dZ* is assumed to be the same as the cross flow drag D(t*) on the two dimensional cylinder for t* = Z*/W. Similarily the side force, Y, and yawing moment, MY, are obtained by integration of the side force per unit length dY/dZ*, which is taken as equal to the cylinder lift, L(t* = Z*/W).

The normal and side force acting on the body are then,

$$N = \int_0^{\ell} \frac{dN}{dZ^*} \, dZ^* \tag{2-5a}$$

$$Y = \int_0^{\ell} \frac{dY}{dZ^*} \, dZ^* \tag{2-5b}$$

and the pitch and yaw moments about some moment center $(X^*, Y^*, Z^*) = (0, 0, \lambda\ell)$ are:

$$M_\lambda = \int_0^\ell \left(Z^* + R^* \frac{dR^*}{dZ^*}\right) \frac{dN}{dZ^*} dZ^* + \lambda\ell N \qquad (2\text{-}6a)$$

$$MY_\lambda = \int_0^\ell \left(Z^* + R^* \frac{dR^*}{dZ^*}\right) \frac{dY}{dZ^*} dZ^* + \lambda\ell Y \qquad (2\text{-}6b)$$

If the coordinates are non-dimensionalized as in Section 2.1 and the forces and moments are non-dimensionalized as:

$$C_d(Z) = \frac{dN/dZ^*}{1/2\rho V^2 d} \qquad (2\text{-}7a)$$

$$C_\ell(Z) = \frac{dY/dZ^*}{1/2\rho V^2 d} \qquad (2\text{-}7b)$$

$$CN = \frac{N}{1/2\rho V^2 S} \qquad (2\text{-}8a)$$

$$CY = \frac{Y}{1/2\rho V^2 S} \qquad (2\text{-}8b)$$

$$C_{m_o} = \frac{M}{1/2\rho V^2 S\ell} \qquad (2\text{-}9a)$$

$$C_m = C_{m_o} + \lambda CN \qquad (2\text{-}9b)$$

$$C_{n_o} = \frac{MY}{1/2\rho V^2 S\ell} \qquad (2\text{-}9c)$$

$$C_n = C_{n_o} + \lambda CY \qquad (2\text{-}9d)$$

where S is the frontal area $S = \pi d^2/4$, then the force and moment coefficients become,

$$CN = \frac{4f}{\pi} \int_0^1 C_d \, dZ \tag{2-10a}$$

$$CY = \frac{4f}{\pi} \int_0^1 C_\ell \, dZ \tag{2-10b}$$

$$C_m = \left[\frac{-4f}{\pi}\int_0^1 \left(Z + \frac{R}{4f^2}\frac{dR}{dZ}\right) C_d \, dZ\right] + \lambda CN \tag{2-11a}$$

$$C_n = \left[-\frac{4f}{\pi}\int_0^1 \left(Z + \frac{R}{4f^2}\frac{dR}{dZ}\right) C_\ell \, dZ\right] + \lambda CY \tag{2-11b}$$

where f is the fineness ratio, ℓ/d.

The time dependent lift and drag on the two dimensional circular cylinder are:

$$D(t^*) = \int_0^{2\pi} p^* \cos\Theta \, a^*(t^*) \, d\Theta + \int_0^{2\pi} \tau^* \sin\Theta \, a^*(t) \, d\Theta \tag{2-12a}$$

$$L(t^*) = -\int_0^{2\pi} p^* \sin\Theta \, a^*(t^*) \, d\Theta + \int_0^{2\pi} \tau^* \cos\Theta \, a^*(t) \, d\Theta \tag{2-12b}$$

Introducing the non-dimensional quantities,

$$C_p = \frac{p^* - p^*_\infty}{1/2 \, \rho \, U^2}, \quad p = \frac{p^*}{1/2 \, \rho \, U^2}, \quad \tau = \frac{\tau^*}{1/2 \, \rho \, U^2}$$

and defining lift and drag coefficients as,

$$C_D = \frac{D}{1/2\ \rho\ U^2\ 2\tilde{a}} \tag{2-13a}$$

$$C_L = \frac{L}{1/2\ \rho\ U^2\ 2\tilde{a}} \tag{2-13b}$$

gives,

$$C_D = 1/2 \int_0^{2\pi} C_p \cos\theta\ a\ (t)\ d\theta + 1/2 \int_0^{2\pi} \tau \sin\theta\ a(t)\ d\theta \tag{2-14a}$$

$$C_L = -\ 1/2 \int_0^{2\pi} C_p \sin\theta\ a(t)\ d\theta + 1/2 \int_0^{2\pi} \tau \cos\theta\ a(t)\ d\theta \tag{2-14b}$$

Now, cross flow analogy assumes that at $t^* = Z^*/W$

$$\frac{dN}{dZ^*} = D\ (t^*) \tag{2-15a}$$

$$\frac{dY}{dZ^*} = L\ (t^*) \tag{2-15b}$$

or in non-dimensional form the basic cross flow analogy force transformations are

$$\boxed{C_d\ (Z) = \frac{2\tilde{a}}{d} \sin^2\alpha\ C_D\ (t)} \tag{2-16a}$$

$$\boxed{C_\ell\ (Z) = \frac{2\tilde{a}}{d} \sin^2\alpha\ C_L\ (t)} \tag{2-16b}$$

If the three dimensional pressure coefficient is defined as

$$C_{p3D} = \frac{P^*_{3D} - P^*_\infty}{1/2\ \rho\ V^2} \tag{2-17}$$

and shear stress is neglected,then the sectional normal force coefficient is

$$C_d(Z) = 1/2 \int_0^{2\pi} C_{p3D} \cos\theta \, R(Z) d\theta \qquad (2\text{-}18)$$

The two dimensional analog, neglecting shear and rewritten here for convenience is

$$C_D(t) = 1/2 \int_0^{2\pi} C_p \cos\theta \, a(t) \, d\theta \qquad (2\text{-}19)$$

Now since the drag and sectional force coefficient are related as in equation 2-16a the correspondence between two dimensional unsteady and three dimensional pressure is

$$C_{p3D} = \frac{2\tilde{a}}{d} C_p \sin^2\alpha \qquad (2\text{-}20)$$

The two dimensional unsteady flow solution is given in the next section where it is shown that with the present formulation the above relationships between pressures differ by a additive constant when a(t) is varying, ie., on the missile nose.

3.0 DISCRETE VORTEX WAKE (DVW) CROSS FLOW

The problem is to find the flow field induced by a circular cylinder of time-varying radius in a uniform stream of a viscous incompressible fluid. The time dependent lift and drag on the cylinder will be applied as in Section 2.0 to predict the forces and moments on a three dimensional body of revolution.

The flow field is that of a uniform flow with no body present for $t < 0$. At $t = 0$ a circular body appears at the origin and then grows in time, and in most cases (corresponding to typical missile shapes with cylindrical afterbodies) finally reaches a constant value. During the initial stages a boundary layer is formed on the cylinder. At later times the boundary layer separates from the cylinder feeding vorticity into the wake. Initially two symmetric regions of vorticity form behind the cylinder. Eventually these vortices become unstable, one breaks away and flows downstream initiating the Karman vortex shedding process.

3.1 PROBLEM APPROACH

The basic solution technique is to treat the problem of the impulsively started cylinder by assuming that for high Reynolds numbers the flow may be divided into a region of viscous inner flow near the cylinder described by a boundary layer and a rear shear layer, and a region of essentially inviscid outer flow elsewhere. The outer flow consists of the usual potential flow about a circular cylinder plus a wake region. The wake region is modeled by adding to the usual circular cylinder potential flow (vortex, uniform flow, and doublet) the potential flow induced by a set of point vortices. The point vortices represent the vorticity introduced into the wake from the separating boundary layer and rear shear layer. Since ideal point vortices have infinite velocities at their centers it is necessary to include in the model some kind of vortex core inside which the ideal

point vortex velocity is modified. This then is the discrete vortex wake (DVW) model.

In the following sections the basic equations for the discrete vortex wake model are presented. Except for the unsteady integral momentum boundary layer solution, most of the theory presented has been previously detailed in Ref. (9). The equations are briefly rewritten here for completeness and to accompany the computer program users manual which is a separate volume of this report.

3.2 OUTER FLOW

The outer flow is defined as the inviscid irrotational flow outside of the boundary layer and rear shear layer. The exact equations which govern the outer flow are

$$\frac{\partial \omega}{\partial t} + \underset{\sim}{u} \cdot \nabla \omega = 0 \tag{3-1a}$$

$$\underset{\sim}{u} = \hat{k} \times \nabla \Psi \tag{3-1b}$$

$$\nabla^2 \Psi = \omega \tag{3-1c}$$

The discrete vortex method approximates a solution to equations (3-1) by replacing the continuous vorticity distribution ω by a finite sum of N delta functions such that

$$\omega(\underset{\sim}{x}) = \sum^{N} \Gamma_n \, \delta(\underset{\sim}{x} - \underset{\sim}{x}_n(t)) \tag{3-2}$$

The velocity field is then found by summing the velocity field of the individual point vortices. To account for the presence of the circular cylinder, image vortices are included. Vortex motion is accomplished by integrating the equations

$$\frac{d\Gamma_n}{dt} = 0 \tag{3-3}$$

$$\frac{d\underset{\sim}{x}_n}{dt} = \underset{\sim}{u}_n \qquad (3\text{-}4)$$

where $\underset{\sim}{u}_n$ is the velocity induced by the distribution (3-2) at the discrete point vortex location $\underset{\sim}{x}_n$. The self induced velocity of the point vortex is neglected.

Of particular importance is the relationship between the solution of Equations (3-2, 3-3, and 3-4) and the exact solution of Equations (3-1). As pointed out by Saffman (12) it is not clear that the solution of the discrete vortex method converges to the exact solution for fixed N as $t \to \infty$. Although, as Saffman mentions, Dushane (13) proved under restrictive conditions that a form of the discrete vortex method converges in some form to the solution of Equations (3-1) for fixed t as $N \to \infty$.

For practical uses of the method, i.e., fixed N and t, confidence in the method depends on comparison with exact solutions and in some cases comparison with experiment.

The complex potential for a circular cylinder with time dependent radius in the presence of a set of discrete vortices is

$$w = \Phi + i\Psi = z + \frac{a^2}{z} - a\dot{a}\,\ell n\, z + \frac{i\Gamma_o}{2\pi}\,\ell n\,\left(\frac{z}{a}\right)$$

$$+ i \sum_{n=1}^{N} \frac{\Gamma_n}{2\pi} \left[\frac{(z-z_n)z}{z - \dfrac{a^2 z_n}{|z_n|^2}}\right] z_n \qquad (3\text{-}5)$$

where

$$z = x + iy = re^{i\theta} \qquad (3\text{-}6a)$$

$$z_n = x_n + iy_n = \ell_n e^{i\theta_n} \qquad (3\text{-}6b)$$

$$z - z_n = (x - x_n) + i(y - y_n) = r_{1n} e^{i\theta_{1n}} \qquad (3\text{-}6c)$$

$$z - \frac{a^2 z_n}{|z_n|^2} = \left[x - \frac{a^2 x_n}{\ell_n^2}\right] + i\left[y - \frac{a^2 y_n}{\ell_n^2}\right] = r_{2n} e^{i\theta_{2n}} \quad (3\text{-}6d)$$

On the cylinder surface $z = a$, $r_{2n} = a r_{1n}/\ell_n$, and $\Psi = 0$.

The coordinate system is shown in Figure 3-1. The cartesian components of velocity ($\bar{u}$, $\bar{v}$) and the tangential and radial velocity components (u_θ, v_r) may be obtained by differentiating (3-5)

$$\frac{dw}{dz} = -\bar{u} + i\bar{v} = e^{-i\theta}\,(-v_r + iu_\theta) \quad (3\text{-}8)$$

The cartesian components are

$$-\bar{u} + i\bar{v} = 1 - \frac{a^2(x^2 - y^2 - 2ixy)}{r^4} - \frac{a\dot{a}(x - iy)}{r^2} + \frac{i\Gamma_o}{2\pi}\frac{(x - iy)}{r^2}$$

$$+ \sum_{n=1}^{N} \frac{\Gamma_n}{2\pi}\left\{\frac{(y - y_n) + i(x - x_n)}{r_{1n}^2} - \frac{\left(y - \frac{a^2 y_n}{\ell_n^2}\right) + i\left(x - \frac{a^2 x_n}{\ell_n^2}\right)}{r_{2n}^2}\right.$$

$$\left. + \frac{y + ix}{r^2}\right\} \quad (3\text{-}9)$$

The polar velocity components evaluated at the cylinder surface

$$u_o = u_\theta\ (r = a,\ \theta)$$

$$v_o = v_r\ (r = a,\ \theta)$$

become,

$$-v_o + iu_o = -\dot{a} + i\,2\sin\Theta + \frac{i\Gamma_o}{2\pi} + i\sum_{n=1}^{N}\frac{\Gamma_n}{2\pi}\left\{\frac{a^2 - \ell_n^2}{a r_{1n}^2} + \frac{1}{a}\right\} \quad (3\text{-}10)$$

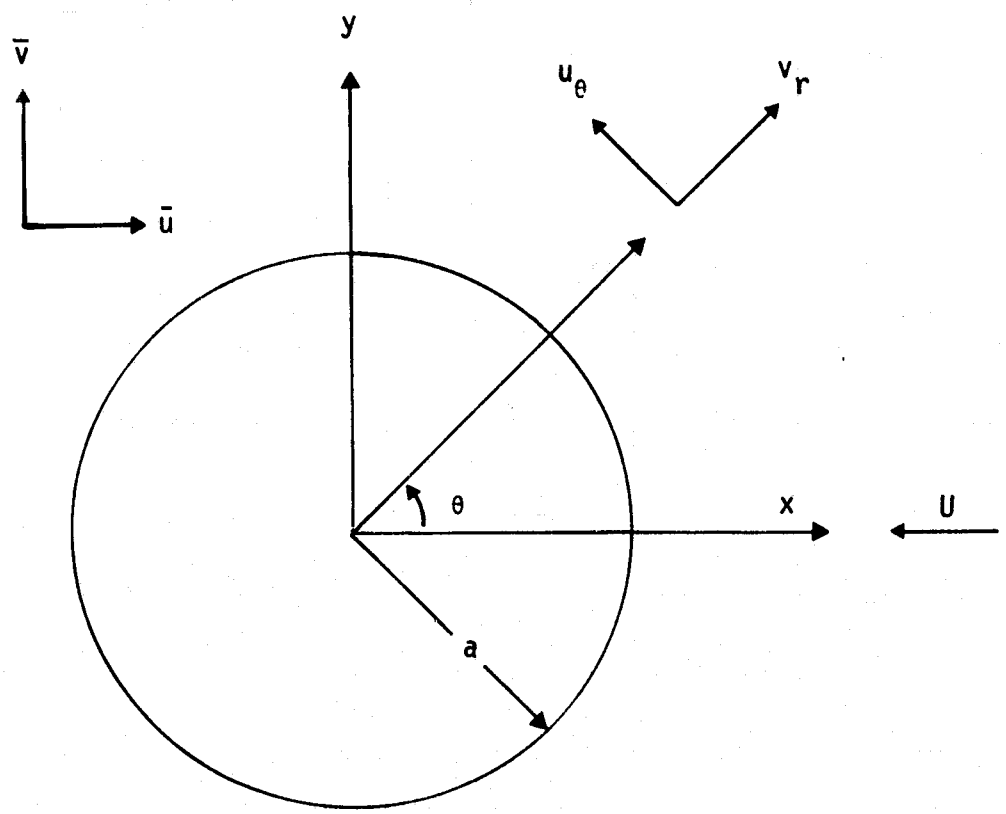

FIGURE 3-1 COORDINATE SYSTEM

For completeness equation 3-5 includes a circulation term Γ_o. This is essentially an additional point vortex placed at the cylinder center. For bodies with sharp trailing edges Γ_o is usually chosen to satisfy the Kutta condition. For the case of the circular cylinder where no sharp edge exists other physical considerations should determine the value of Γ_o.

However, to date there is no clear consensus on how to determine Γ_o for this problem. The approach in the present work is to choose $\Gamma_o = 0.0$, but to leave the capability in the computer program for future use.

Pressure

The surface pressure coefficient is determined from the time dependent Bernoulli equation. In non-dimensional form the Bernoulli equation is

$$2\Phi_{,t} + u_\theta^2 + v_r^2 + p = 2F(t) \tag{3-11}$$

where from (3-5)

$$\Phi = \cos\Theta \left[r + \frac{a^2}{r}\right] - a\dot{a}\,\ell n\, r - \frac{\Gamma_o \Theta}{2\pi} - \sum_{n=1}^{N} \frac{\Gamma_n}{2\pi}\left\{\Theta_{1n} - \Theta_{2n} + \Theta - \Theta_n\right\} \tag{3-12}$$

such that

$$\Phi_{,t} = \frac{2a\dot{a}\cos\theta}{r} - \frac{d(a\dot{a})}{dt}\ell n\, r - \frac{\dot{\Gamma}_o \theta}{2\pi} - \sum_{n=1}^{N} \frac{\Gamma_n}{2\pi}\left\{\dot{\theta}_{1n} - \dot{\theta}_{2n} - \dot{\theta}_n\right\} \tag{3-13}$$

where

$$\dot{\theta}_{1n} = \frac{-\dot{y}_n(x - x_n) + \dot{x}_n(y - y_n)}{r_{1n}^2}$$

$$\dot{\Theta}_{2n} = \left\{ - \frac{d}{dt}\left(\frac{a^2 y_n}{\ell_n^2}\right) + \frac{d}{dt}\left(\frac{a^2 x_n}{\ell_n^2}\right) \cdot \frac{y - a^2 y_n}{\ell_n^2} \right\} \frac{1}{r_{2n}^2}$$

$$\dot{\Theta}_n = \frac{\dot{y}_n x_n - \dot{x}_n y_n}{\ell_n^2} \tag{3-14}$$

If the pressure coefficient on the surface $C_p = p - p_\infty$ and from (3-11)

$$p_\infty = 2F(t) - 1.0 - \lim_{r \to \infty} 2\Phi_{,t}\ (r, \theta, t) \tag{3-15}$$

where

$$\Phi_{,t}(r \to \infty, \theta, t) = - \frac{d}{dt}(a\dot{a}) \lim_{r \to \infty} \ell n\ r + \sum_n \frac{\Gamma_n}{2\pi}\ \dot{\theta}_n \tag{3-16}$$

The pressure coefficient becomes

$$C_p = 4\ \dot{a}\ \text{Cos}\ \theta - \frac{d}{dt}(a\dot{a})\ \ell n\ a - 2 \sum_{n=1}^{N} \frac{\Gamma_n}{2\pi}\ \left\{\dot{\theta}_{1n} - \dot{\theta}_{2n}\right\}$$

$$- u_o^2 + 1.0 + 2\ \frac{d}{dt}(a\dot{a}) \lim_{r \to \infty} \ell n\ r \tag{3-17}$$

For times where $\dot{a} \neq 0$, ie., on the missile nose, the last term in (3-17) precludes an absolute determination of C_p. The computations of C_p in the present program do not include the log terms in (3-17). On the nose then, C_p is only qualitative, on the missile after body ($\dot{a} = 0$) C_p is computed exactly.

Lift and Drag

In the present program lift and drag are obtained by numerically (Simpson's Rule) integrating the pressure coefficient distribution around the cylinder. The additive constant in C_p for $\dot{a} \neq 0$ is integrated out and does not effect lift and drag. Lift and drag due to shear stress are small compared to the pressure forces and are ignored in the present formulation.

A consequence of using Equation (3-17) to compute the pressure is the occurrence of spikes in the distribution due to discrete vortices being too near the surface point at which the pressure is being calculated. A core radius is employed to account for the singular nature of the point vortex approximation. In the present model point vortices

within a radius, $r_c = .05$, of the point at which the pressure is being computed are ignored in the computation. Even with this use of a core radius, spikes in the pressure coefficient distribution may occur. The discrete vortices, especially the ones introduced from the rear shear layer, may tend to cluster in regions of low velocity on the rear of the cylinder. This concentration of vorticity which is in effect a small secondary vortex will cause a spike. Also in examining the results, it appears that the time derivative of the potential term is a larger contributor to the pressure than is the surface velocity.

Experimental pressure data is usually time-averaged and any sharp pressure peaks in the data are averaged out. Instantaneous pressure data, Ref. (14), may exhibit pressure peaks which as in numerical models may be a consequence of small eddies in close proximity to the cylinder surface. The numerical results could be filtered or smoothed before the pressure is integrated. The difficulty which then arises is how much of the spike is "real" and how much is not. In the present work the computed pressure distribution is not smoothed. As a result the lift and drag may exhibit high frequency variations, See Figure 3-2. However, the forces will average out for frequencies on the order of the vortex shedding frequency.

Vortex Motion

Equation (3-4) is integrated using a Euler scheme to determine the development of the discrete vortex wake in time. Thus at each timestep, t_k, a new vortex distribution is calculated at $t_{k+1} = t_k + \Delta t_k$ as

$$x_n(t_{k+1}) = x_n(t_k) + u(x_n, y_n, t_k) \cdot \Delta t_k \qquad (3\text{-}18a)$$

$$y_n(t_{k+1}) = y_n(t_k) + v(x_n, y_n, t_k) \cdot \Delta t_k \qquad (3\text{-}18b)$$

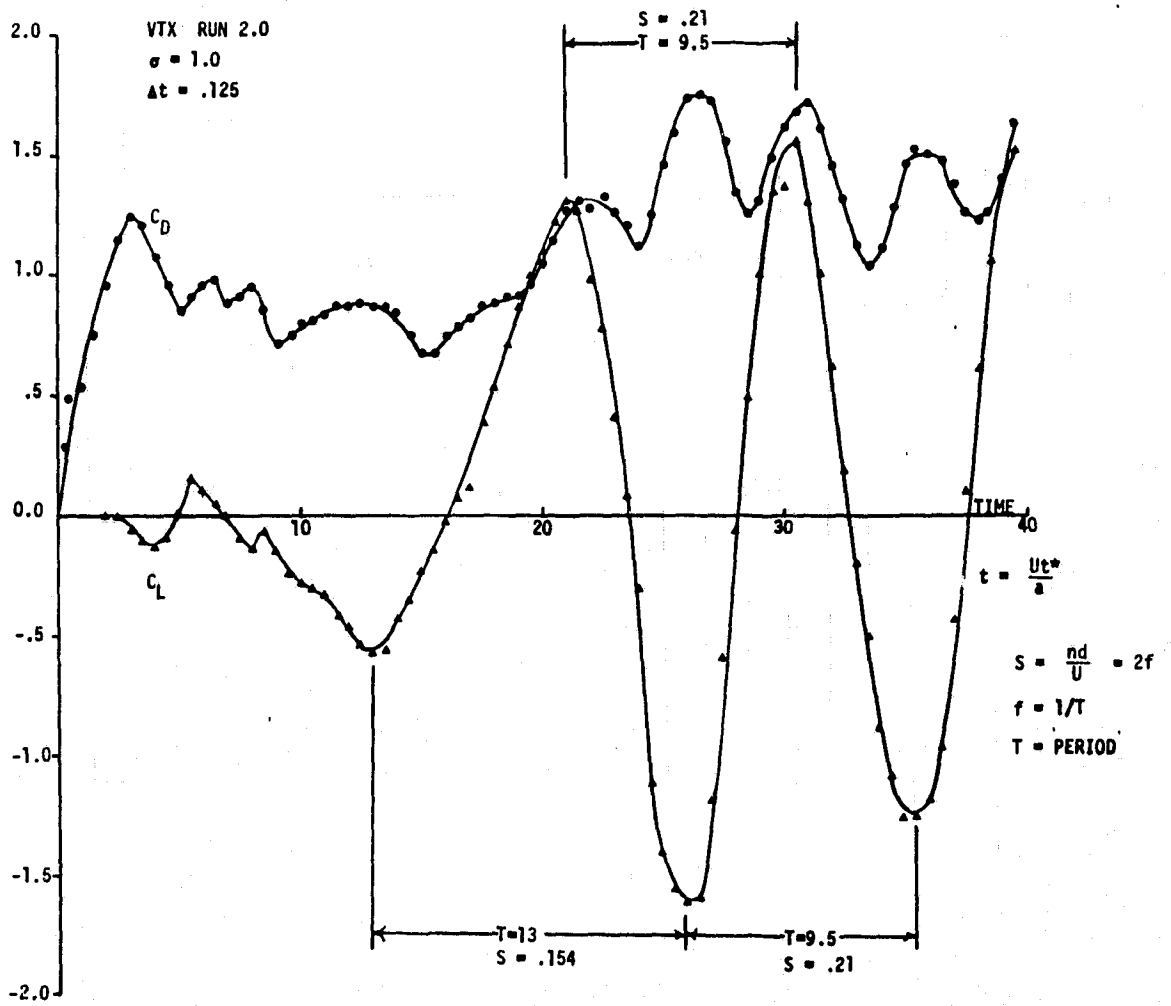

FIGURE 3-2 TIME DEPENDENT LIFT AND DRAG OF A CONSTANT RADIUS CYLINDER

On occasion when a discrete vortex is close to the cylinder surface the Euler scheme will allow the new discrete vortex position to be inside the cylinder surface. To avoid this each new discrete vortex position is checked and when found to be inside the cylinder is moved to a point (r_n = a + .001, θ_n (t_k)) just outside the cylinder. The integration step is then completed using only the tangential component of the original discrete vortex velocity.

Vortex Birth

Discrete point vortices are introduced into the flow at the boundary layer and rear shear separation points θ_s, and θ_s^r respectively. The determination of the separation points is discussed in the next Section (3.3). The vorticity flux across the boundary layer at θ_s is

$$\frac{\partial \Gamma}{\partial t} = \int_o^\infty \omega u dr = \int_o^\infty \frac{\partial u'}{\partial r'} u' dr' = \frac{u_o^2}{2} \tag{3-19}$$

where the prime quantities denote inner boundary layer variables. The vorticity flux out of the boundary layer in a time-step, Δt_k, is summed into a point vortex of strength

$$\Gamma_n = \Delta t_k \frac{\partial \Gamma}{\partial t} \tag{3-20}$$

The point vortex is placed in the outer flow at the separation angle at some distance, m, from the cylinder surface. Images are created simultaneously to satisfy the condition of zero normal flow at the surface. In the present work, m is chosen so as to satisfy the no slip condition on the cylinder surface. The just born vortex and its images induce a velocity at the surface $u_j = \frac{\Gamma_j}{\pi m}$. With the requirement that u_j be canceled by the outer flow velocity then,

$$m = \frac{\Gamma_j}{\pi u_o} = \frac{\Delta t_k u_o}{2\pi} \tag{3-21}$$

Point vortices are introduced from rear shear layer separation points in the same manner.

The distance from the cylinder surface, m, depends on the timestep Δt. For large Δt, the point vortex may be placed outside of the boundary layer. In keeping with the boundary layer approximation it may be that m should be required to be within the boundary layer thickness. This restriction would limit the choice of Δt. The point vortex, however, could be required to remain within the boundary layer and the no slip condition relaxed. Because the point vortex is in the outer inviscid flow there is no real requirement for no slip to hold.

Vortex Coalescence

Even with the use of large scale computers and vectorized solution techniques, it may be desirable at some point to coalesce two or more vortices into one. In the present method, if the option is desired, two point vortices at (x_i, y_i), (x_j, y_j) of strengths Γ_i, Γ_j are coalesced into one discrete vortex of strength

$$\Gamma_c = \Gamma_i + \Gamma_j \tag{3-22}$$

at position

$$x_c = \frac{(|\Gamma_i|\, x_i + |\Gamma_j|\, x_j)}{(|\Gamma_i| + |\Gamma_j|)} \tag{3-22a}$$

$$y_c = \frac{(|\Gamma_i|\, y_i + |\Gamma_j|\, y_j)}{(|\Gamma_i| + |\Gamma_j|)} \tag{3-23b}$$

when the two vortices are within some specified coalescence radius, ε, ie., when

$$(x_i - x_j)^2 + (y_i - y_j)^2 \leq \varepsilon \qquad (3\text{-}24)$$

Now, if

$$(x_j - x_i)/r \text{ and } (y_j - y_i)/r$$

where

$$r = (x - x_i)^2 + (y - y_i)^2$$

or

$$r = (x - x_j)^2 + (y - y_j)^2$$

are of order $0(\varepsilon)$,
then it can be shown that the coalesced vortex yields a velocity field

$$u_c = (u_i + u_j)\ (1 + 0\ (\varepsilon^2))$$

$$v_c = (v_i + v_j)\ (\ 1 + 0\ (\varepsilon^2)$$

As will be discussed later in the results section, coalescence of the vortices can make a significant difference in the early time development of lift on the cylinder even though the coalescence radius is no greater than $\varepsilon = .1$.

Wake Vortex Stability

The development of the wake will continue to be symmetric until some sort of perturbation is introduced into the numerical scheme so far outlined. The type of perturbation and magnitude of perturbation will have a large effect on the early flow development although an equivalent steady state will be achieved eventually. In the present work the method of perturbation is to reduce the boundary layer discrete vortex strength coming from one side of the cylinder for a short period of time early in the flow development.

Vortex Strength Parameter, σ

In the two dimensional theory all of the vorticity created at a solid body surface must eventually end up in the wake. Experimentally, Fage (15) observed that only about 60% of the vorticity which is generated in the boundary layer is later measurable in the wake. It is generally felt that vorticity from the rear of the cylinder which is opposite in sign to that of the boundary layer coalesces with the boundary layer vorticity and accounts for Fage's observation. Since rear vorticity is accounted for in the present model no further reduction of vorticity should be required or perhaps permitted, at least for the two dimensional case.

For use in the cross flow analogy however a further reduction of vorticity may be necessary. In previous work, Ref. (9), good results were obtained by multiplying the boundary layer strength by a reduction factor $\sigma < 1.0$ such that

$$\Gamma_n = \sigma\Gamma_j$$

where Γ_j is the just born vortex of strength $\Gamma_j = \Delta t \frac{u_o^2}{2}$.

The use of the factor σ in the cross flow analogy is not yet fully understood. So far no theoretical justification for its use has been found. However, if one considers the problem of a three dimensional separation it is not reasonable to expect that all of the vorticity at the separation ends up in the cross flow plane. The vorticity vector in a three dimensional flow has three components. The justification for the use of the two dimensional vortex strength parameter σ may be found in a better understanding of the three dimensional flow separation.

3.3 BOUNDARY LAYER

Governing Equations

The boundary layer equations non-dimensionalized as in the outer flow and written in polar form for an expanding radius circular cylinder in

incompressible flow are

$$(1)\quad \frac{\partial u}{\partial t} + \frac{u}{a^2}\frac{\partial u}{\partial x} + v\frac{\partial u}{\partial y} = \frac{\partial (aU)}{\partial t} + \frac{aU}{a^2}\frac{\partial (aU)}{\partial x} + \frac{\partial^2 u}{\partial y^2} \qquad (3\text{-}25a)$$

$$(2)\quad \frac{1}{a^2}\frac{\partial u}{\partial x} + \frac{\partial v}{\partial y} = \frac{\dot{a}}{a} \qquad (3\text{-}25b)$$

For a cylinder started impulsively from rest the initial conditions are

$$(1)\quad t = 0,\ u = v = 0 \qquad (3\text{-}25c)$$

and the boundary conditions are,

$$(1)\quad y = 0,\ u = v = 0$$

$$(2)\quad y \to \infty,\ u \to aU(x,t) \qquad (3\text{-}25d)$$

Here x and y are coordinates along and normal to the wall.
Equations (3-25) have in the previous work been solved directly using an implicit finite difference technique developed by M. G. Hall (16). The finite difference methods suffers from two aspects. The finite difference method requires a large amount of computer storage and computer time. Secondly, the finite difference method does not allow for oscillation of the separation angles. The discrete vortex wake solution requires only the determination of the separation angles at each timestep. Therefore in past work the finite difference method was replaced by a quasi-steady separation scheme developed by Stratford (17, 18). However, it was still necessary to use the finite difference solution for early times where the boundary layer is unsteady, and for times where $\dot{a} \neq 0$.

The objective of the present work was to increase the efficiency of the discrete vortex wake method through efficient programming techniques, by using "vector" software where ever possible, and by developing new

algorithms. Therefore in the present work a method was developed to predict separation on a changing radius cylinder based on the integral form of the unsteady momentum equations. This method based on the work of Thwaites (19, 20, 21) replaces the finite difference method. For a missile test case with ogive nose 2.59d and 7.727d afterbody at 45° angle of attack the unsteady finite difference solution executed on TRW's CDC6600 in 1207 CPU seconds. The new unsteady integral momentum solution executed in 363 CPU seconds.

Unsteady Integral Momentum Formulation

Multiplying (3-25a) by (aU - u), adding to (3-25b) and integrating with respect to y from o to ∞ yields the integral form of the momentum equations for time dependent radius,

$$\frac{\partial(U_o\delta_1)}{\partial t} + \frac{U_o}{a^2}\frac{\partial U_o}{\partial x}(\delta_1 + 2\delta_2) + \frac{U_o^2}{a^2}\frac{\partial \delta_2}{\partial x} - \frac{\dot{a}}{a}U_o = \left(\frac{\partial u}{\partial y}\right)_o \qquad (3\text{-}26)$$

where $U_o = aU$

and

$$\delta_1 = \int_o^\infty \left(1 - \frac{u}{U_o}\right) dy \equiv \text{Displacement Thickness}$$

$$\delta_2 = \int_o^\infty \frac{u}{U_o}\left(1 - \frac{u}{U_o}\right) dy \equiv \text{Momentum Thickness}$$

The last term on the left side of the equation (3-26) is analogous to a blowing term. Solutions to equation (3-26) based on the assumption of a Pohlhausen velocity profile, i.e.,

$$\frac{u}{U_o} = a\eta + b\eta^2 + c\eta^3 + d\eta^4 \qquad (3\text{-}27)$$

$$\eta = \frac{y}{\delta}$$

may fail for strong blowing or suction because $\frac{u}{U_o}$ may be greater than 1, which Pohlhausen profiles do not permit. In fact, for this problem a Pohlhausen solution was initially tried and did fail.

To circumvent this difficulty a velocity distribution is chosen for which $\frac{u}{U_o}$ must always be ≤ 1. Following the method developed by Thwaites (19), if we consider the velocity distribution given by

$$\frac{y}{\delta_2} = F\left(\frac{u}{U_o}\right)$$

or

$$\frac{y}{\delta_2} = F(s) \quad , \qquad s = \frac{u}{U_o} \qquad (3\text{-}28)$$

where conditions at the boundary are

$$F(0) = 0$$

$$F(1) = \infty \qquad (3\text{-}29)$$

and require that S be monotonic for $0 \leq S < 1$, then equation 3-28 represents a velocity distribution which has no maximum of u/U_o other than unity.

From the definition of momentum thickness it can be shown that the following condition must hold

$$\int_0^\infty (2s - 1)\, F(s)\, ds = 1 \qquad (3\text{-}30)$$

F(s) can be chosen in any way such that the above equation (3-30) is satisfied. The momentum thickness is no longer a function of the shape of the velocity distribution since there are many choices for F(s). This allows velocity distributions to be added simply and without imposing any condition on the momentum thickness, δ_2, ie., (3-30) is satisfied. The idea behind Thwaites method is to add a Blasius profile and a suitable separation velocity distribution. The details are the same as presented by Thwaites (19) and the form of F(s) is

$$\frac{y}{\delta_2} = F(s) = \left[1 - \frac{c\lambda}{6}\left(1 - \frac{\lambda^4}{5}\right)\right] B(s) \qquad (3\text{-}32)$$

$$+ \frac{c}{\lambda}\left[\sqrt{\left(\frac{1-\lambda^2}{2}\right) + \lambda s} - \left(\frac{1-\lambda^2}{2}\right)\right]$$

where B(s) is the Blasius profile and λ a parameter. From (3-28) and (3-32) the following derivatives at the wall are obtained

$$\frac{\delta_2}{U_o}\left(\frac{\partial u}{\partial y}\right)_o = \frac{1-\lambda^2}{j(\lambda)} \qquad (3\text{-}33a)$$

$$\frac{\delta_2^2}{U_o}\left(\frac{\partial^2 u}{\partial y^2}\right)_o = \frac{2c\lambda^3}{j^3(\lambda)}$$

where

$$j(\lambda) = 4.5345\,(1-\lambda^2)\left[1 - \frac{c\lambda}{6}\left(1 - \frac{\lambda^4}{5}\right)\right] + c\lambda \qquad (3\text{-}34)$$

When $\lambda = 0$, $\frac{y}{\delta_2} = B(s)$, the Blasius profile. When $\lambda = 1$, $\left(\frac{\partial u}{\partial y}\right) = 0$ ie., separation occurs. For the above formulation to be complete a value for the constant, c, which appears in equations (3-32), (3-33), and (3-34)

needs to be determined. Thwaites (19) found that for the case of Howarth's linear adverse velocity gradient $U = \beta_o - \beta_1 x$, a choice of $c = 5.1$ resulted in separation of the boundary layer for $\beta_1 x/\beta_o = .120$, ie., the solution obtained by Howarth.

Thwaites applied this method to a variety of steady problems Refs. (19, 20, 21) with suction. In the present work Thwaites method is extended to unsteady flows with a blowing like term. The value of $c = 5.1$ found by Thwaites is retained in the present work.

Having chosen the form of the velocity profile as in (3-32) and defining the quantities

$$H = \delta_1 / \delta_2, \qquad z = \delta_2^2, \qquad \varepsilon = \frac{\delta_2}{U_o} \left(\frac{\partial u}{\partial y} \right)_o$$

Then the integral momentum equation (3-26) can be written after a few pages of algebra as

$$\frac{U_o}{a^2} \frac{\partial z}{\partial x} + \left(H + \frac{2\lambda}{3\left(1 - \frac{\lambda k}{j} \right)} \frac{dH}{d\lambda} \right) \frac{\partial z}{\partial t} = 2\varepsilon + \frac{4c\lambda^3}{j^3} (H + 2) + 2\sqrt{z} \frac{\dot{a}}{a}$$

$$-2z \left[\frac{1}{3\left(1 - \frac{\lambda k}{j} \right)} \frac{dH}{d\lambda} \frac{\lambda}{g} \frac{\partial g}{\partial t} - 2 \frac{1}{U_o} \frac{\partial U_o}{\partial t} \right] \qquad (3\text{-}35a)$$

For the case of impulsive start the initial condition is,

$$\text{I.C.} \qquad t = 0 \; ; \quad z = 0 \quad \text{on } x \qquad (3\text{-}35b)$$

ie., momentum thickness is initially zero.

In equation (3-35) g is a function only of the outer flow ie.,

$$g = \frac{1}{a^2}\frac{\partial U_o}{\partial x} + \frac{1}{U_o}\frac{\partial U_o}{\partial t} \tag{3-36a}$$

$$\frac{\partial g}{\partial t} = \frac{1}{a^2}\frac{\partial^2 U_o}{\partial x\,\partial t} + \frac{1}{U_o}\left[\frac{\partial^2 U_o}{\partial t^2} - \frac{1}{U_o}\left(\frac{\partial U_o}{\partial t}\right)^2\right] - \frac{2\dot{a}}{a^3}\frac{\partial U_o}{\partial x} \tag{3-36b}$$

Now, from eqns (3-33) and evaluating (3-25a) at y = 0

$$\frac{2c\lambda^3}{j^3} = -z\,g \tag{3-37}$$

hence knowing z and g

λ can be found

and H, $\frac{dH}{d\lambda}$, ε, j, and h are all functions of λ, ie.,

$$H = 2.5911\left[1 - \frac{c\lambda}{6}\left(1 - \frac{\lambda^4}{5}\right)\right] + \frac{c\lambda\,(\lambda^2 + 3)}{6} \tag{3-38}$$

$$\frac{dH}{d\lambda} = \frac{c}{6}\left[-2.5911\,(1 - \lambda^4) + \lambda^3(3\lambda + 1) + 3\right] \tag{3-39}$$

$$\varepsilon = \frac{\delta_2}{U_o}\left(\frac{\partial u}{\partial y}\right)_o = \frac{1 - \lambda^2}{j(\lambda)} \tag{3-40}$$

$$j(\lambda) = 4.5345\,(1 - \lambda^2)\left[1 - \frac{c\lambda}{6}\left(1 - \frac{\lambda^4}{5}\right)\right] + c\lambda \tag{3-41}$$

$$k(\lambda) = 4.5345\,(1 - \lambda^2)\left[-\frac{c}{6}\,(1 - \lambda^4)\right] - 2(4.5345)\lambda\left[1 - \frac{c\lambda}{6}\,(1 - \frac{\lambda^4}{5})\right] + c \tag{3-42}$$

Equation (3-35) is quasi-linear partial differential equation, the solution of which may be found by solving the following set of ordinary differential equations.

$$\frac{dx}{dt} = \frac{U_o}{a^2 \left[H + 2h \lambda \frac{dH}{d\lambda} \right]} \tag{3-43a}$$

$$\frac{dz}{dt} = \frac{F_1 + 2\sqrt{z} \frac{\dot{a}}{a} - 2z \left[h \frac{dH}{d\lambda} \frac{\lambda}{g} \frac{\partial g}{\partial t} - \frac{2}{U_o} \frac{\partial U_o}{\partial t} \right]}{H + 2h \lambda \frac{dH}{d\lambda}} \tag{3-43b}$$

$$\frac{dz}{dx} = \frac{F_1 + 2\sqrt{z} \frac{\dot{a}}{a} - 2z \left[h \frac{dH}{d\lambda} \frac{\lambda}{g} \frac{\partial g}{\partial t} - \frac{2}{U_o} \frac{\partial U_o}{\partial t} \right]}{U_o/a^2} \tag{3-43c}$$

where for convenience

$$f = \frac{4c\lambda^3}{j^3} \tag{3-44}$$

$$h = \frac{1.0}{3\left(1 - \frac{\lambda k}{j} \right)} \tag{3-45}$$

and

$$F_1 = 2\varepsilon + (H + 2) \; f \tag{3-46}$$

Equations (3-43) are integrated numerically using a simple Euler scheme. Once z is found as function of x and t then λ is determined from (3-37). Separation occurs at $x = x_s$ when

$$z(x = x_s, t) = \frac{2}{gc^2}$$

ie., when $\lambda = 1$.

Figs. 3-3 and 3-4 present the separation angles calculated using the method just outlined and using the previous finite difference scheme. The separation angle predicted by Thoman, (22) using a Navier-Stokes finite difference solution is presented for comparison. The results for a constant radius cylinder are presented in Fig. 3-3. The boundary layer finite difference and integral momentum methods are in close agreement. Figure 3-4 presents the results for a changing radius cylinder. (Thoman's results are for constant radius). The results in Fig. 2-4 correspond to the rate of change of radius over an ogive nose of fineness ratio 2.598. A constant radius would be reached for this case at a time of $t = 5.0$. The time dependent radius results show that for early times separation is promoted over the constant radius case while for times $t \geq 1.2$ separation may even be prolonged. A possible explanation for this behavior might be found in examining the relationship between the $\frac{1}{a^2}$ terms and the blowing term $-\frac{\dot{a}}{a} U_0$ in equations (3-26) and (3-35) as, a, increases. The dependence of the solution on the relationship between, a, and, $\dot{a}$, has not been investigated in detail in the present work.

Quasi-Steady Separation

Stratford (17, 18) derived a method to determine the separation point of a laminar or turbulent boundary layer from an arbitrary pressure distribution. For laminar flow separation occurs at x when

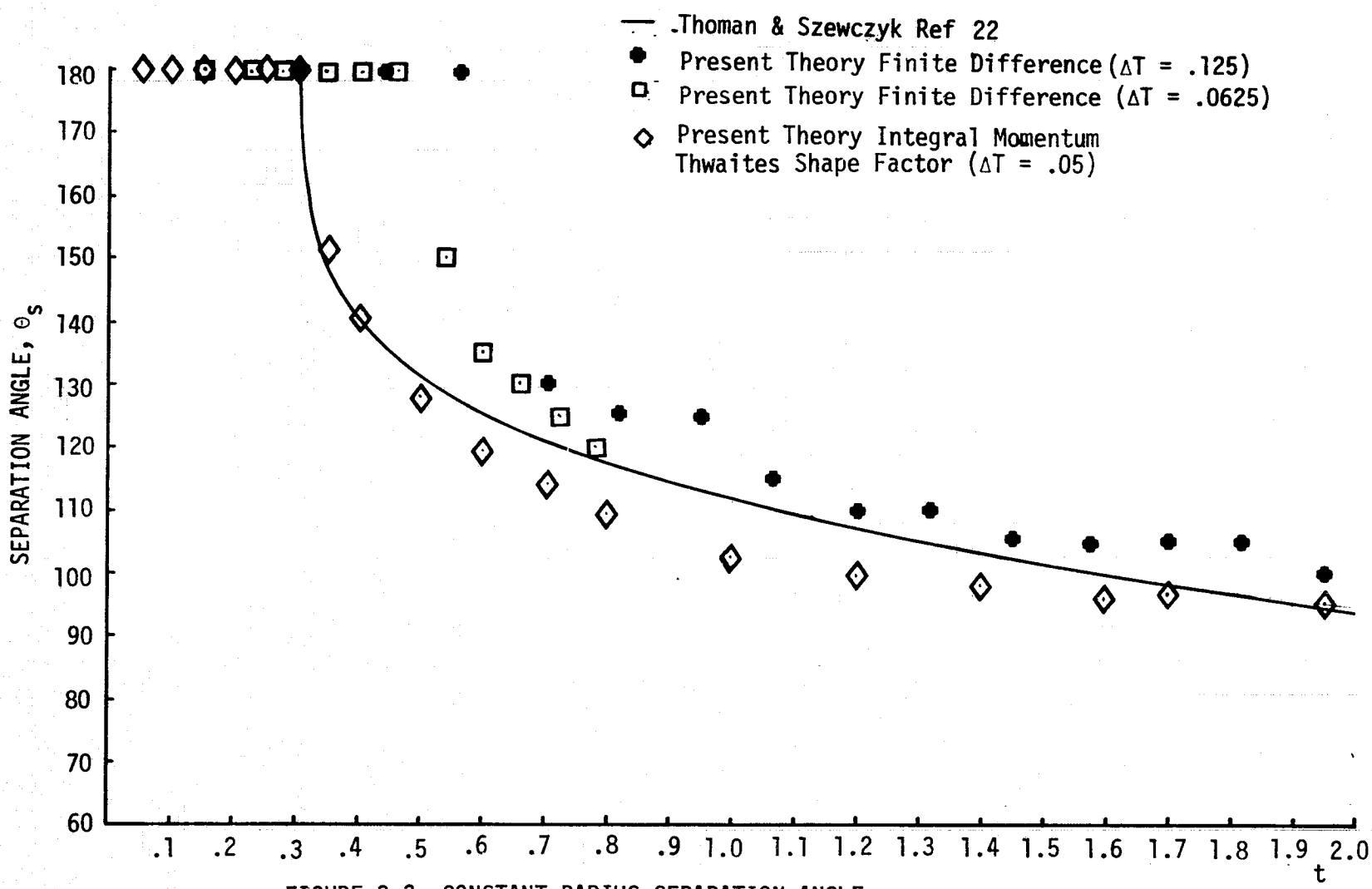

FIGURE 3-3 CONSTANT RADIUS SEPARATION ANGLE

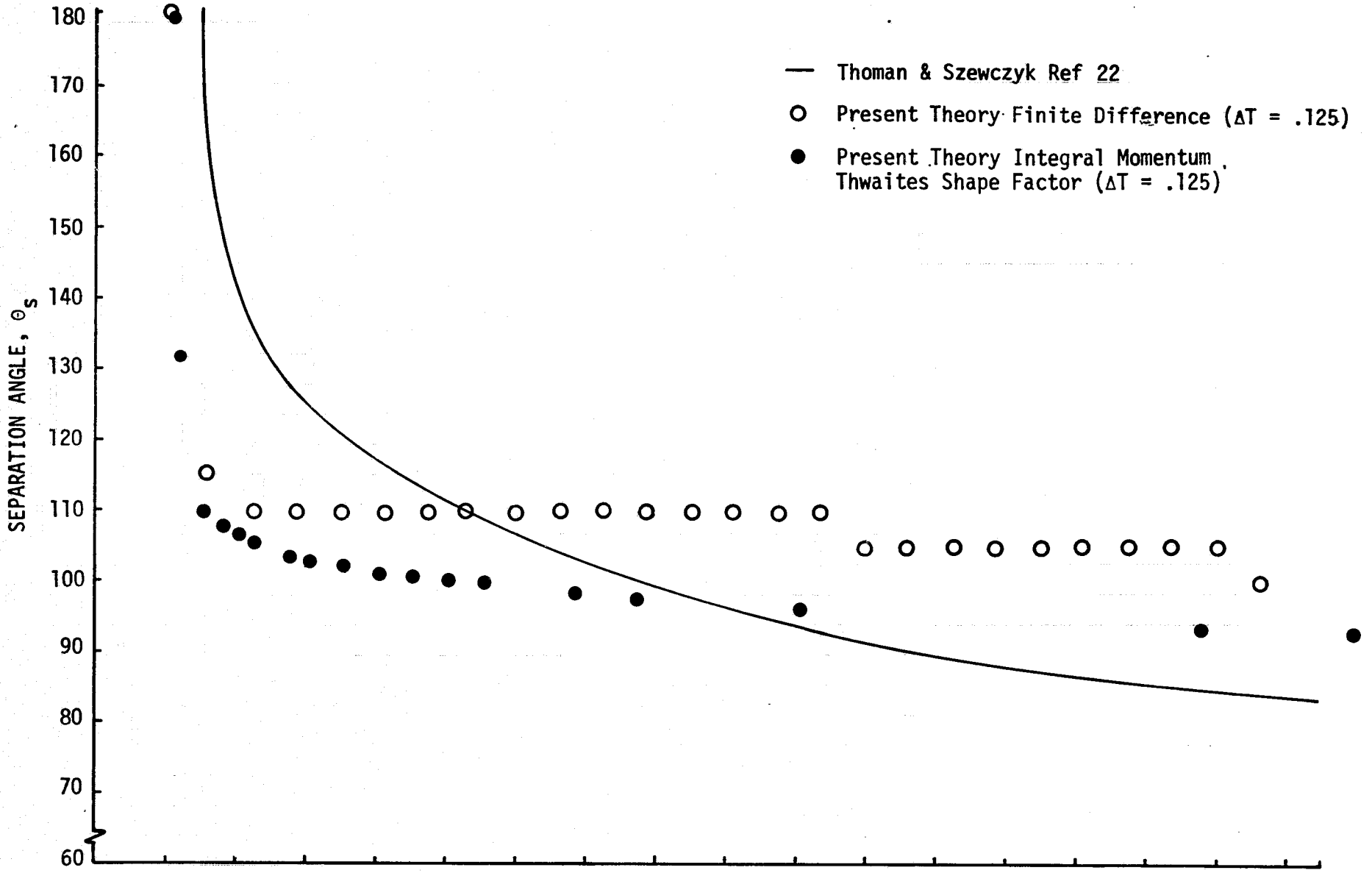

FIGURE 3-4 SEPARATION ANGLE ON N1B1, $\alpha = 45^{o}$

$$\tilde{x}^2 \, C_p(\tilde{x}) \left(\frac{dC_p}{d\tilde{x}} \right)^2 = s_k$$

where the constant $s_k = .14$, and $\tilde{x}$ is an equivalent distance,

$$\tilde{x} = x - x_m - x_s + \int_{x_s}^{x_m} \left(\frac{u}{u_m} \right)^5 dx \qquad (3\text{-}47)$$

which accounts for regions of positive pressure gradient. For turbulent flow separation occurs at x when

$$(2C_p)^{5/4} \quad (\tilde{x} \frac{dC_p}{d\tilde{x}})^{1/2} = 1.06 \, \beta \, (10^{-6} R)^{1/10} \qquad (3\text{-}48)$$

where R = Reynolds number based on local value of equivalent distance, $\tilde{x}$, and peak velocity, u_m, or velocity at transition, u_{tr}, whichever occurs later. The equivalent distance, $\tilde{x}$, accounts for an initial region of favorable pressure gradient and for a boundary layer which is initially laminar. The distance along the surface from $\theta = 0$ to the forward stagnation point is x_s.

$$\tilde{x} = x - x_o - x_s + 38.2(u_o/u_{tr})^{1/8} \, (R_{tr})^{-3/8}$$

$$\left[\int_{x_s}^{x} \left(\frac{u}{u_o} \right)^5 dx \right]^{5/8} (x_{tr})^{3/8} + \int_{x_{tr}}^{x_o} \left(\frac{u}{u_o} \right)^3 dx \qquad (3\text{-}49)$$

where

$$u_o = u_m = u(x_m), \; x_o = x_m, \; x_m > x_{tR}$$

$$u_o = u_{tr} = u(x_{tr}), \; x_o = x_{tr}, \; x_m < x_{tr}$$

The empirical factor chosen by Stratford is $\beta = .73$ and is the value used in the present work. Mendenhall, (23), suggested that a factor $\beta' = \beta \sin \alpha$ be used to account for 3D boundary layer effects.

4.0 VECTORIZATION

Vectorization refers to the organization of individual steps in an algorithm into loop operations on arrays of data. Current vector processors exploit mainly pipelining rather than parallelism to achieve vector speedup over scalar operation.

Pipeline processors consist of high speed arithmetic units which are segmented into a series of serial operations. The idea of vectorization is to perform operations on long vectors (such as C(I) = A(I) + B(I)) so that an element of the vector flows into the pipeline at each clock cycle. A clock cycle is defined as the maximum time it takes for an element to pass through any segment of the pipe. The idea is to keep all segments of the arithmetic unit continually busy on different elements of the vector. Once the pipe is full a result will be produced every clock cycle. In a scalar mode an element would have to traverse the entire pipeline to produce a result. In scalar mode then the operation C(I) = A(I) + B(I) would produce one result every 6 clock cycles (see Figure 4-1) whereas in vector mode 6 results would have been computed.

The discrete vortex wake method involves operations on a large number of point vortices which are essentially vector operations. Most of the computation time is spent operating on these arrays. The present study was aimed at restructuring the current scalar code to take advantage of vector processing capability.

Vector CDC7600

When the CDC7600 is used with the FTN FORTRAN compiler it operates mostly as a sequential machine. However, by making efficient use of certain features of the machine hardware, ie., the functional units, and the instruction stack unit,the CDC7600 can exhibit a limited vector capability. A high speed software vector processing subroutine library was written by R & D Associates (24,25) for use on the NASA AMES CDC7600 computer. When these subroutines are implemented on the CDC7600 it

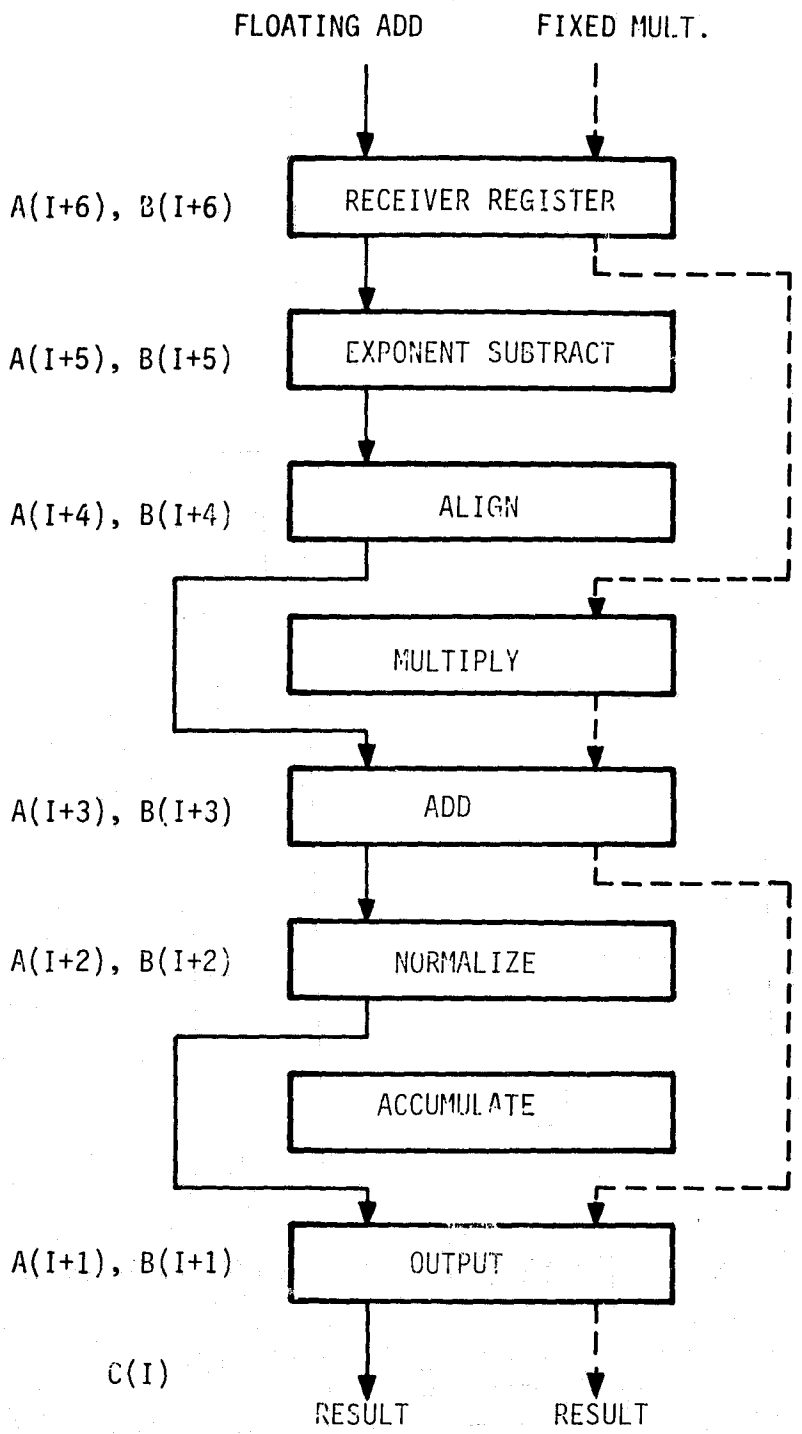

FIGURE 4-1. ARITHMETIC PIPELINE OF TEXAS INSTRUMENTS ADVANCED SCIENTIFIC COMPUTER

displays characteristics similar to other vector processor machines, ie., TI's ASC and CDC STAR.

The approach in the present work was to restructure the discrete vortex wake program into efficient FORTRAN code which then could be replaced by calls to the RDA vector routines. In the listing of the code the serial FORTRAN is left in as comment statements.

Discrete Vortex Wake Vectorization

Since conditional branches can not be handled in the vector method it was first necessary to divide the loops into two segments. One segment would contain all calculations required which were not dependent upon the conditional. In this segment a number of scalars were changed to vectors so that at the cost of a small amount of storage the vector routines could be used.

In some cases the equations that followed the conditional could be expressed in a manner such that a vectorization could be used. Arrays containing either zeroes or ones were generated depending upon the conditional and were used in the calculations. Hence terms would be used or dropped depending upon the value in these arrays. In other cases this method could be used but it was so complicated that the vector code actually took longer to execute than the loop code with the conditional.

At the beginning of the present program a constant radius two dimensional circular cylinder version of the discrete vortex wake program (VTX) was vectorized and timing runs made on the CDC7600. This version of the program used Stratfords criteria for separation. Timing runs on the program indicated that about 75% of the total time was spent in computing the motion of the vortices. The results of the timing runs are presented in Figure 4-2. For a time where there are about 800 vortices in the flow the optimized FORTRAN code resulted in an increase in speed of 35 percent. Vectorizing the optimized code resulted in another 14 percent increase.

The cross flow discrete vortex wake program was then rewritten in structured FORTRAN code and then vectorized. Several algorithms were rewritten and in the region of the missile nose a solution technique

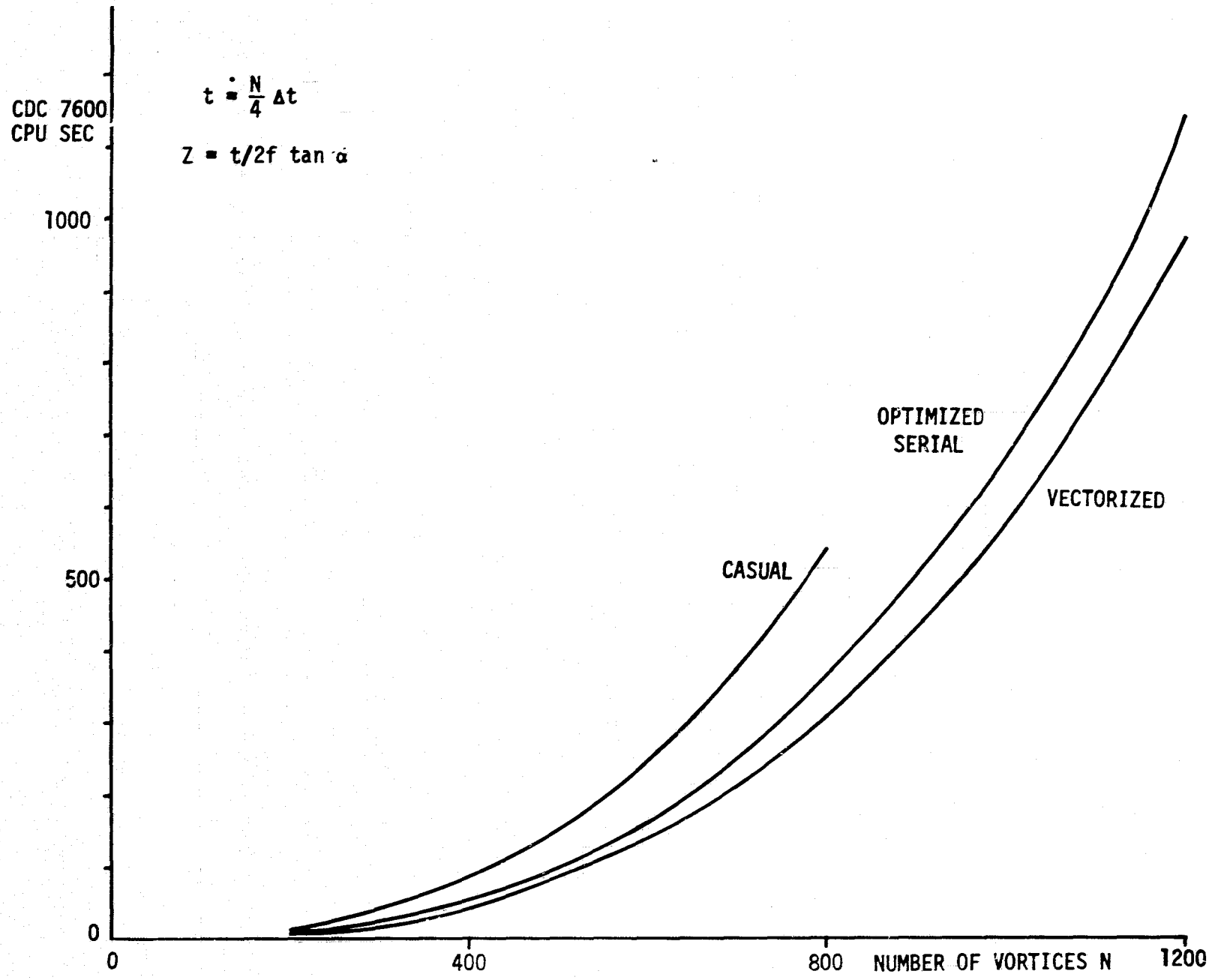

FIGURE 4-2 VTX TIMING RESULTS

based on the integral momentum form of the boundary layer equations was developed to replace the finite difference solution. A summary of the timing results is presented in Table 4-1. These results were obtained with the integral momentum boundary layer solution.

The original cross flow program using the finite difference boundary layer solution was run for the NIBI missile test case at 45 degrees angle of attack. Using the RUNX compiler the program executed in 2694 CPU seconds on TRW's CDC 6600. The unoptimized program using the unsteady integral momentum solution executed in 2122 seconds using RUNX. The vecotorized integral momentum solution on AMES CDC 7600 took 190 seconds to execute using the FTN compiler. Allowing a factor of 5.0 for CDC 6600 to CDC 7600 conversion and a factor of 2.0 to equivalence RUNX and FTN compilers the estimated time for the original finite difference program to run for this case on the CDC 7600 would be 269 seconds. The final vectorized cross flow program is then estimated to be approximately 30 percent faster than the original program. The cross flow program could not achieve the same increase in speed as did the constant radius test case (twice as fast as the original) because much less of the code could be vectorized.

Results obtained using the vectorized DIscrete VORtex Crossflow Evaluator (DIVORCE) program are presented in the next section. The user's manual for DIVORCE is a separate volume of this report.

TABLE 4-1 VISCOUS CROSS FLOW PROGRAM TIMING RESULTS
NIBI (ℓ_n/d=2.598, f=10.325), $\alpha = 30^0$

Cross Flow Program	CDC6600 CPU SEC	CDC7600 CPU SEC
Unoptimized	425	
Structured FORTRAN	317	60
Vectorized		53

5.0 METHOD APPLIED TO BODIES OF REVOLUTION

The vectorized discrete vortex wake cross flow program was applied to several missile test cases of various fineness ratios with varying nose geometry and nose fineness ratios. Table 5-1 lists the test cases for which results are presented. Except for bodies NC (20^{o} cone) and NPP (pointed paraboloid), the nose geometries were sharp tangent ogives. The results for cases NC, and NPP were non-dimensionalized using an average characteristic radius instead of the base diameter. The highest fineness ratio body tested was the ogive nose fineness ratio 5.0, afterbody fineness ratio 11.0, N3C configuration.

Input Values

In addition to body geometry several input values are required by the current method. These values are numerical parameters such as the integration timestep, Δt, and empirical constants like the vortex strength factor σ.

The numerical parameters are:

Δt = integration timestep

ε = coalescence radius

KRCOAL = timestep, t_k, at which to coalesce rear vortices

KCOAL = timestep, t_k, at which to coalesce all vortices

ZI = axial station at which solution is started ZI $\neq$ 0.0

ZPERT = axial station at which a perturbation to newly born vortex strengths is added

ZPEND = axial station at which a perturbation to newly born vortex strengths is removed

The empirical constants are

σ = vortex strength factor

$\Delta\sigma$ = vortex strength perturbation $\sigma' = \sigma\ (1.0 + \Delta\sigma)$

c = constant in Thwaites method = 5.1 (see section 3.3)

β = Stratfords turbulent separation criteria constant = .73

Sk = Stratfords laminar separation criteria constant = .022

X_{tr} = transition location on circular cylinder in radius measured from forward stagnation point = .5236

Body	Angle of Attack α, DEG	Nose Fineness Ratio ℓ_n/d	Fineness Ratio $f=\ell/d$	Afterbody Body Diameter d(inches)	Reference
N1B1	10-50	2.598	10.325	7.6	26
N4B2	10-50	1.633	8.094	7.6	26
N4B7	45	1.633	7.0	2.6	
N2C7	45	3.5	7.0	2.6	
N3C7	45	5.0	7.0	2.6	
NC (20° Cone)	10-50	2.84	2.84	7.4	27
NPP (Pointed Paraboloid)	10-50	2.84	2.84	6.0	27
N3C	10-50	5.0	16.0	2.6	28
N3C1	35-50	5.0	12.0	2.6	28
N2C1	35-50	3.5	10.5	2.6	28

TABLE 5-1 MISSILE TEST CASES

The choice of these parameters and their effect on the solution is discussed in the following.

5.1 N1B1 RESULTS

The predicted normal force coefficient on N1B1 versus angle of attack is presented in Figure 5-1 and is compared with MX results, Reference (26). Past experience with the discrete vortex wake program has shown that good normal force results can be obtained with the vortex strength parameter, $\sigma = 0.6$. However these results, Reference (9), were for angles of attack less than 30 degrees. For larger angles of attack only a very limited number of cases have been run. Figure 5-1 shows that good results are obtained up to 30 degrees for $\sigma = .6$, but at higher angles of attack normal force is underpredicted. The bar on the last symbol denotes a range of values which may be obtained if during the solution the vortices are coalesced. This effect will be discussed in detail later.

At 45 degrees angle of attack normal force coefficient was predicted using values of $\sigma = 1.0$ and $\sigma = \sin \alpha = .707$. The predicted values are higher since increasing vortex strength produces a stronger wake which increases pressure drag on the two dimensional circular cylinder. Figure 5-2 shows that predicted pitching moment coefficients agree well with experiment to 40 degrees angle of attack with, $\sigma = .6$, but drops off at higher angles. The distribution of normal force coefficient per unit length is presented in Figure 5-3. Increasing the vortex strength parameter results in a better prediction over the nose region but then overpredicts the load on the afterbody.

Prior to exercising the discrete vortex wake program to predict side forces and moments on the goemetries listed in Table 5-1 a parametric

study was undertaken to determine the sensitivity of the method to the various numerical and empirical parameters listed in Section (5.0). In general normal forces and moments were not largely affected (except for σ). However side forces and moments were nearly always affected.

The parametric study was undertaken for the N1B1 body since the largest amount of experimental data was available for that body.

Effect of Vortex Strength Parameter σ

The effect of σ on side force distribution is not well understood as it is for normal force. While eventually (in the steady state) stronger vortices would probably result in larger amplitudes of oscillating lift it is not clear how stronger vortices affect the initial vortex development. The side force coefficient on N1B1 is presented in Fig. 5-4. The magnitude of the predicted coefficients bounds the values obtained experimentally. However, at the same angle of attack the side force coefficient may be positive or negative depending on the choice of σ. Figure 5-5 shows the side force coefficient per unit length along the missile axis for three values of σ. The development of the asymmetry is similar up to about half (Z = .5) the body length. In this example σ = .707, produced the largest side force. The corresponding yawing moment coefficient is presented in Figure 5-6.

Effect of Coalescence on Side Force Distribution

To save computer time it may be desirable to coalesce two vortices into one if they are in close proximity. Virtually all of the discrete vortex methods have some type of coalescence scheme. Normal force is affected little by coalescence. Side force on the other hand is significantly affected as is shown in Figure 5-7. Vortex plots at Z = .804 are presented in Figure 5-8 for the case of no coalescence and coalescence using the largest core radius of ε = .25. From Figure 5-8 very little difference in the wake structure can be observed (aside from fewer vortices). In examining the pressure distributions at Z = .7516, Figure 5-9, however, it appears that small differences in the pressure occur and result in

the significant differences in side force when integrated.

The initial vortex growth is very sensitive to small perturbations. Coalescing the vortices introduces an error of only order ε^2 at the time of the coalescence. However this small perturbation significantly affects the initial vortex growth and eventual asymmetry. At later times a Karman vortex street will always be established and the initial perturbation is not important. However for times pertinent to the cross flow analogy coalescence makes a difference as indicated in Figure 5-7 for $\alpha = 30^0$ and Figure 5-10 for $\alpha = 45^0$.

For the same reasons described above the frequency of coalescence, or the time at which the first vortices are coalesced can alter the distribution of side force, see Figure 5-11.

Effect of Δt on Side Force Distribution

In the present work Δt is usually allowed to vary from $\Delta t = .05$ near the nose tip where the cylinder radius is small and a small timestep is required to a constant value usually $\Delta t = .125$ at the nose afterbody junction. Figure 5-12 shows the effect of constant $\Delta t = .125, .250$. Letting Δt be variable had little effect. However, $\Delta t = .250$ significantly reduced the amplitude of the sectional side force coefficient. For 30 degrees angle of attack $\Delta t = .0625$ was also tried with results significantly different from the $\Delta t = .125$, and $\Delta t = .250$ cases. However the maximum amplitude of the sectional side force coefficient for 30 degrees was only 0.1.

In addition to being the integration timestep, Δt also implicitly determines the distance m (see Eqn 3-21) at which vortices from the boundary layer and rear shear layer are introduced into the outer flow. Further work needs to be done in examining the effect of Δt. The discrete vortex wake solution may not be unique as indicated by many of the present results. For many of the cases run in this and other studies $\Delta t = .125$ has provided reasonable answers. For the rest of the results presented in this work $\Delta t = .125$.

5.2 OTHER TEST CASES

Based on the study of the N1B1 body, discrete vortex wake parameters were chosen as follows to investigate the effect of angle of attack, nose fineness ratio, nose geometry, and overall fineness ratio:

σ = .6 (unless otherwise specified)

$\Delta\sigma$ = .1

ZI = .01

ΔT = .125 (variable .05 to .125 on the nose)

ZPERT = .05, ZPEND = .25 } (unless otherwise specified)

KRCOAL = 30, KCOAL = 150 } if vortices coalesced, ie., normally α = 10, 20, 30 does not require coalescence

N4B2

The forces and moments on N4B2 (ℓ_n/d = 1.633) are presented in Figs. 5-13 through 5-17. The normal force coefficient agrees well with the experimental data up to 45 degrees angle of attack. The pitching moment coefficient is somewhat higher than the experimental values for angles of attack greater than about α = 30 degrees. Examination of the normal force distribution shows that the predicted normal force is higher over the nose region than that measured experimentally. This is in contrast to the N1B1 results which underpredicted nose distribution of local normal force coefficient. Predicted and experimental side forces are small except at 45 degrees angle of attack. The predicted results show a change in side force sign only at α = 40 degrees. Similarly the predicted yawing moment changes sign whereas the force data does not.

The predicted force and moment results are of the same order of magnitude as the experimental values. A plot of |CY| versus angle of attack would show better agreement. However, the purpose of the present work is to examine and disclose the applicability of discrete vortex methods for the cross flow problem and therefore signed values are presented.

N2C1, N3C1

The present method was applied to the data taken by Jorgensen Ref. (28) on ogive cylinders of nose fineness ratio $\ell_n/d = 3.5$, and $\ell_n/d = 5.0$, and afterbody ratio 7.0. A calculation was also done with afterbody fineness ratio 11.0. The purpose was to determine if effects of nose fineness can be predicted using the discrete vortex method. The normal force coefficient data in Figure 5-17 shows that the predictions are significantly lower than the experiment. Part of the discrepency is a Mach number effect. Figure 5-18 shows the predicted normal force coefficient with $\sigma = 1.0$ to be in much better agreement. Predicted aerodynamic normal force center also agrees well with Jorgensens results, Figure 5-19. Jorgensen found maximum side force to occur at 35 to 40 degrees on N3C1, Figure 5-20. Maximum predicted side force coefficient occurs at 50 degrees angle of attack and is only about one half of the maximum value obtained by Jorgensen. Yawing moment is presented in Figure 5-21. Side force coefficient results for N2C1 and for N3C (f = 16.0) are presented in Figure 5-22 in addition to the N3C1 results. The N3C1 configuration ($\ell_n/d=5.0$, f=12.0) resulted in the largest predicted side force.

Effect of Nose Fineness Ratio on Side Force Coefficient Distribution

To examine in more detail the effect of nose fineness ratio on asymmetric vortex develpment and side force distribution three bodies of overall fineness ratio f = 7.0, and nose fineness ratios, $\ell_n/d=1.666$, 3.5, and 5.0 were run at 45 degrees angle of attack. Discrete vortex wake parameters were ZI = .01, ZPERT = .05, ZPEND = .25, $\sigma = .6$, $\Delta\sigma = .1$, $\Delta t = .125$, and were the same for the three runs. The vortices were not coalesced. The sectional side force coefficients Figs. 5-23, all are initially perturbed to positive values and then reach a maximum negative amplitude at about, Z = .4. The longest nose attained the largest sectional side force amplitude. The effect of nose fineness ratio on separation angle is presented in Figure 5-24. Separation is in general further windward for the highest fineness ratio body. The

short ogive tends to prolong separation. The jump in the separation curve at Z = .3 for case N4B7 is a result of changing from the unsteady boundary layer solution to Stratford's quasi-steady scheme. The separation angles for all three bodies approach Θ_s = 85 degrees at about 70% of the body length. Figure 5-25 shows the vortex growth for the short, N4B7, and long N3C7 ogives. The N2C7 development was very similar to N3C7. The radii are to the same scale. Some differences are observable in the vortex wake. However, overall the vortex development looks very similar. While nose fineness ratio has an effect on the predicted asymmetric vortex development and on the resulting side force distribution it is not clear that these effects are any greater than the effect of changing one of the other parameters in the method such as, Δt, or coalescence radius or frequency, and probably has much less of an effect than changing σ, or ZPERT and ZPEND. Figure 5-26 shows the effect of applying the vortex strength perturbation over different lengths of a fineness ratio ℓ_n/d = 5.0 ogive nose. The length scale in Figure 5-26 is non-dimensionalized by the longest body length, ℓ_{Ref} = 16.378 inches.

The effect of forebody geometry was briefly examined for the case of a sharp 20^o cone and a pointed paraboloid (ℓ_n/d = 3.5, f = 3.5). The side force coefficient is presented for comparison with the available data. Forebody geometry had little effect on the predicted side force coefficient.

Pressure Distribution

One of the purposes of a complex method such as the discrete vortex wake program is to be able to predict surface pressures and the distributed aerodynamic load. The sectional normal force coefficient and sectional side force distributions on N1B1 at 45 degrees angle of attack is presented in Fig. 5-28, and 5-29.

The corresponding vortex development and surface pressures are presented in Figures 5-30 and 5-31. The numerical perturbation caused an asymmetric vortex development which resulted in a side force distribution opposite in sign to that obtained experimentally. Applying the perturbation to the opposite point would change the sign of

the predicted results. Rather than rerun the case the results can be viewed as in Figure 5-30. The usual nomenclature is y positive to the right. Figure 5-30 shows the vortex development on N1B1 at 45 degrees angle of attack. Corresponding pressures are presented in Figure 5-31. At Z = .124 the experimental and predicted pressures are almost symmetric.

At Z = .222 the experimental pressures are still symmetric whereas slightly asymmetric pressures are predicted at Z = .232. Pressure recovery on the rear of the cylinder is considerably lower for the experiment. At Z = .337 the experimental pressure begin to show an asymmetry. The theoretical pressures at Z = .352 are asymmetric but with lower pressures at 80 degrees as opposed to the experiment which exhibits the lowest pressure on the opposite side at 285 degrees.

At Z = .352 the vortex plot Figure 5-30 shows the left vortex beginning to dominate. Hence, the lower pressures on the left half of the body ($0 < \theta < 180$ degrees). At Z = .594, Figure 5-30, the left vortex has entrained fluid from the right side and has weakened. This allows the right vortex to increase in strength as the weakening left vortex begins to move downstream. The corresponding pressure Figure 5-31 (Z=.594) shows a large asymmetry with the lowest pressure on the right side where the stronger right vortex exists. The agreement with the experimental pressures, Z = .591, is very good. At the last station the left vortex is again dominant as shown in Figure 5-30, Z = .835. The predicted pressures at this station show the presence of a strong left vortex. The experimental pressure data, Figure 5-31 Z = .845 reflects a similar asymmetry.

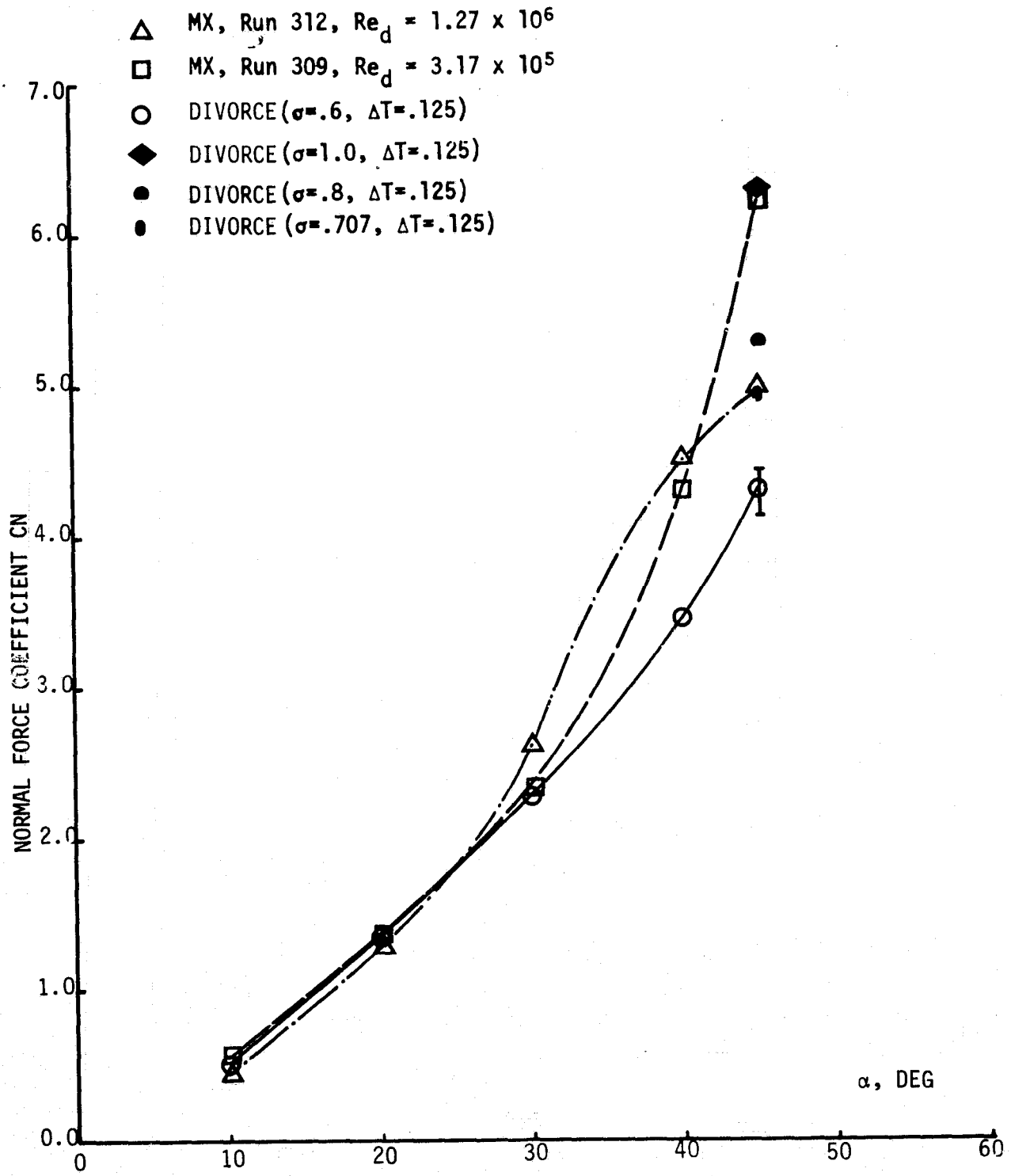

FIGURE 5-1. NORMAL FORCE COEFFICIENT ON N1B1 (ℓ_n/d = 2.598, f = 10.352) vs. Angle of Attack

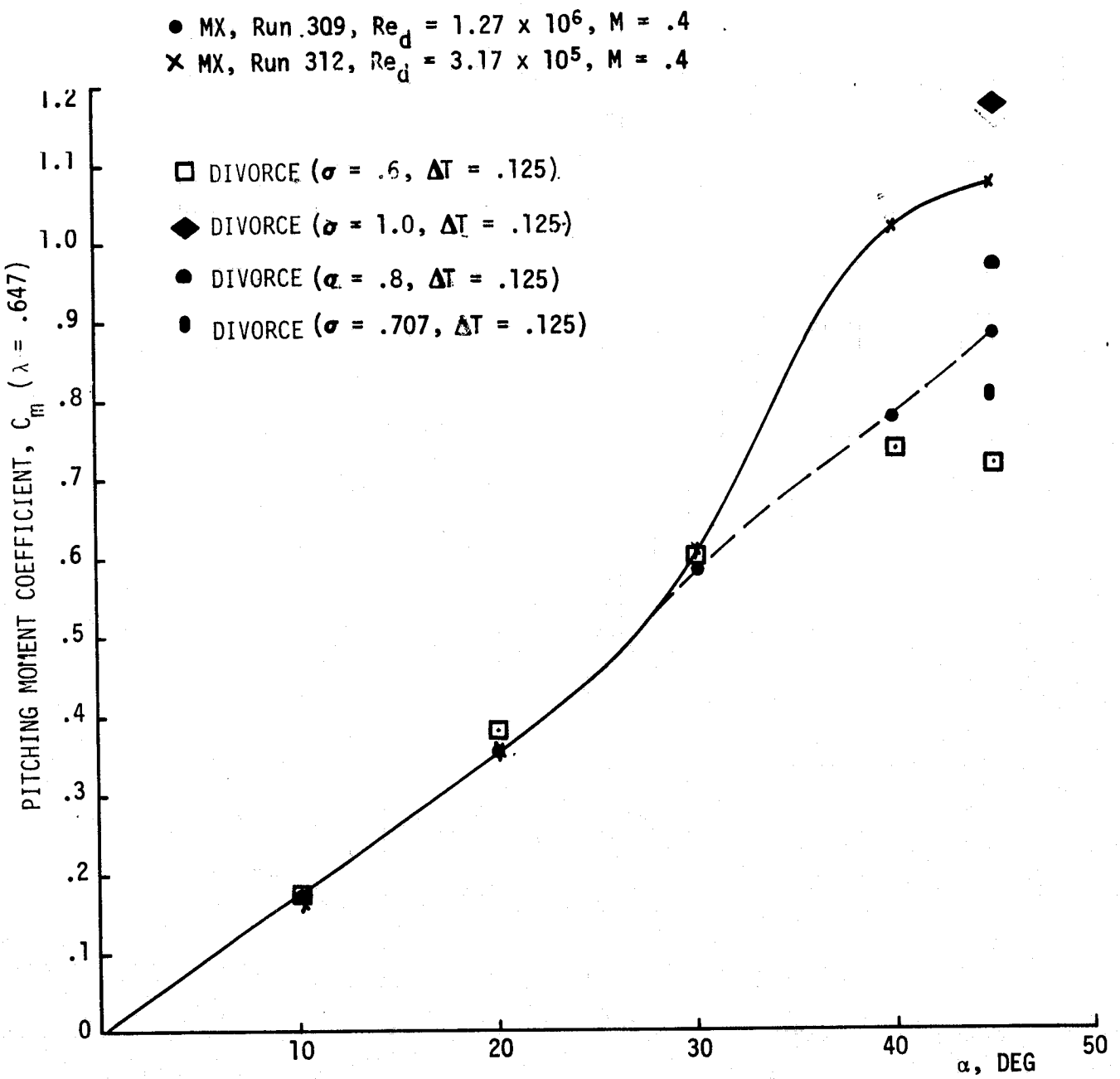

FIGURE 5-2 N1B1 PITCHING MOMENT COEFFICIENT WITH ANGLE OF ATTACK

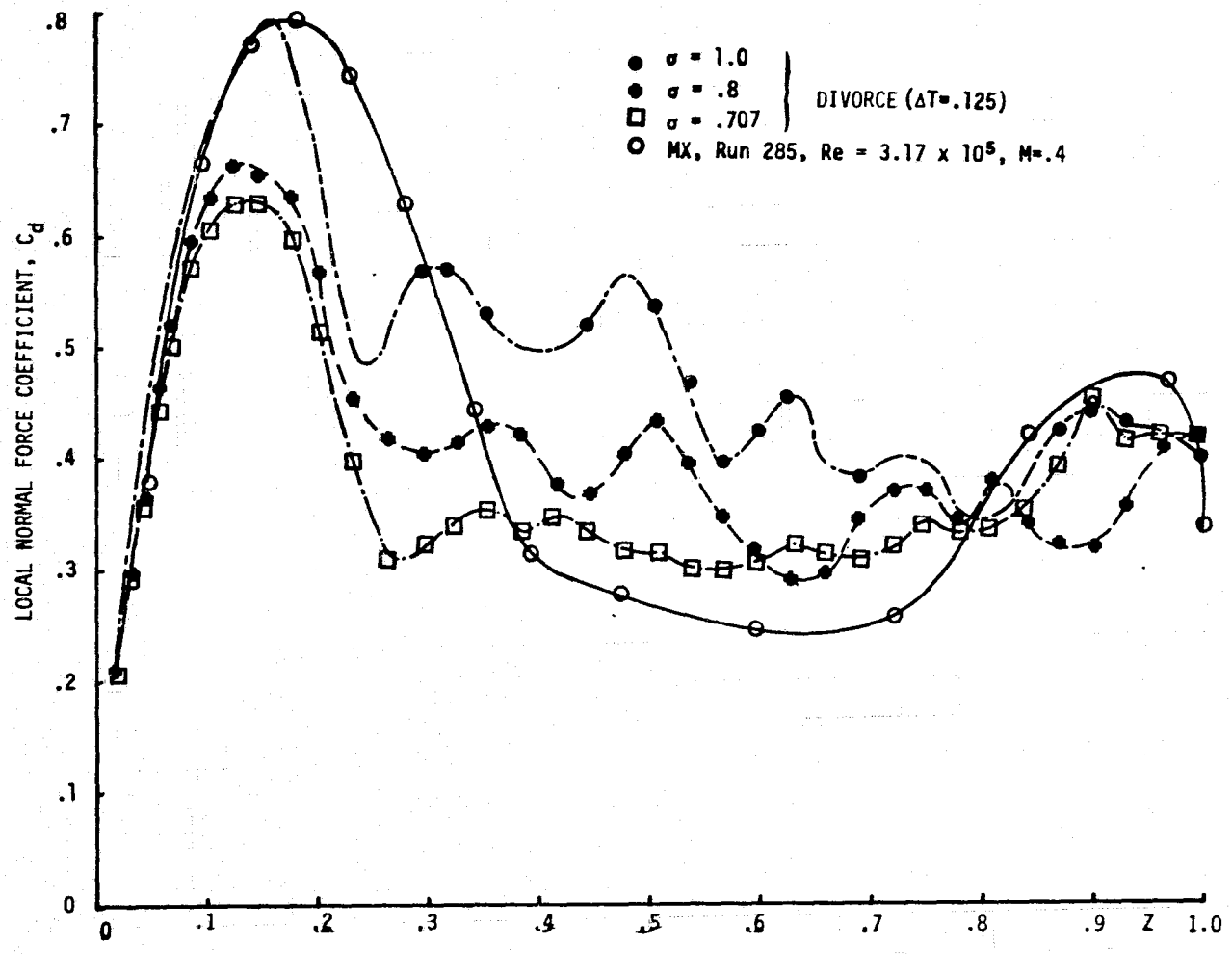

FIGURE 5-3 EFFECT OF VORTEX STRENGTH PARAMETER σ, ON N1B1, α = 45° NORMAL FORCE DISTRIBUTION

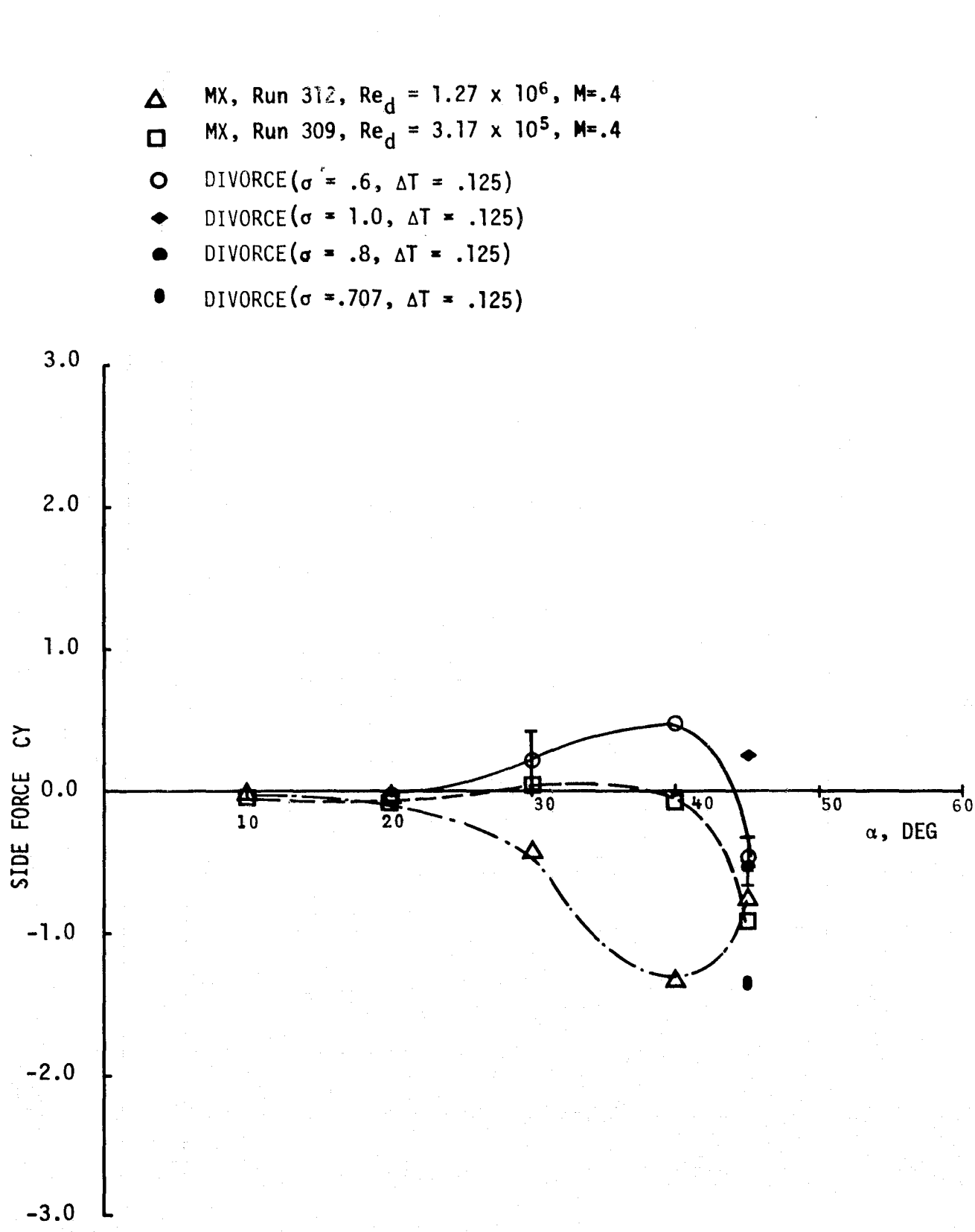

Figure 5-4 SIDE FORCE COEFFICIENT VARIATION WITH ANGLE OF ATTACK (N1B1, ℓ_n/d=2.598, f=10.325)

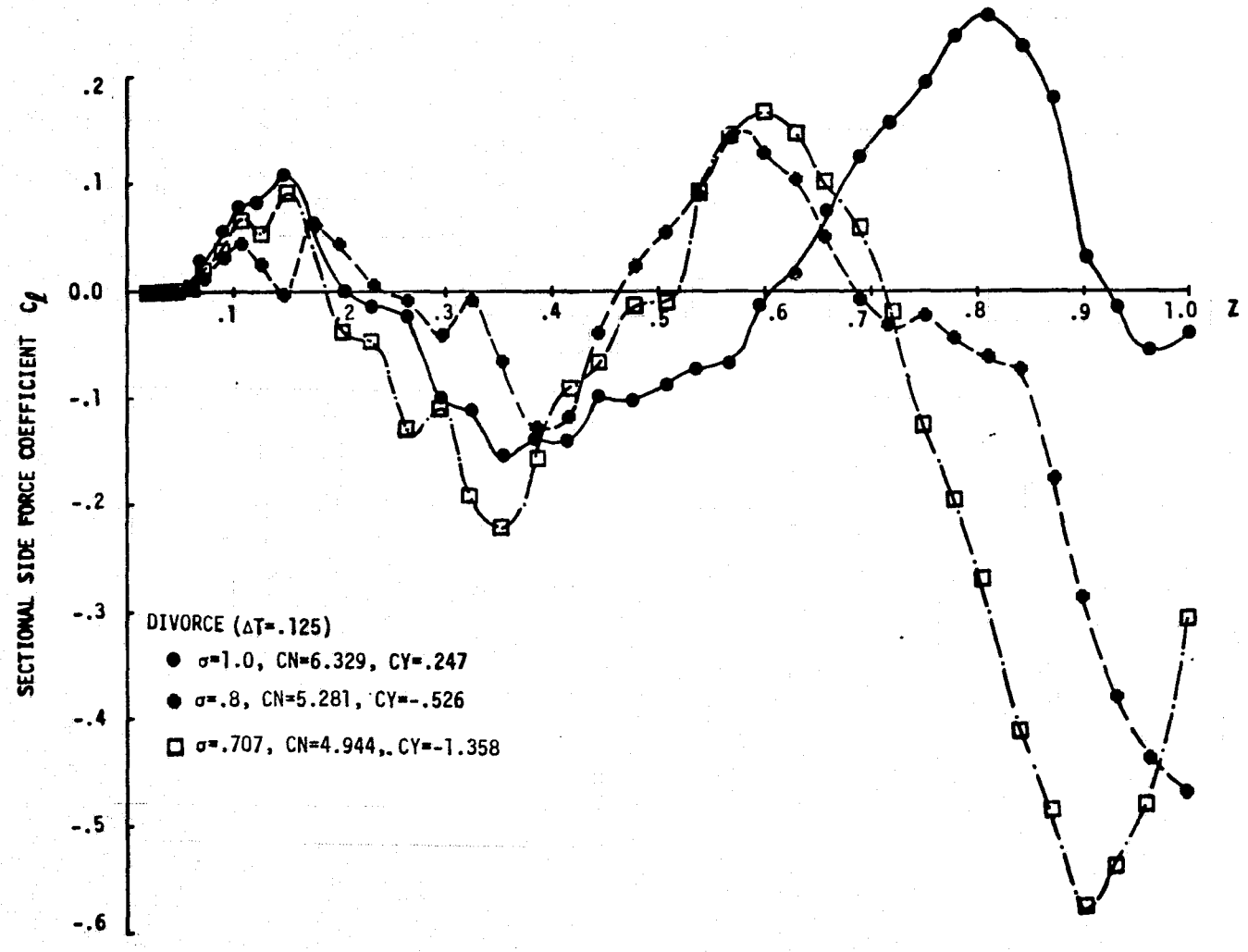

FIGURE 5-5 EFFECT OF VORTEX STRENGTH PARAMETER, σ, ON N1B1 SIDE FORCE DISTRIBUTION, α = 45°

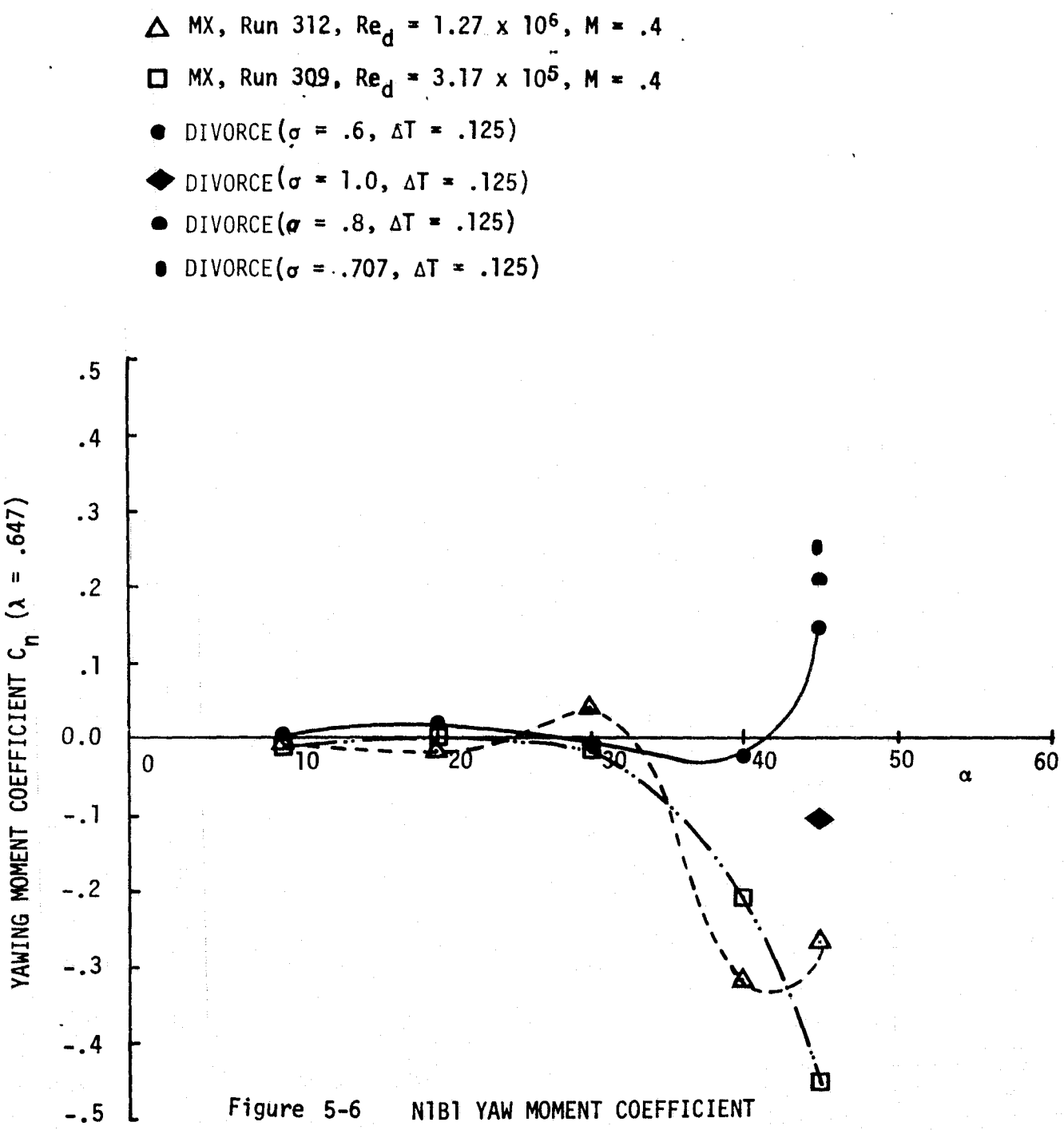

Figure 5-6 N1B1 YAW MOMENT COEFFICIENT WITH ANGLE OF ATTACK

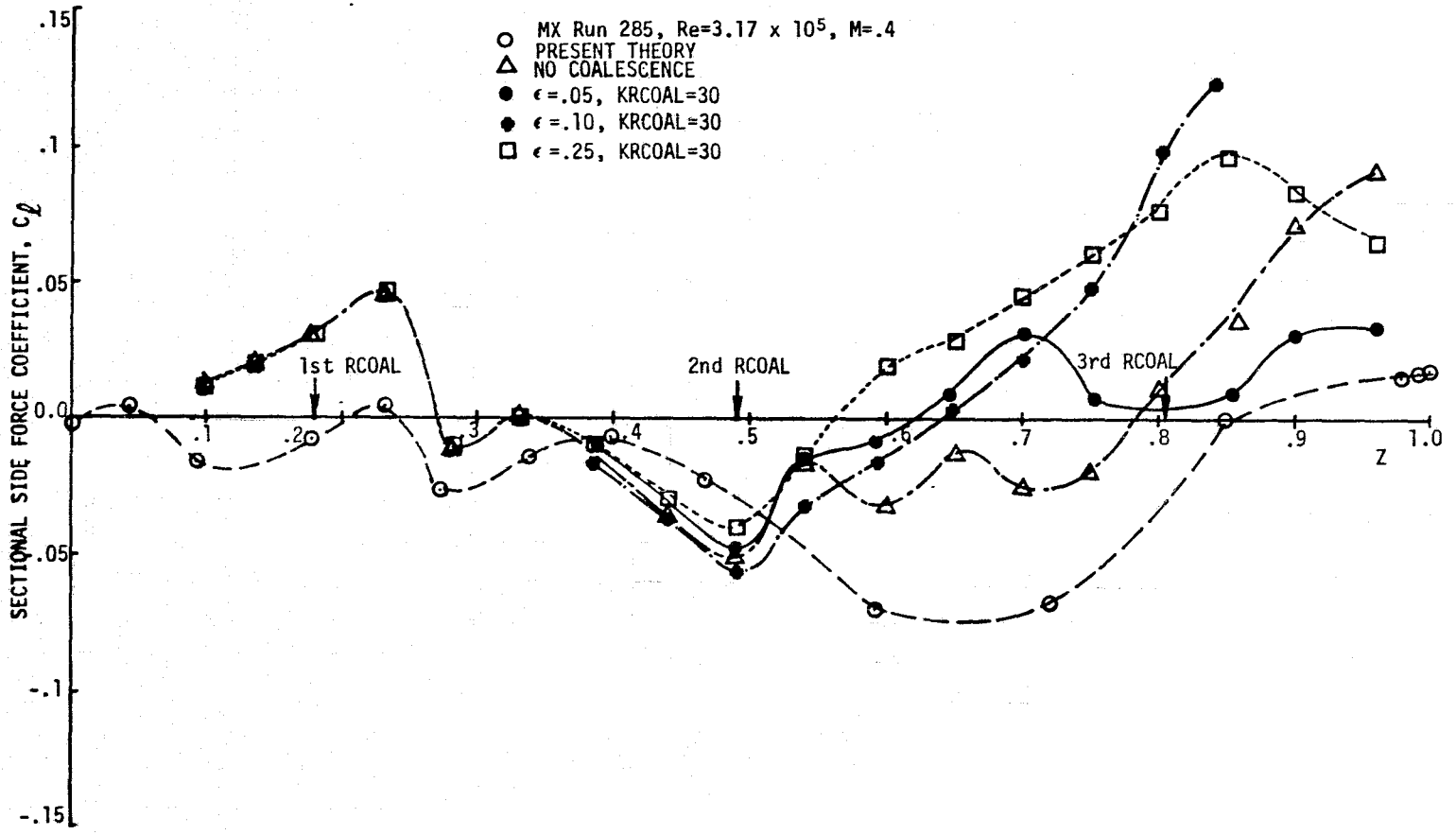

FIGURE 5-7 EFFECT OF COALESCENCE RADIUS ON N1B1 SIDE FORCE DISTRIBUTION, α=30°

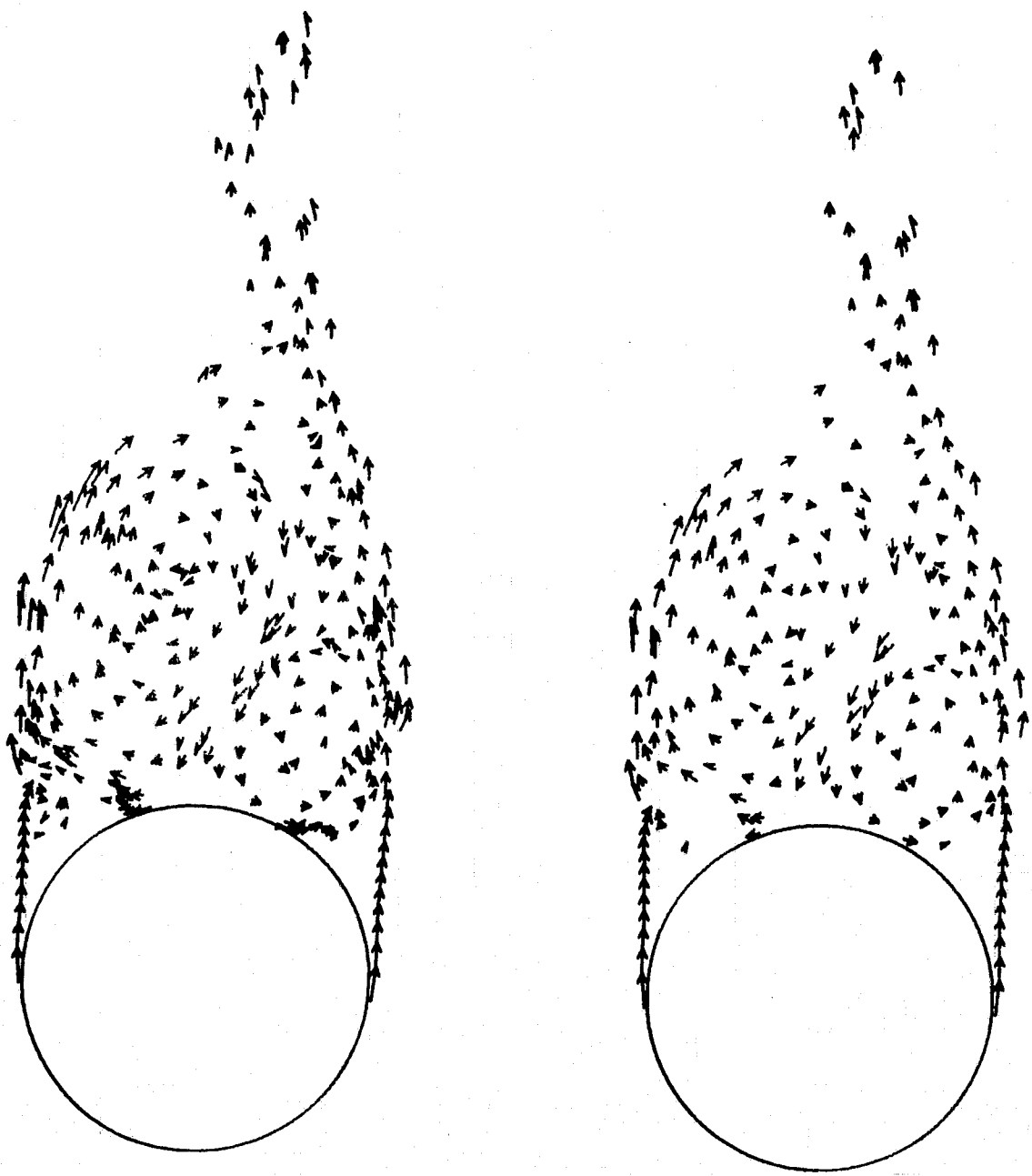

FIGURE 5-8 EFFECT OF COALESCENCE ON DISCRETE VORTEX WAKE DEVELOPMENT, Z=.804

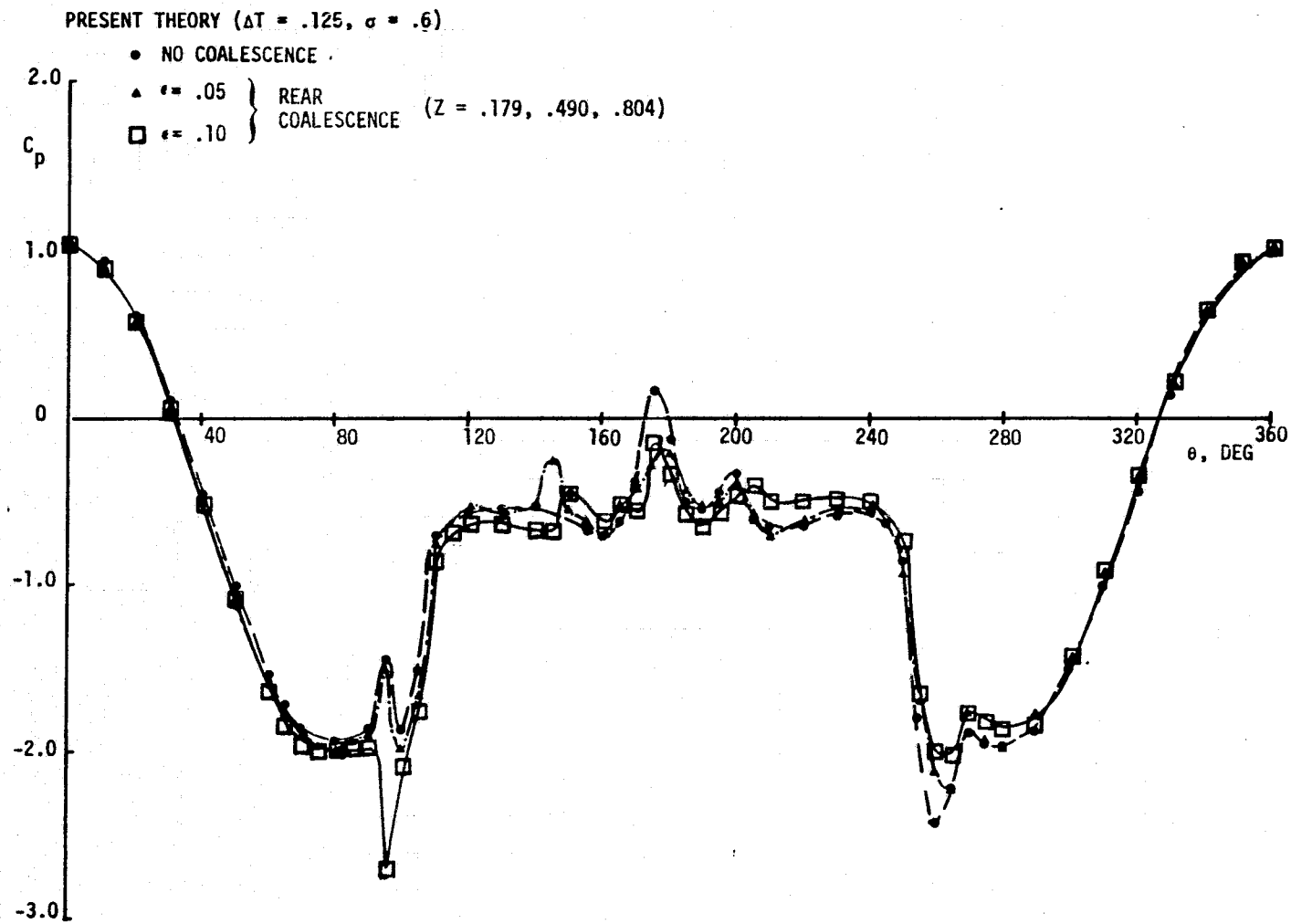

FIGURE 5-9 EFFECT OF COALESCENCE RADIUS, ε, ON N1B1 PRESSURE DISTRIBUTION, α=30°, Z =.7516

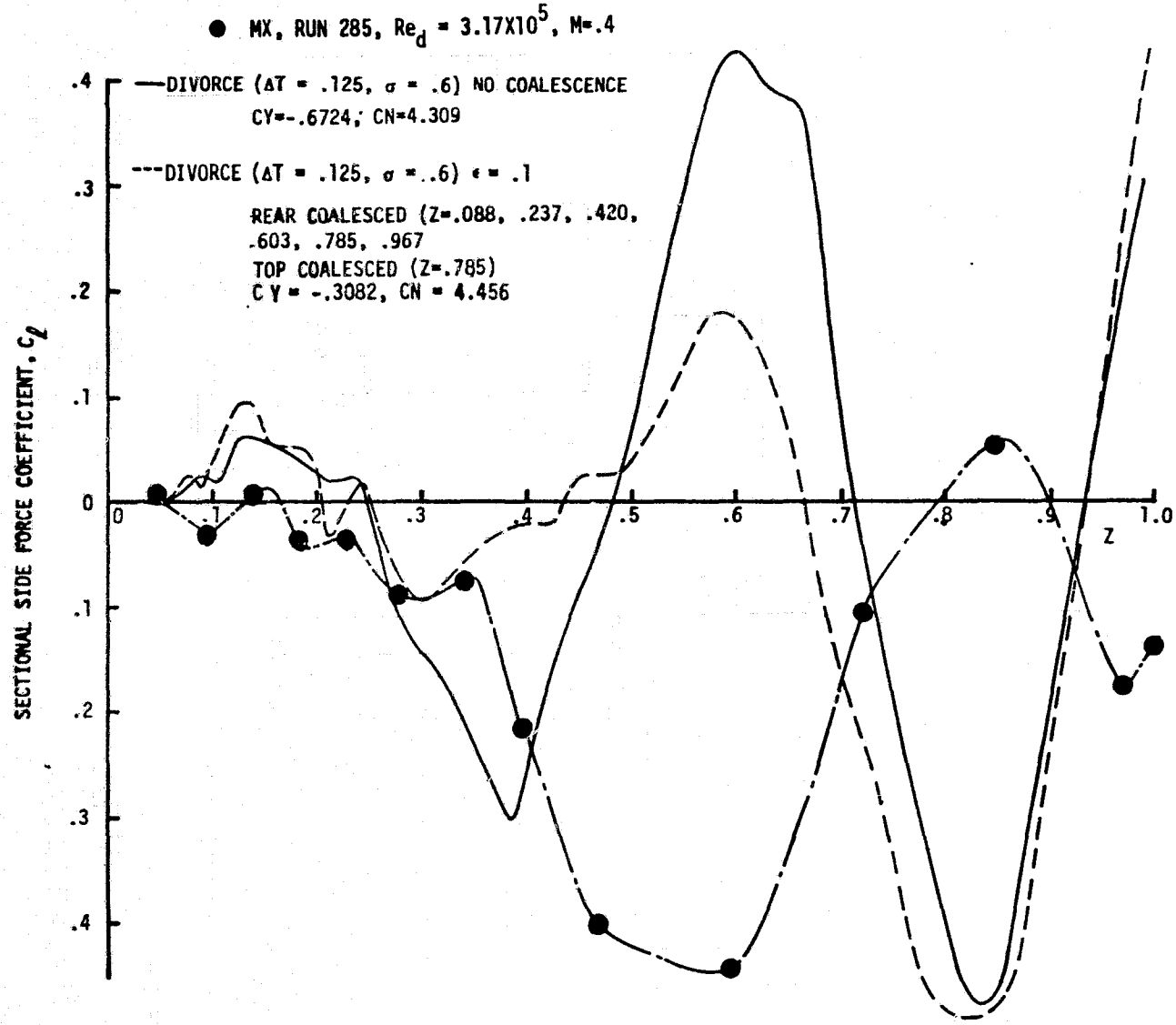

FIGURE 5-10 EFFECT OF COALESCENCE ON N1B1 SIDE FORCE DISTRIBUTION, α=45°

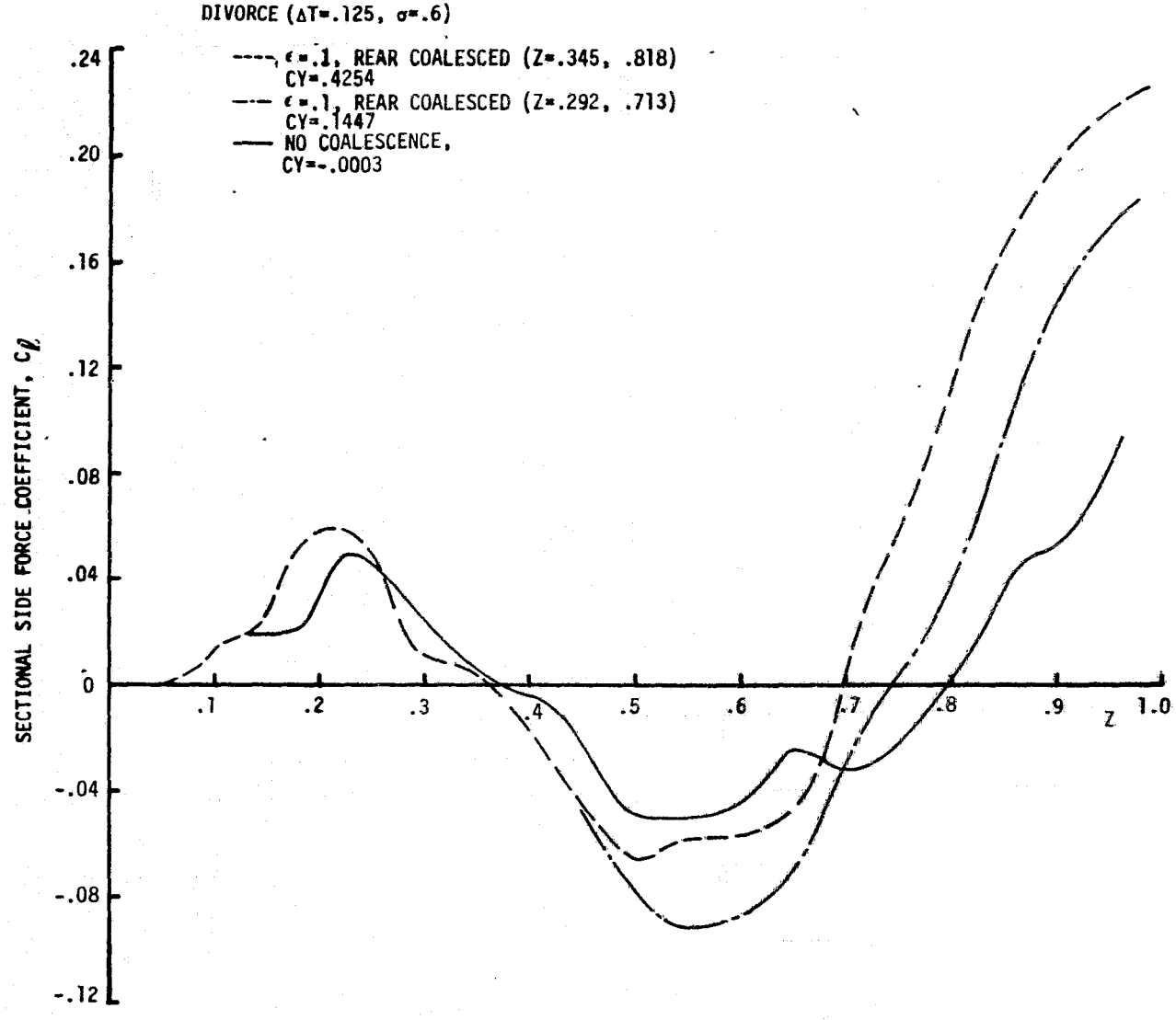

FIGURE 5-11 EFFECT OF COALESCENCE FREQUENCY ON N1B1 SIDE FORCE DISTRIBUTION, α=30°

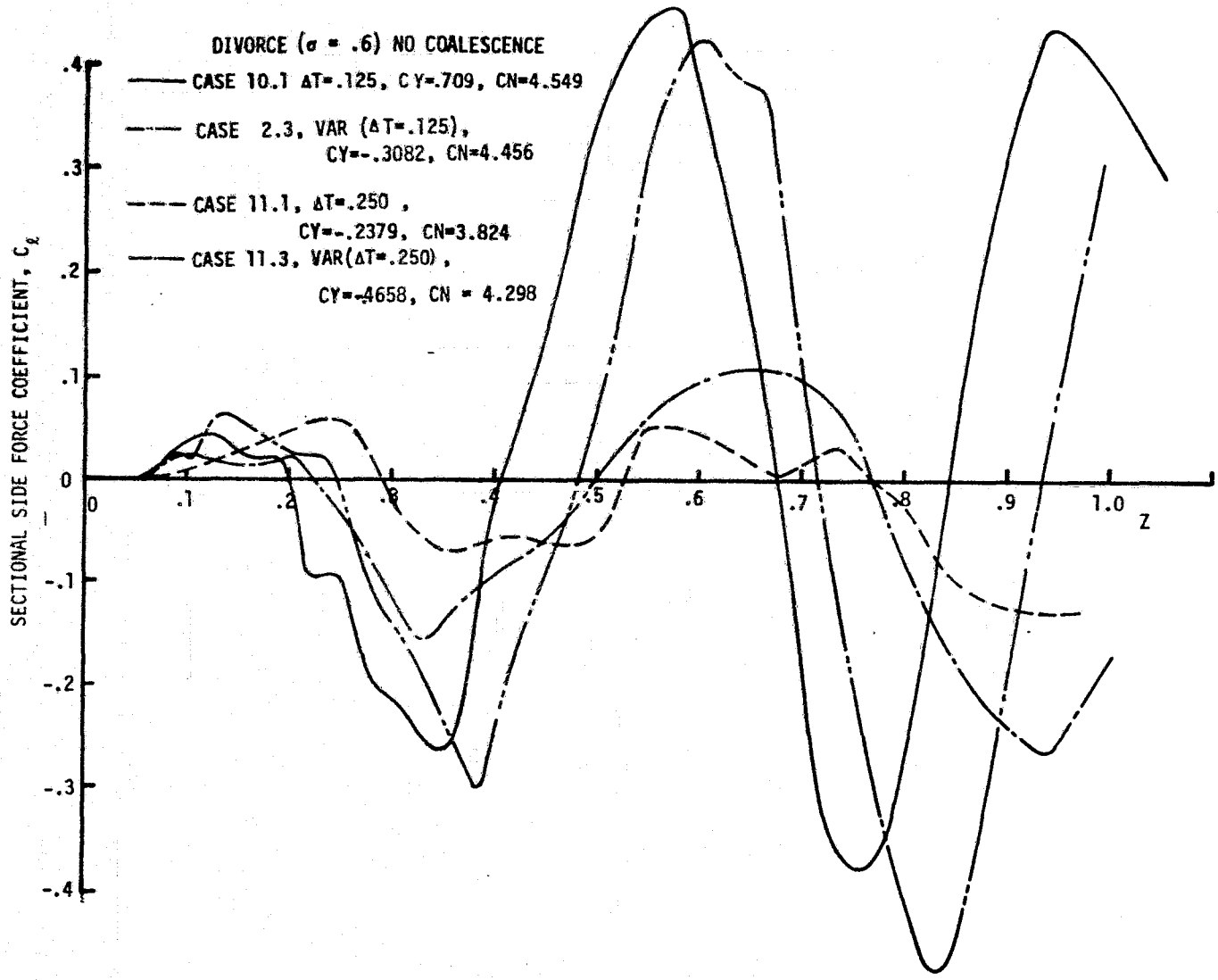

FIGURE 5-12 EFFECT OF ΔT ON N1B1 SIDE FORCE DISTRIBUTION, α=45°

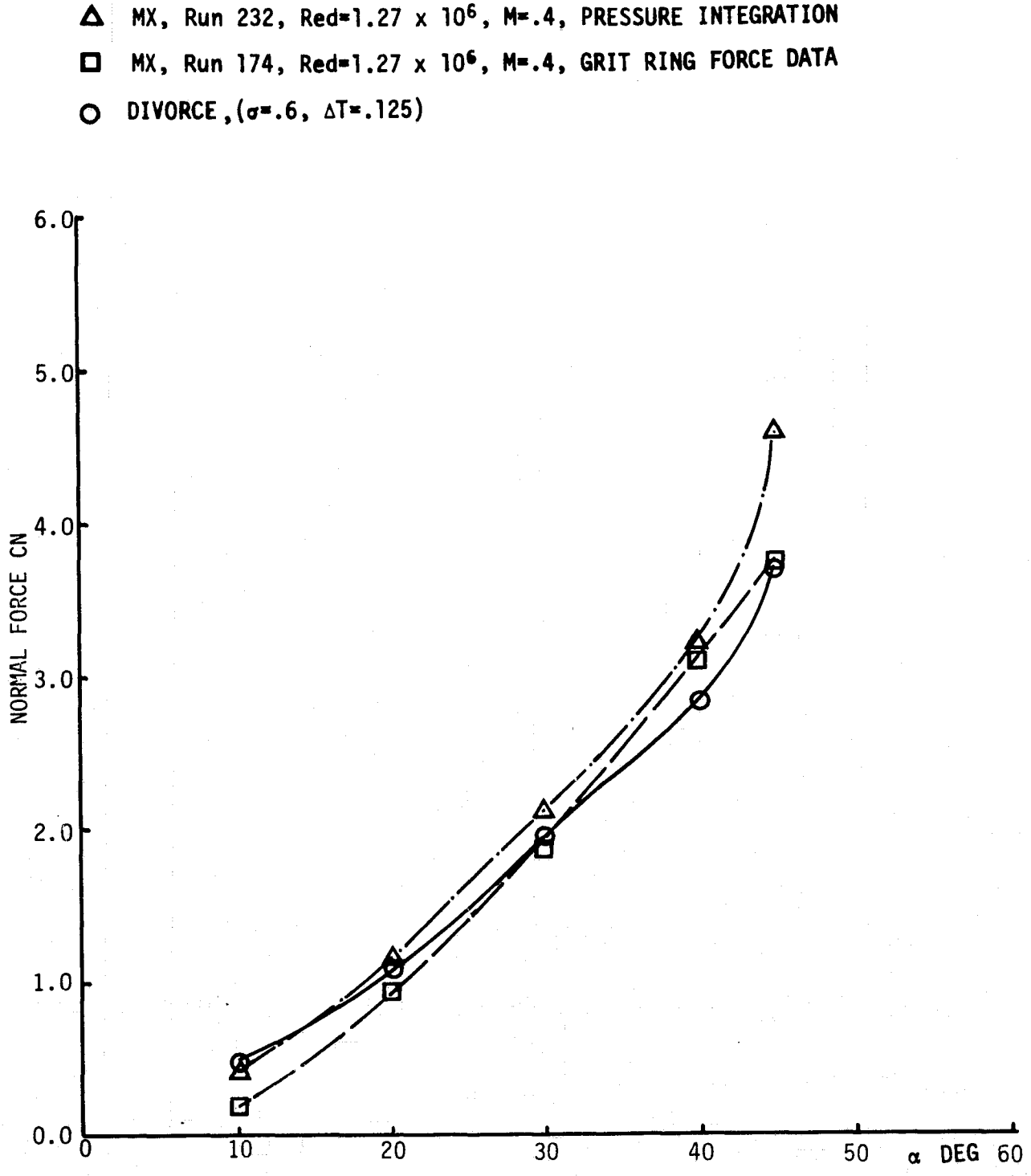

FIGURE 5-13 NORMAL FORCE COEFFICIENT VARIATION WITH ANGLE OF ATTACK N4B2 (ℓ_n/d = 1.666, f = 8.094)

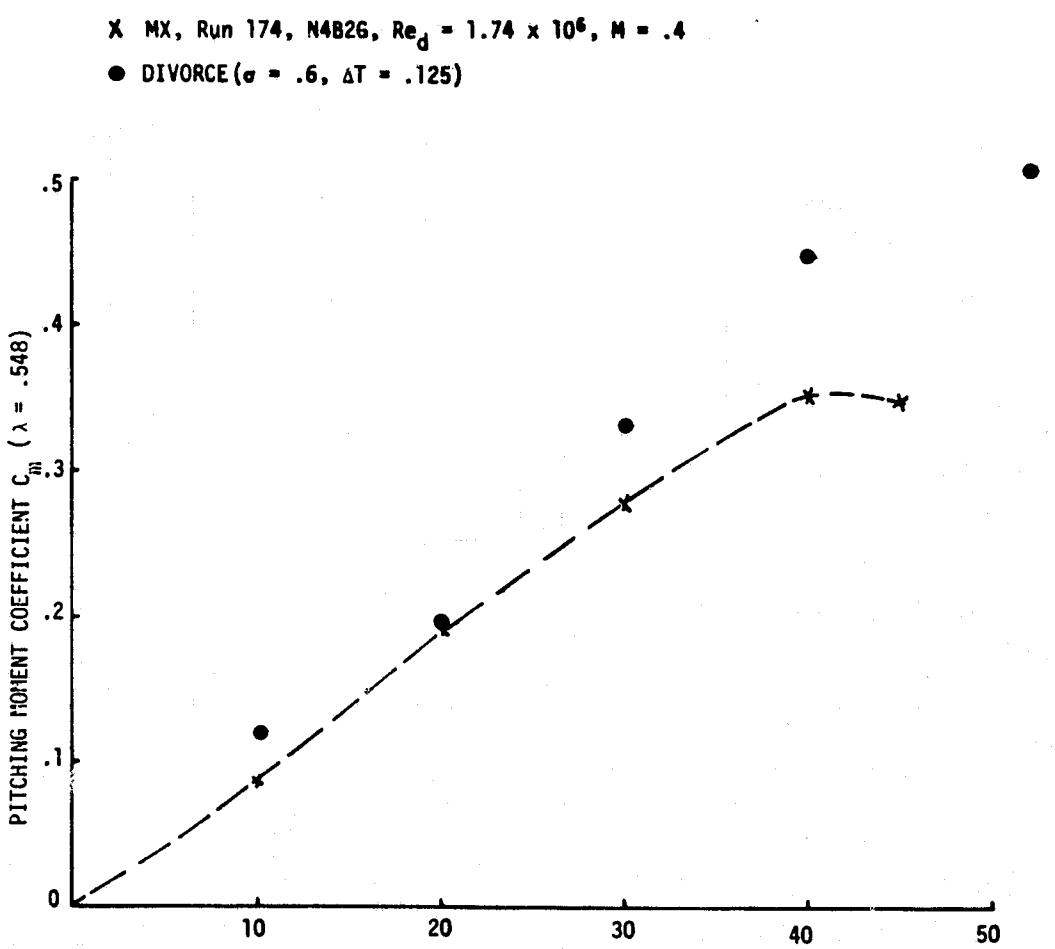

FIGURE 5-14 N4B2 PITCHING MOMENT COEFFICIENT VARIATION WITH ANGLE OF ATTACK

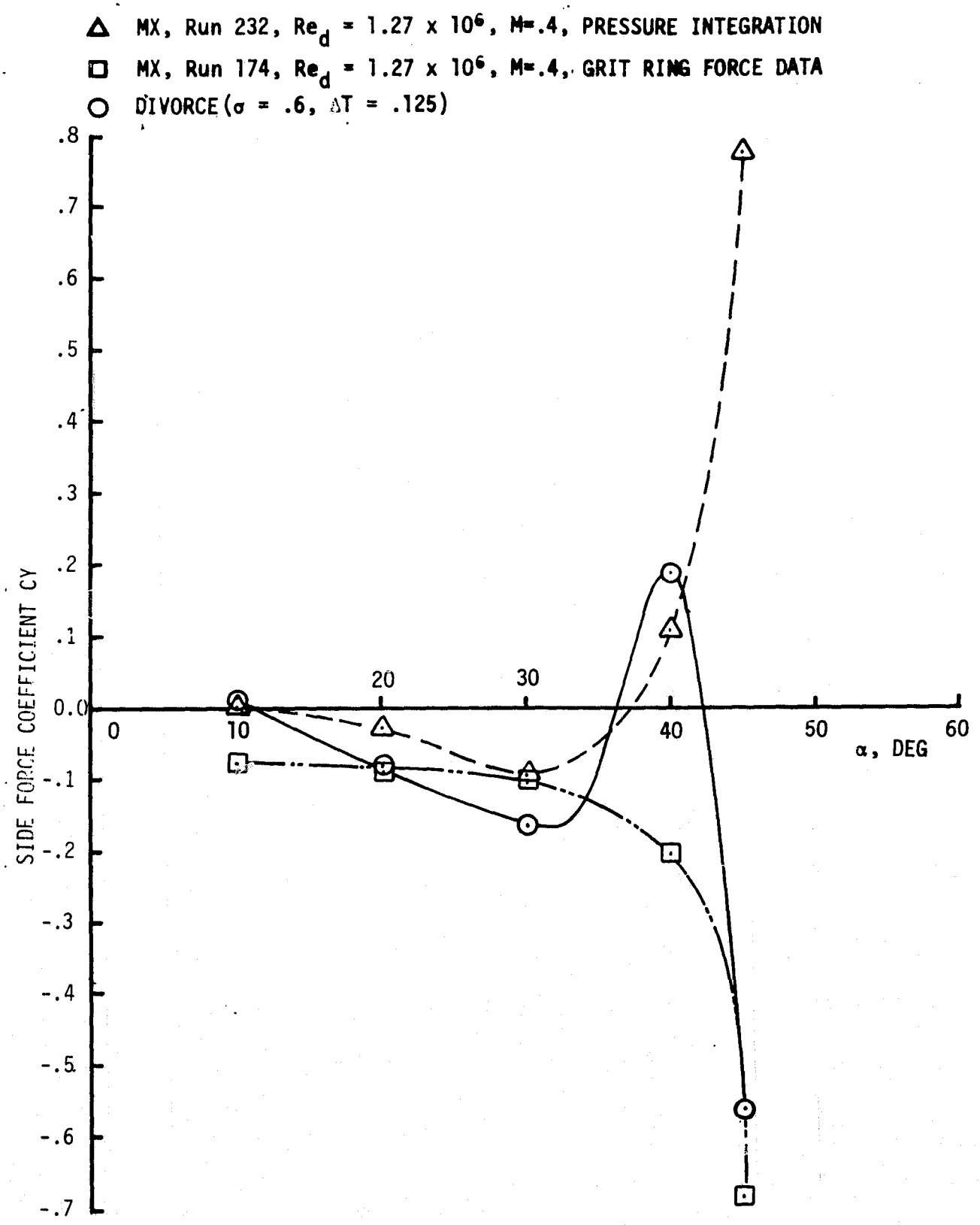

Figure 5-15 SIDE FORCE COEFFICIENT VARIATION WITH ANGLE OF ATTACK (N4B2, ℓ_n/d=1.666, f=8.094)

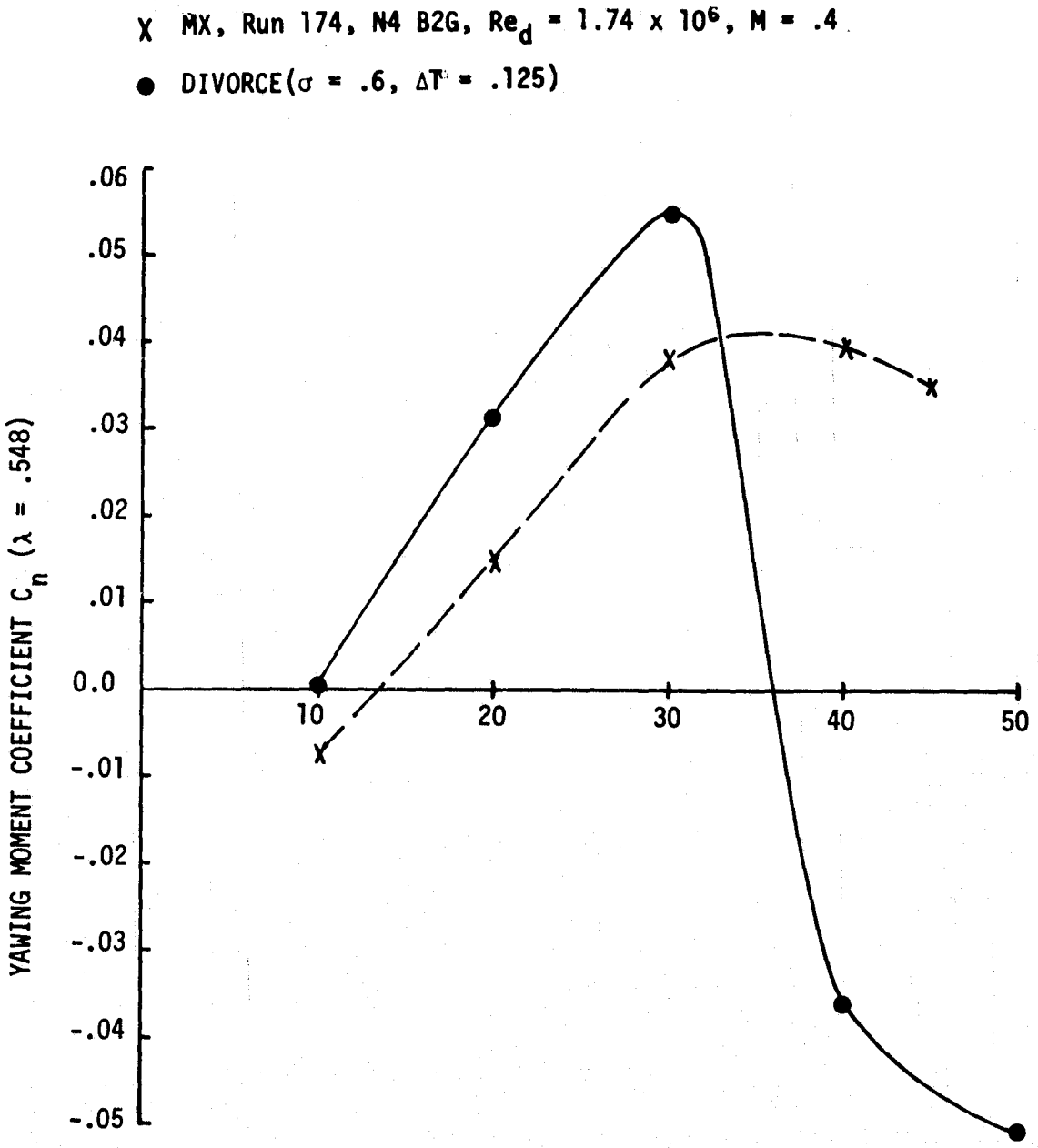

FIGURE 5-16 N4B2 YAWING MOMENT COEFFICIENT VARIATION WITH ANGLE OF ATTACK

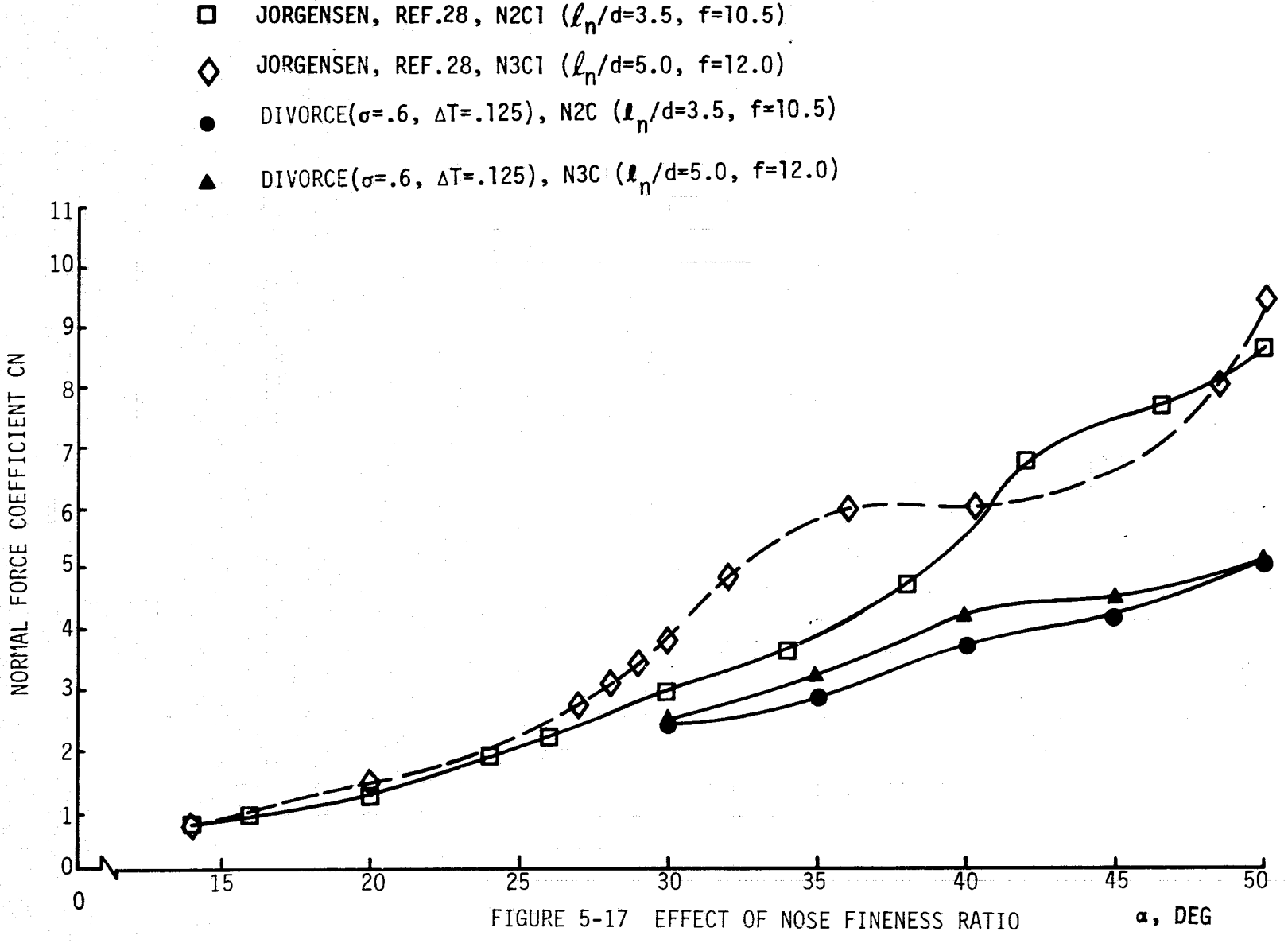

FIGURE 5-17 EFFECT OF NOSE FINENESS RATIO

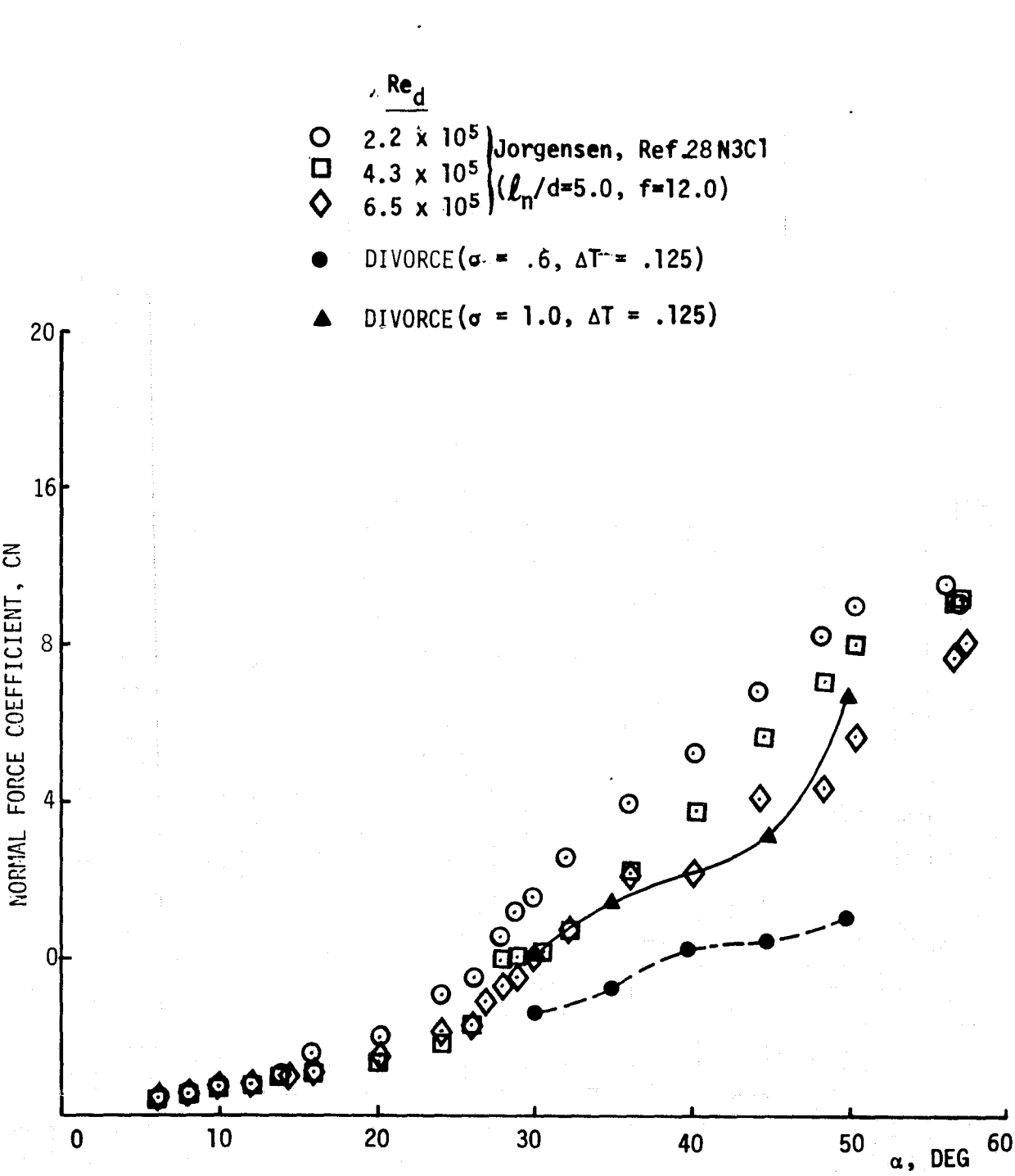

FIGURE 5-18 EFFECT OF VORTEX STRENGTH PARAMETER, σ, ON N3C1 NORMAL FORCE

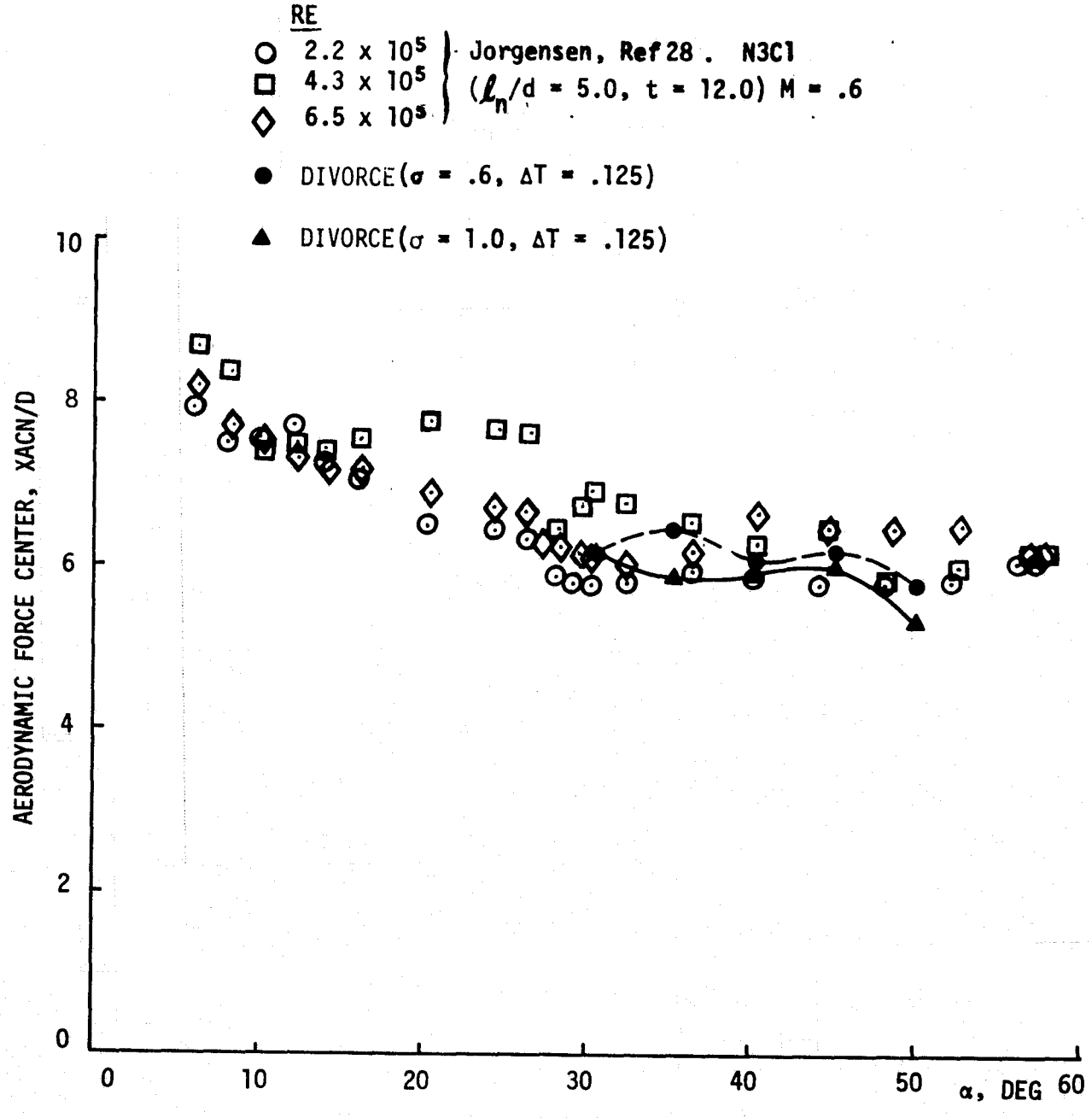

FIGURE 5-19 EFFECT OF VORTEX STRENGTH PARAMETER, σ, ON N3C1 AERODYNAMIC FORCE CENTER.

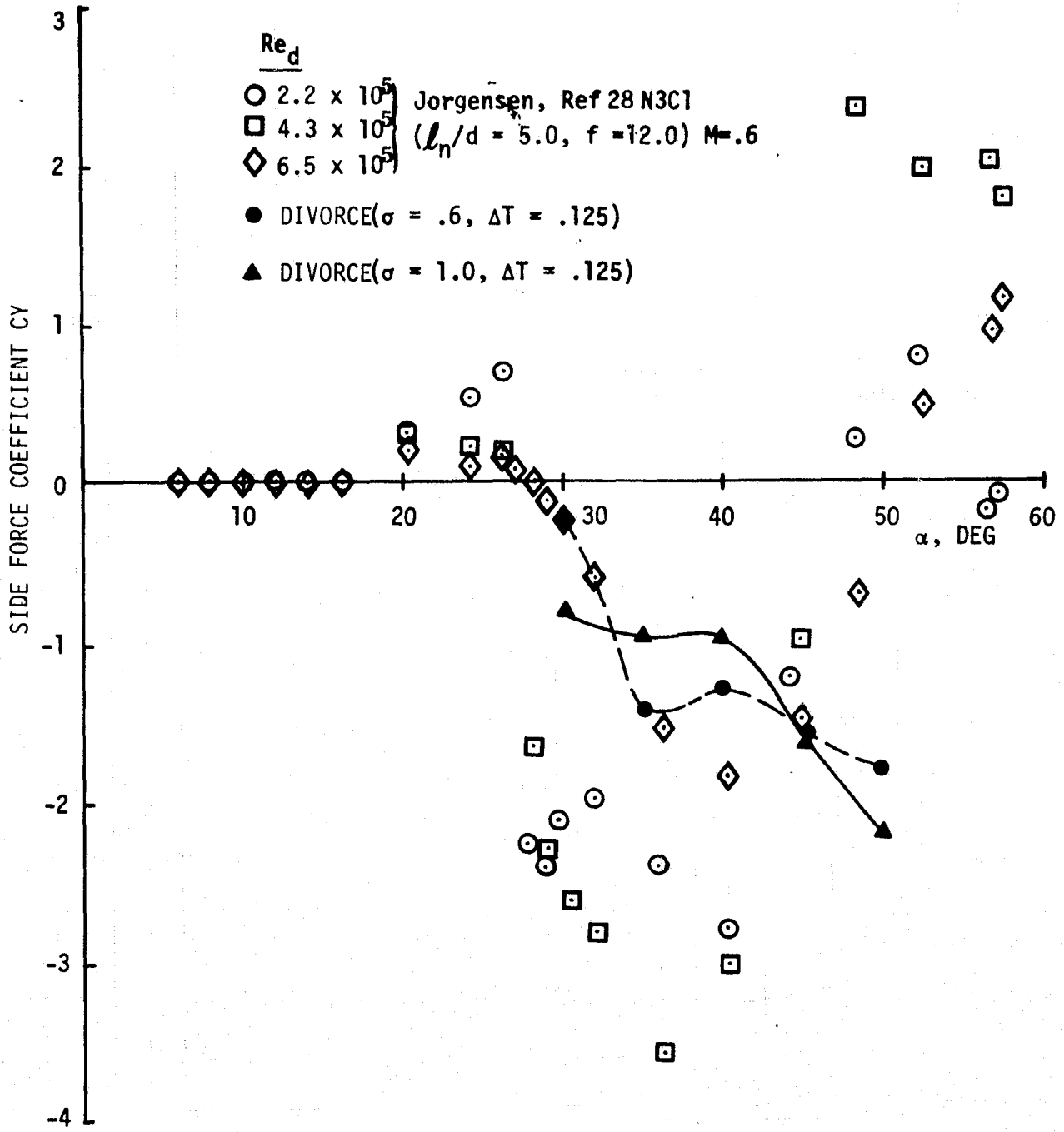

FIGURE 5-20 EFFECT ON VORTEX STRENGTH PARAMETER, σ, ON N3C1 SIDE FORCE

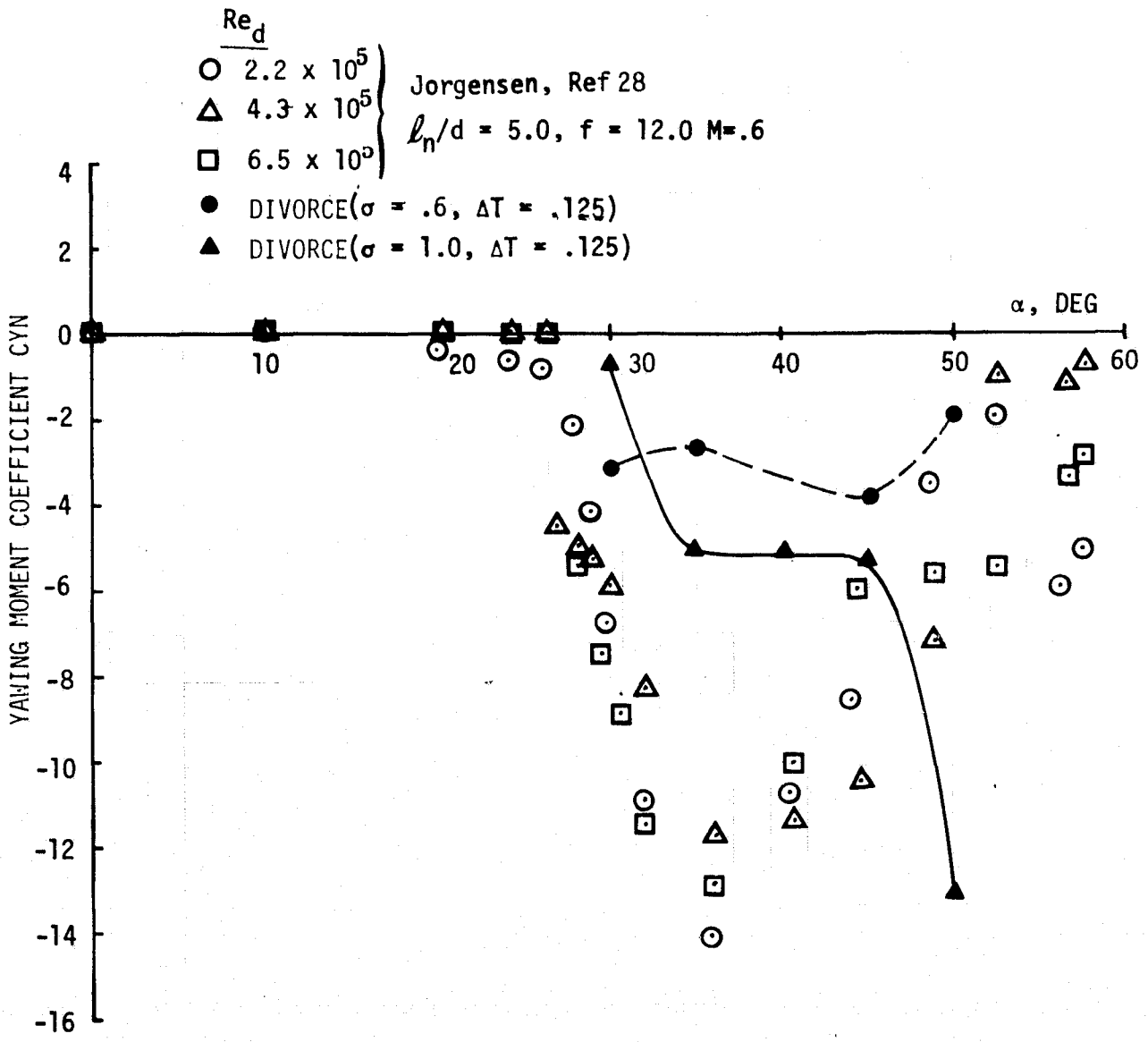

FIGURE 5-21 EFFECT OF VORTEX STRENGTH PARAMETER, σ, ON N3C1 YAWING MOMENT

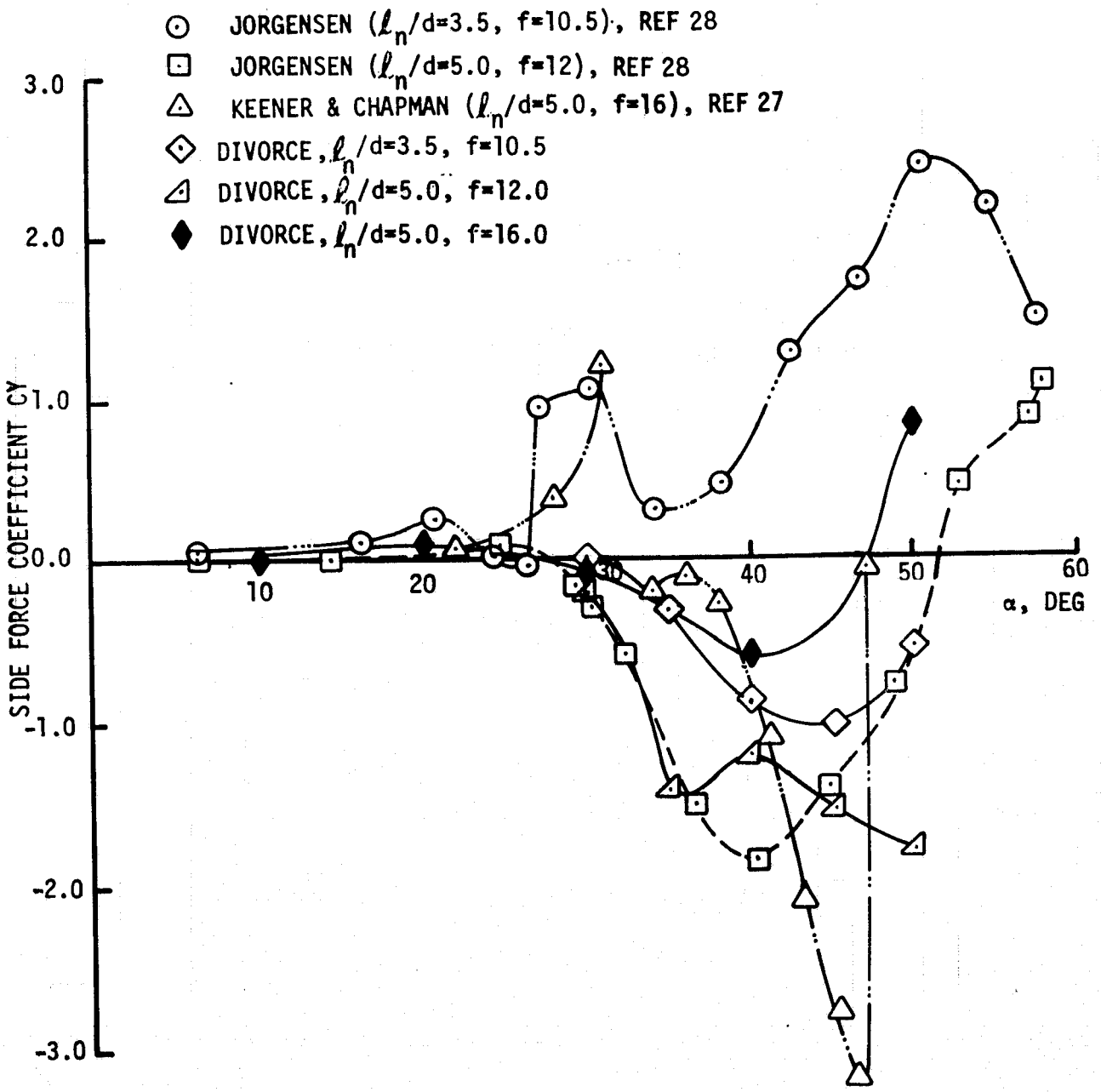

FIGURE 5-22 EFFECT ON FINENESS RATIO ON SIDE FORCE COEFFICIENT

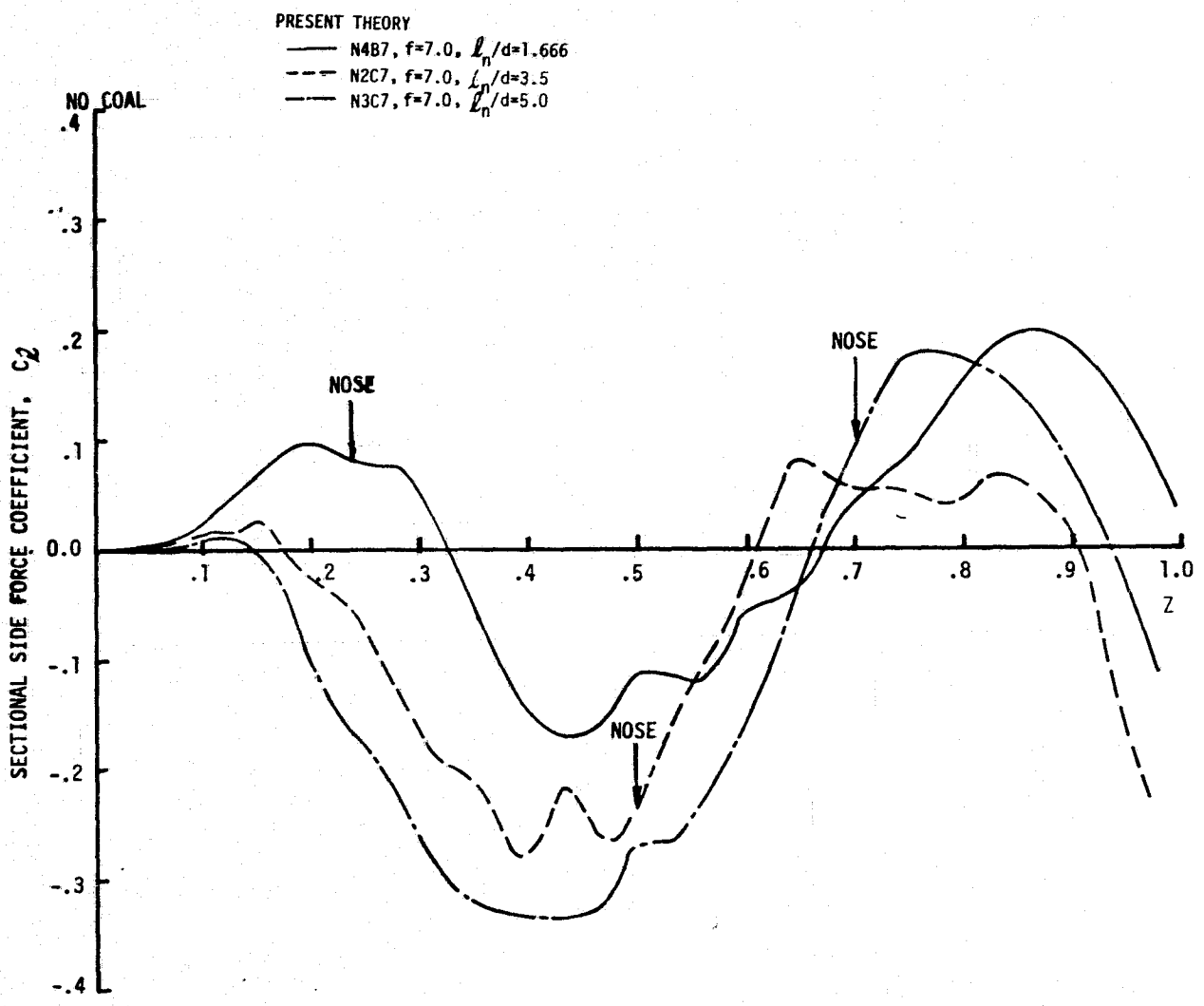

FIGURE 5-23 EFFECT OF OGIVE NOSE FINENESS RATIO ON SIDE FORCE DISTRIBUTION, α = 45°

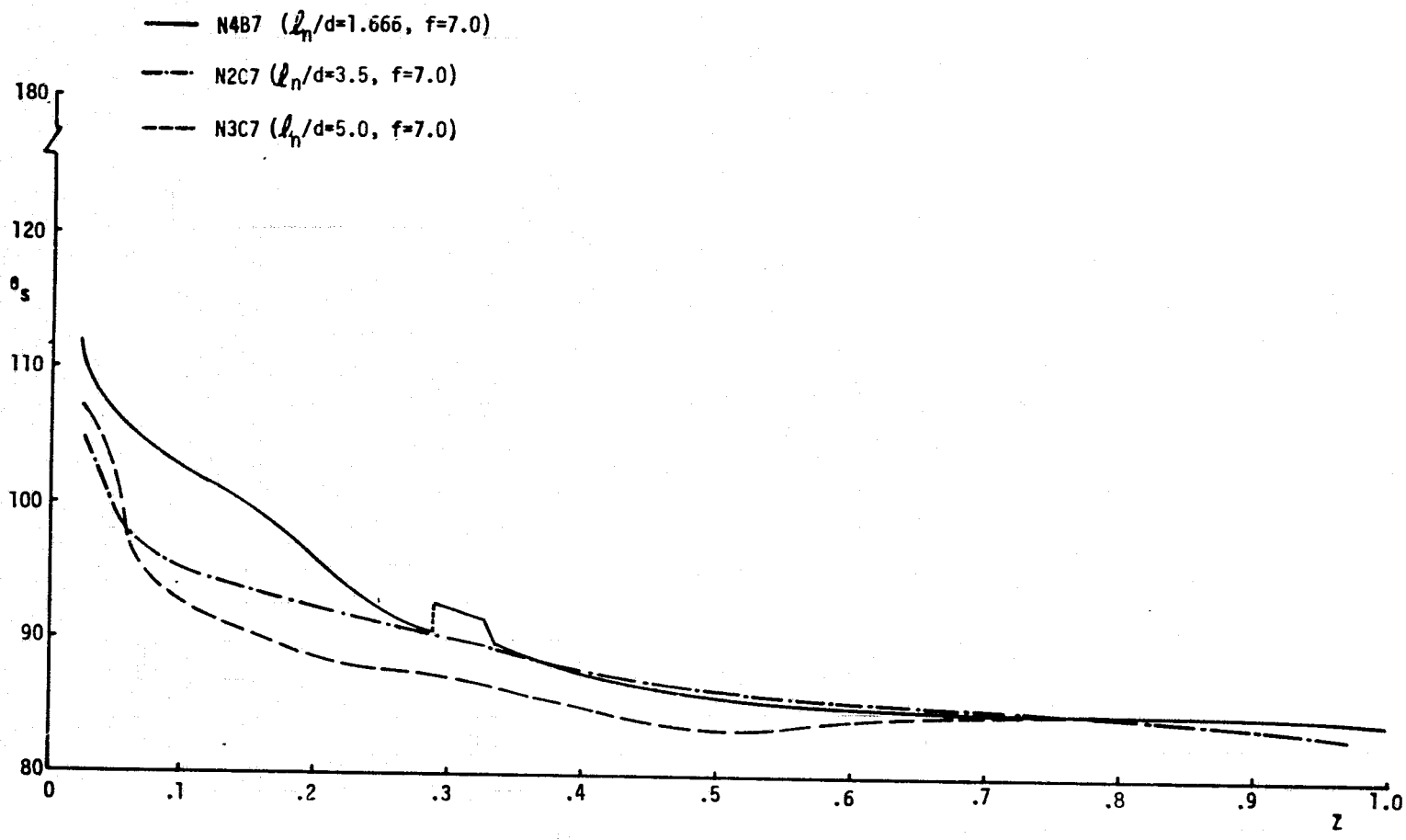

FIGURE 5-24 EFFECT OF OGIVE NOSE FINENESS RATIO ON SEPARATION ANGLE

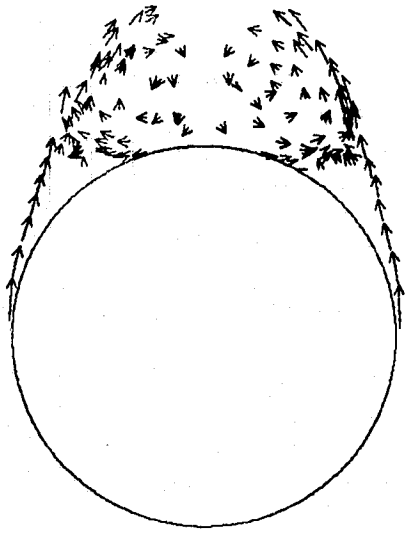

N4B7 ($\ell_{n/d}$ = 1.666)

Z = .236

N3C7 ($\ell_{n/d}$ = 5.0)

Z = .208

FIGURE 5-25 EFFECT OF NOSE FINENESS RATIO ON VORTEX DEVELOPMENT

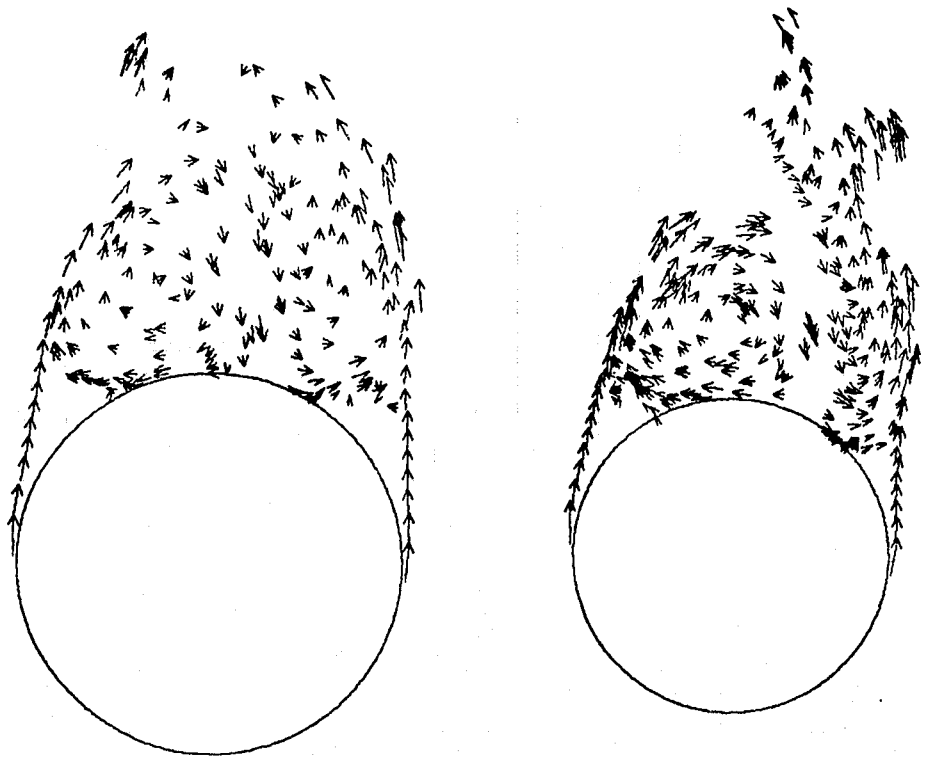

N4B7
Z = .414

N3C7
Z = .413

FIGURE 5-25 CONTINUED

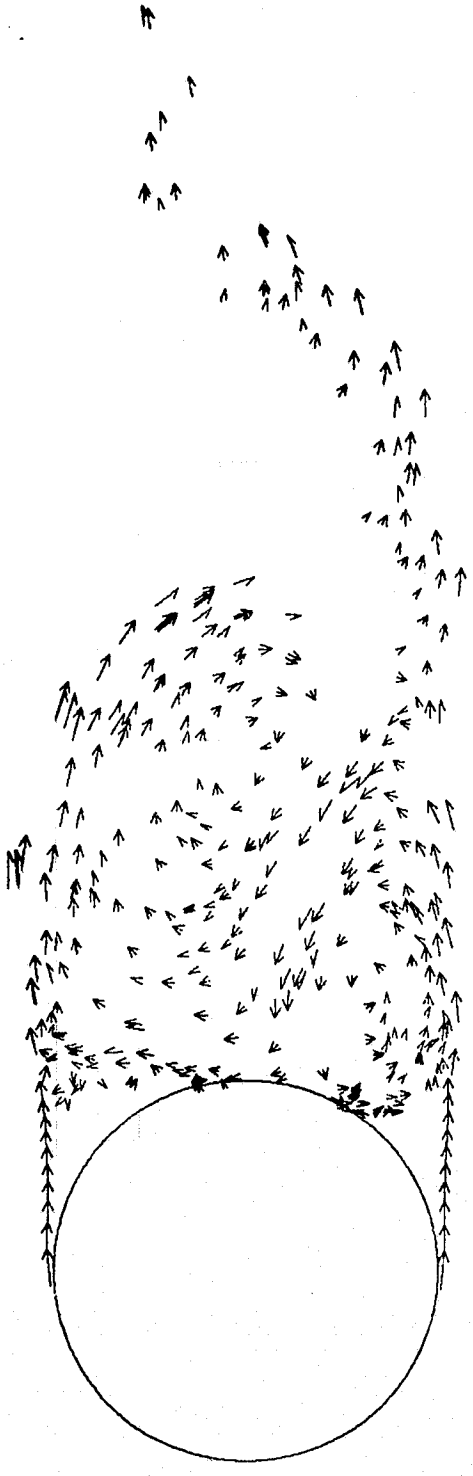

N4B7
Z = .771

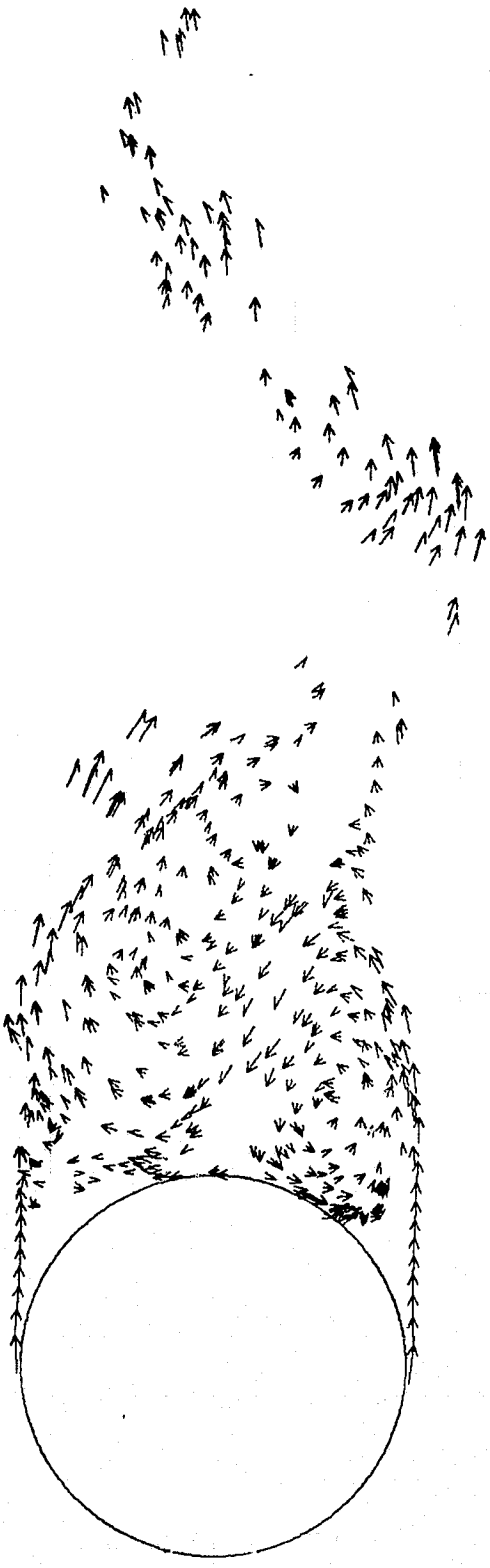

N3C7
Z = .749

FIGURE 5-25 CONTINUED

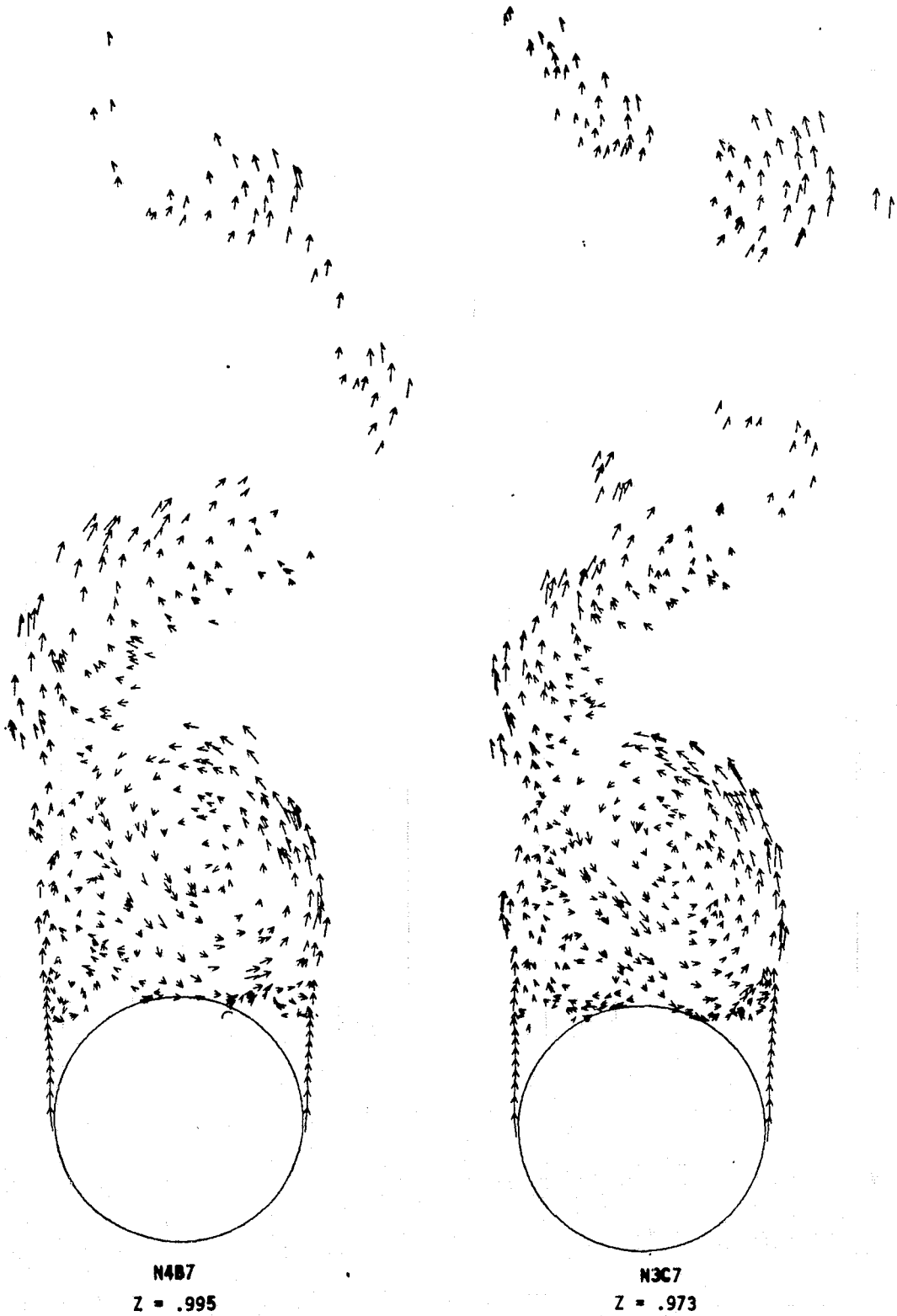

FIGURE 5-25 CONTINUED

DIVORCE (σ=.6, $\Delta\sigma$=.1σ, ΔT=.125) ℓ_{ref}=16.378 inches

CASE 350 (ℓ_n/d=5.0, ℓ=16.378 in, f=16.0) Z_1=.05, Z_2=.25, Z_0=.01, CY=.816, CN=6.904

CASE 2004 (ℓ_n/d=5.0, ℓ=14.843 in, f=12.0) Z_1=.022, Z_2=.109, Z_0=.00435, CY=-1.803, CN=5.085

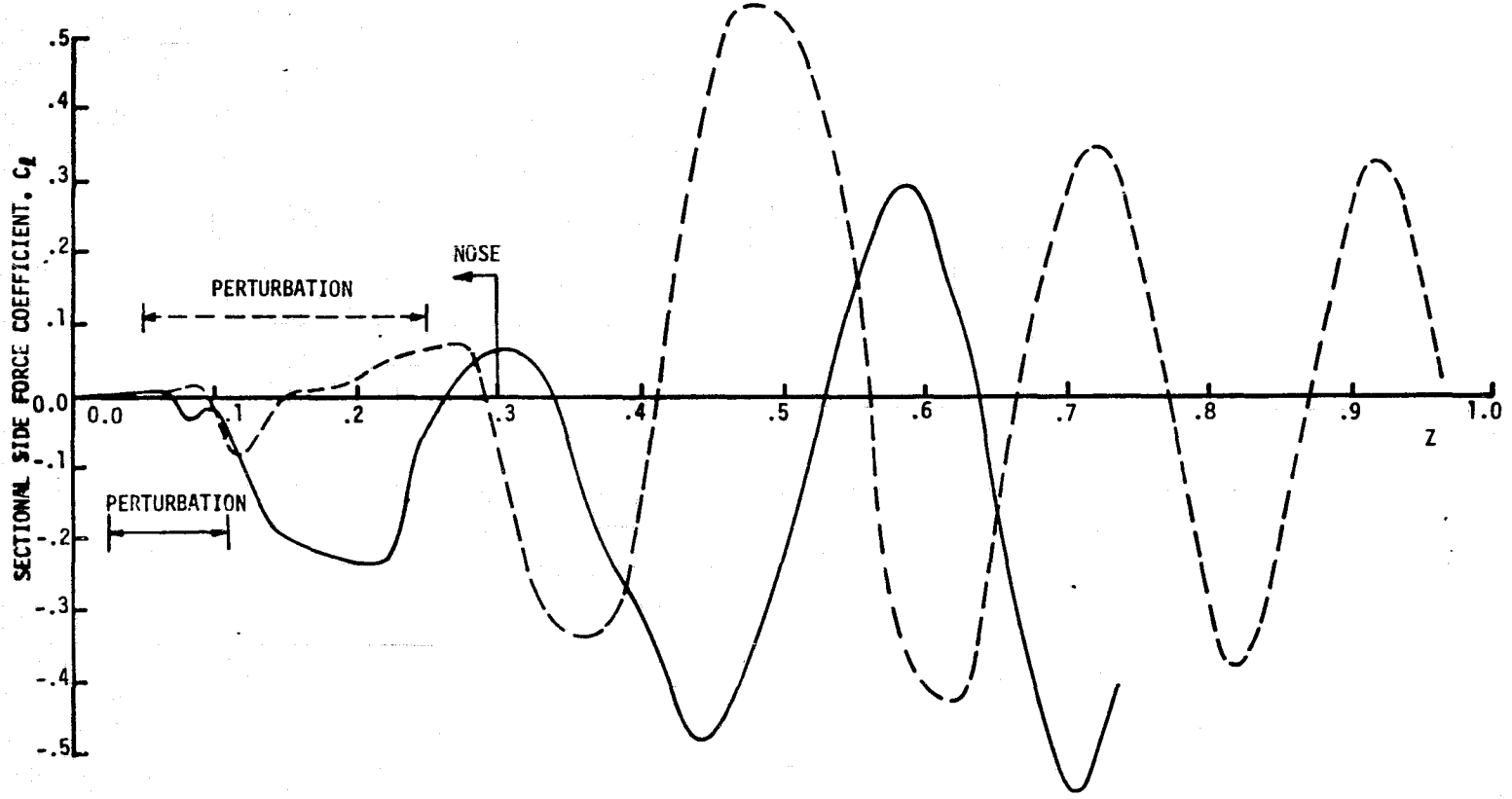

FIGURE 5-26 EFFECT OF PERTURBATION ON N3C (ℓ_n/d=5.0, f=12.0, 16.0) SIDE FORCE DISTRIBUTION (α=50°)

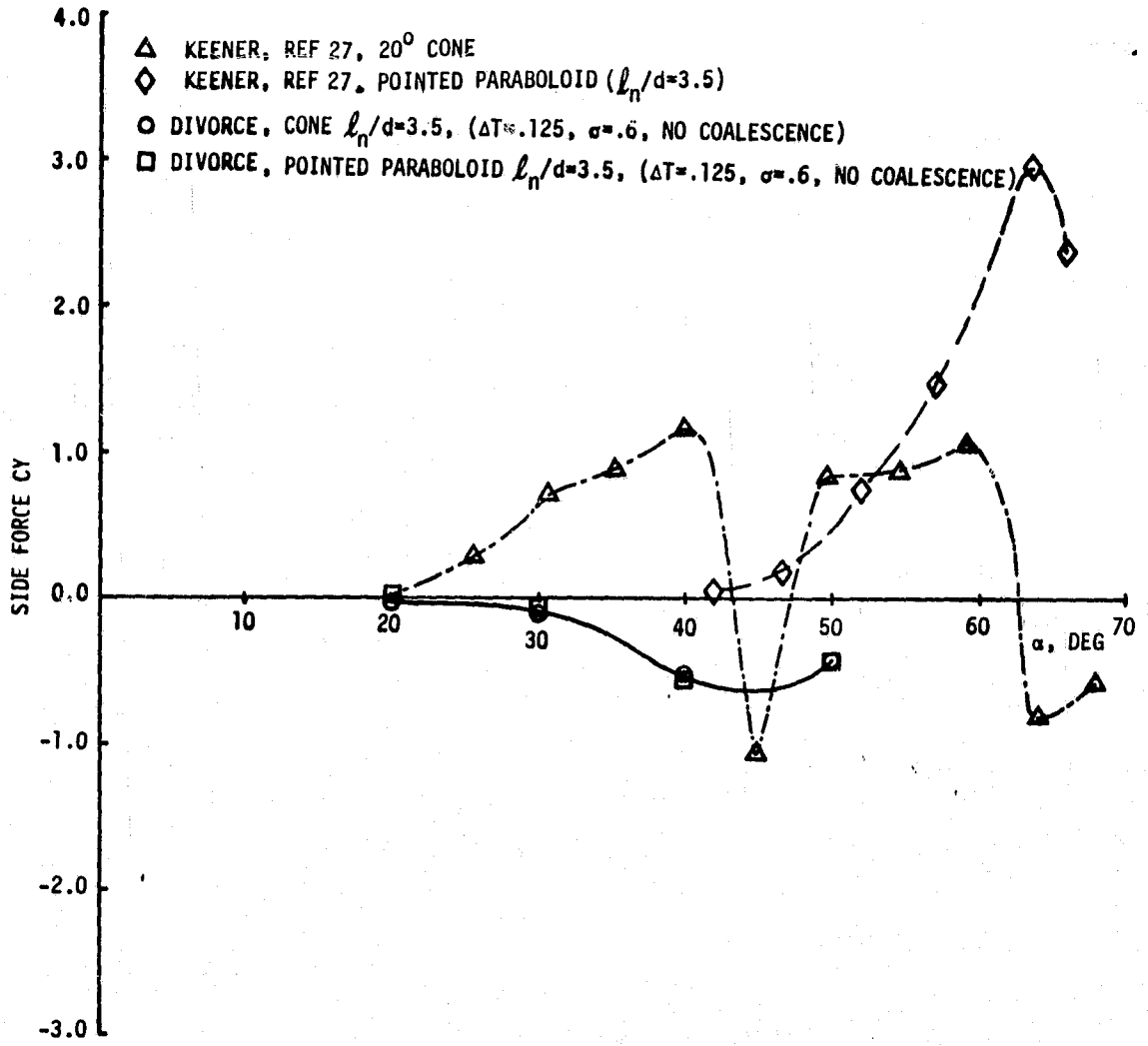

FIGURE 5-27 EFFECT OF FOREBODY GEOMETRY ON SIDE FORCE

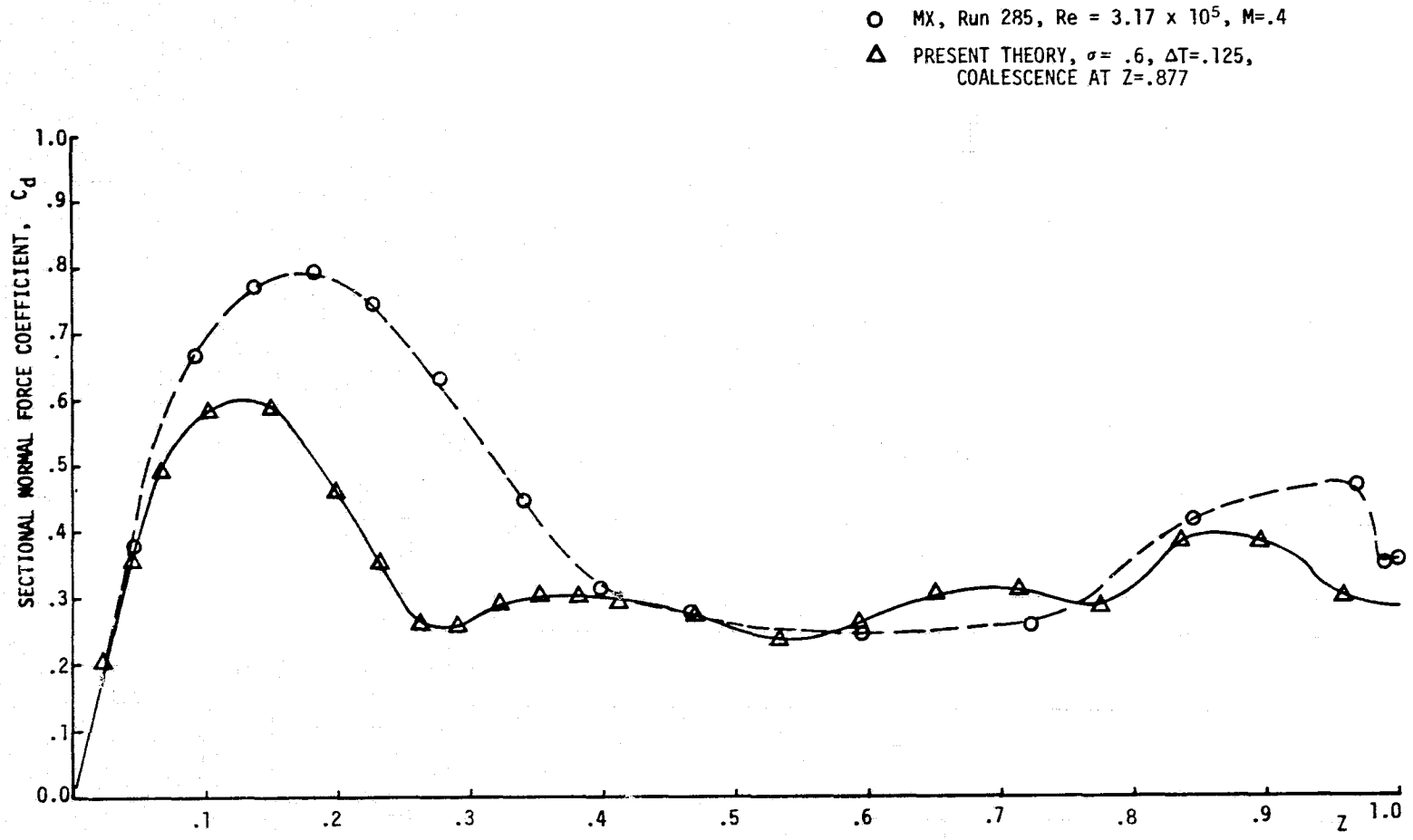

FIGURE 5-28 DISTRIBUTION OF NORMAL FORCE ON N1B1, α = 45°

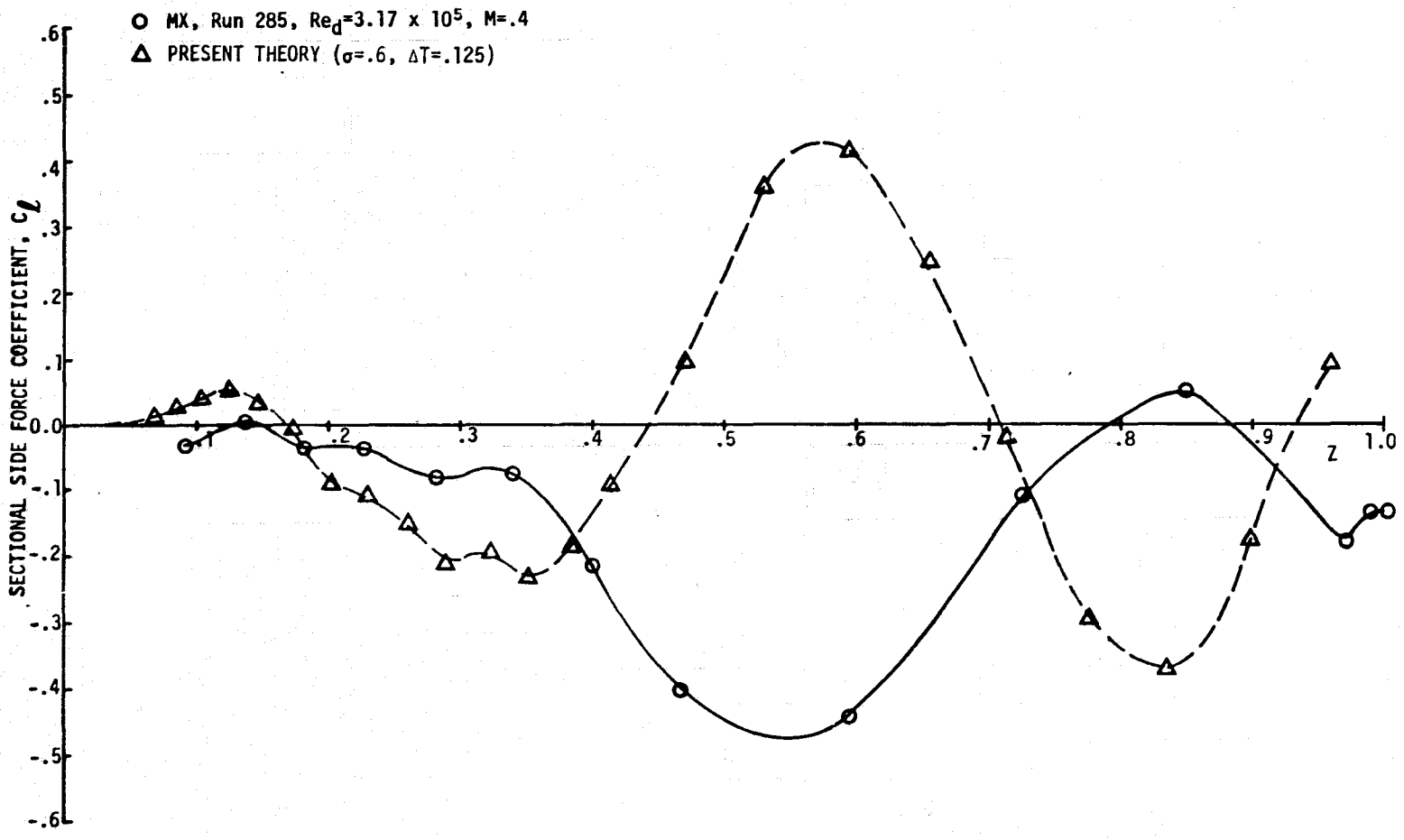

FIGURE 5-29 SIDE FORCE DISTRIBUTION, α = 45°

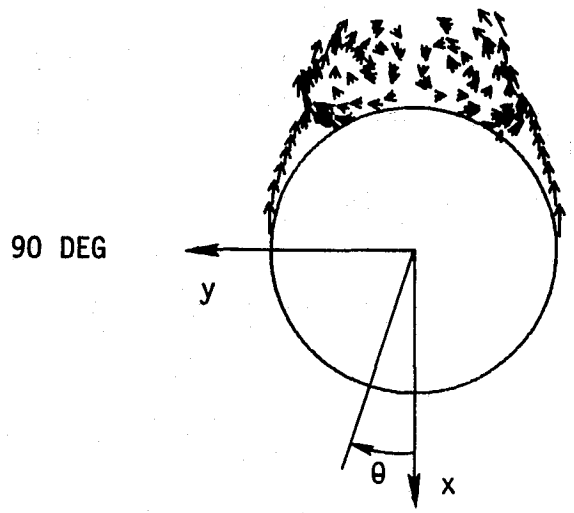

N1B1(Z=.124)
LOOKING UPSTREAM

FIGURE 5-30

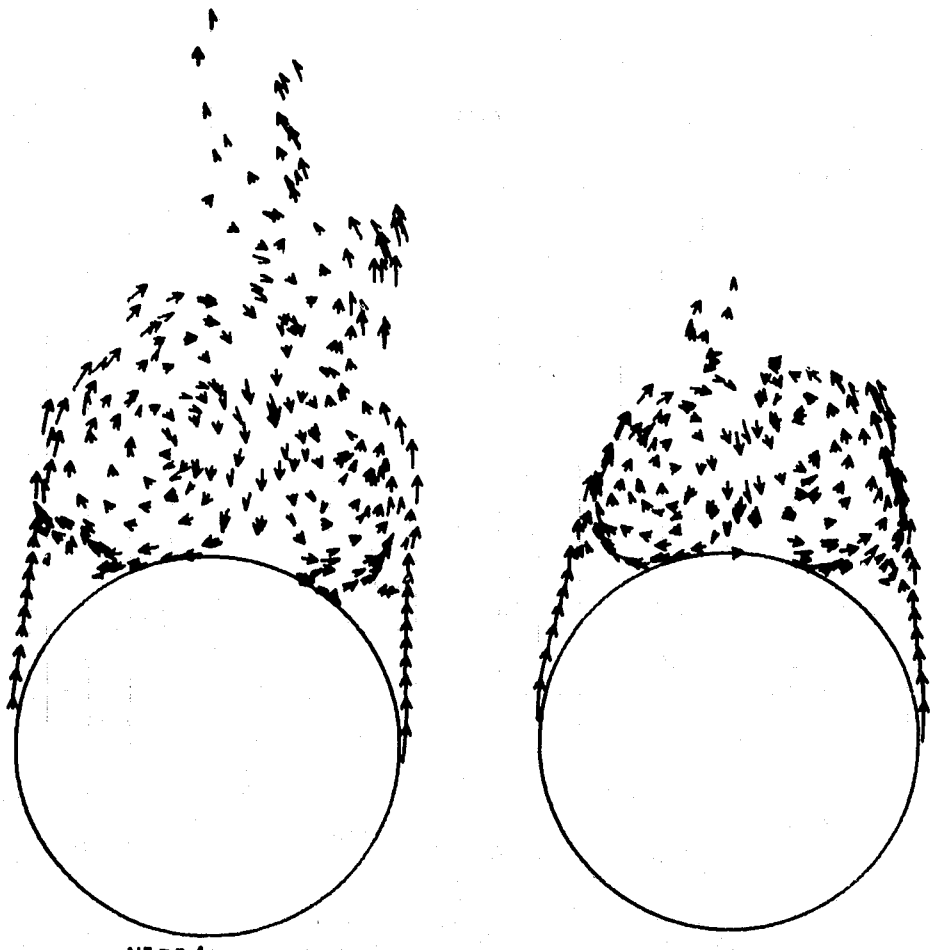

FIGURE 5-30 CONTINUED

N1B1(Z=.594)

FIGURE 5-30 CONTINUED

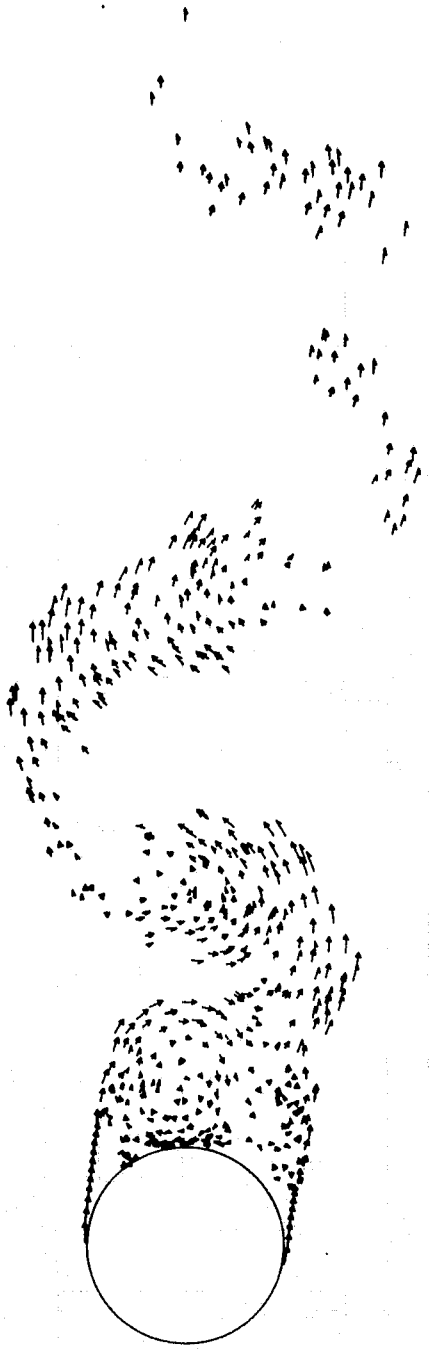

N1B1 (Z = .835)

FIGURE 5-30 CONTINUED

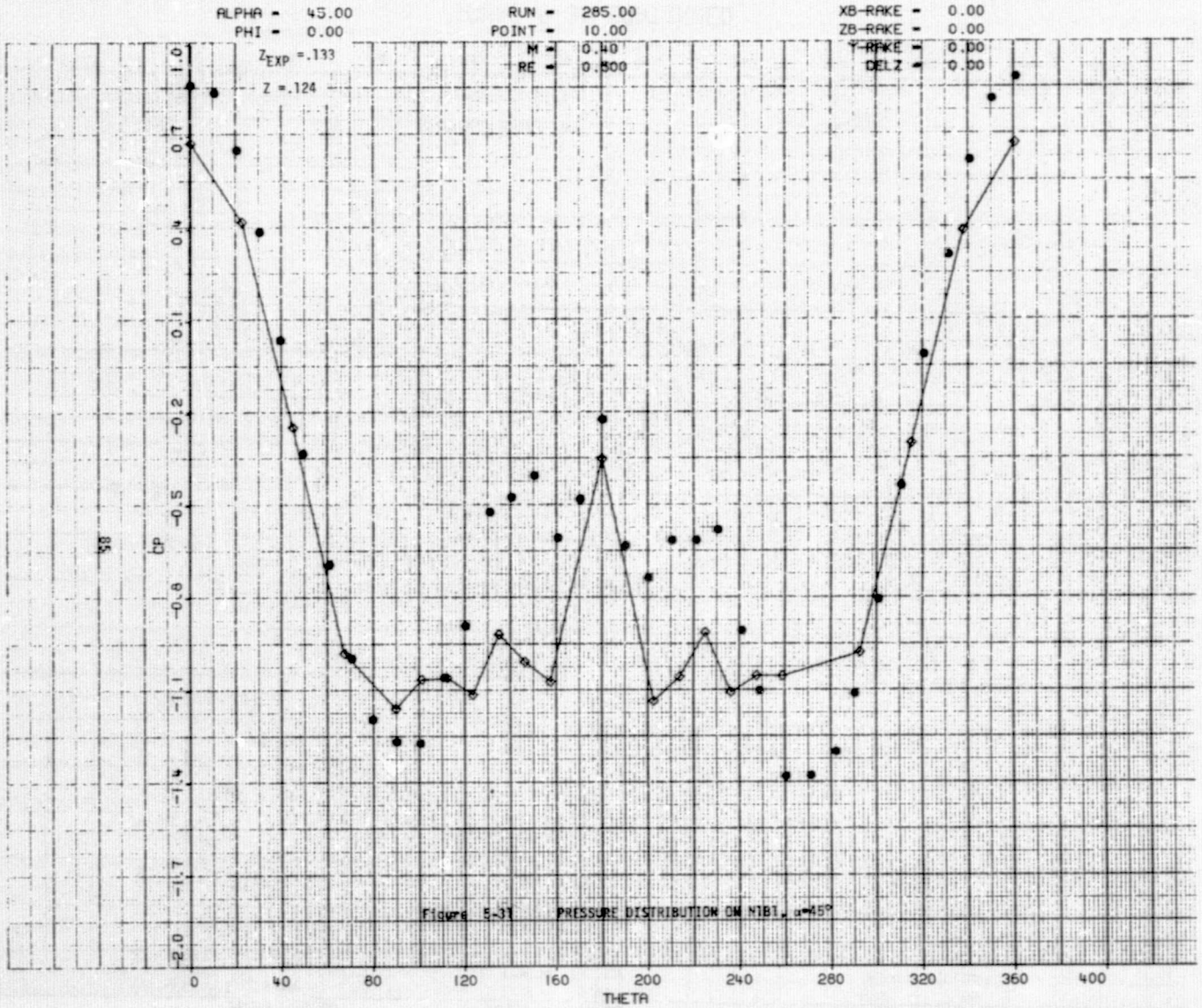

FIGURE 5-31 PRESSURE DISTRIBUTION ON N1B1, α = 45°

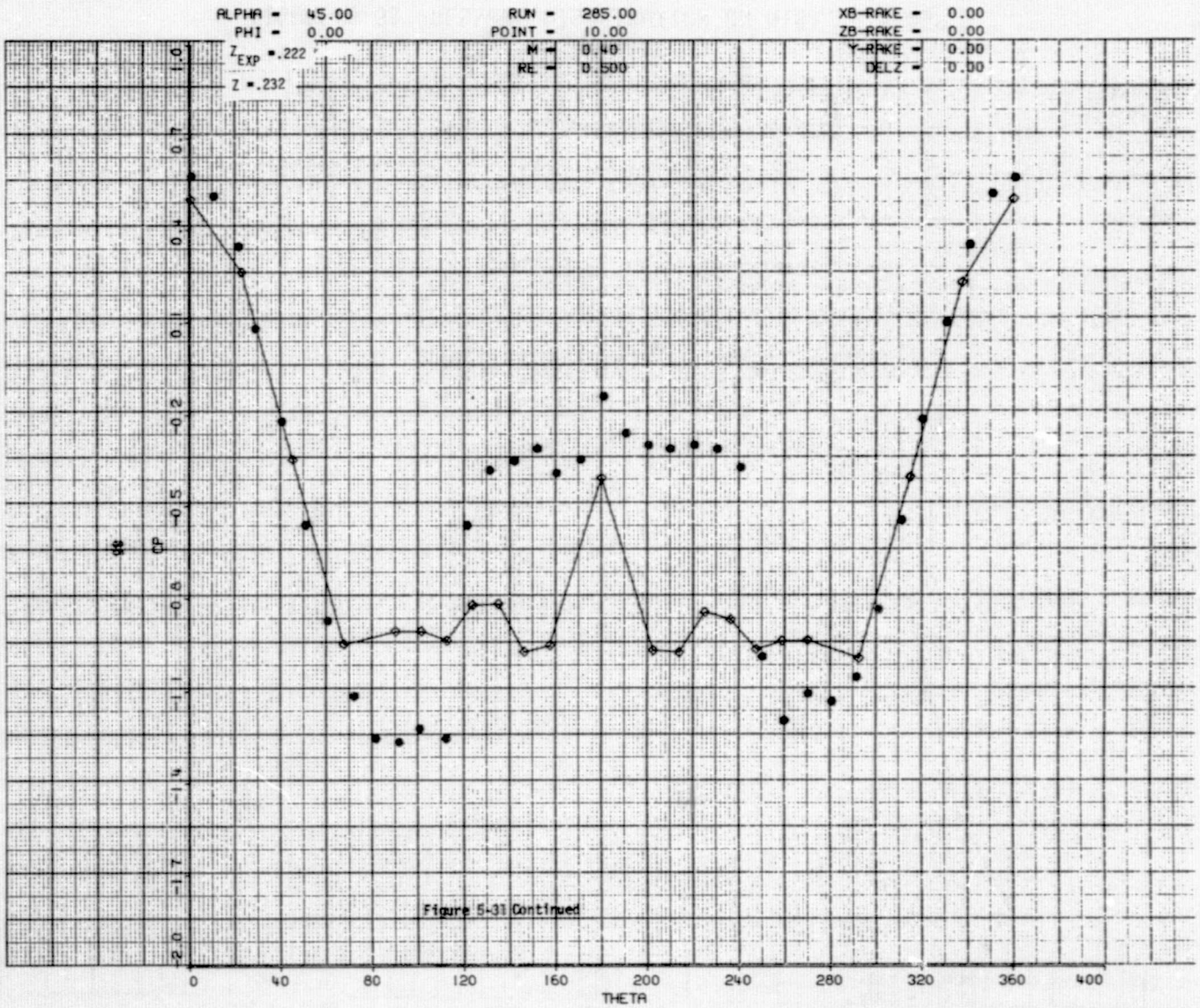

Figure 5-31 Continued

FIGURE 5-31 CONTINUED

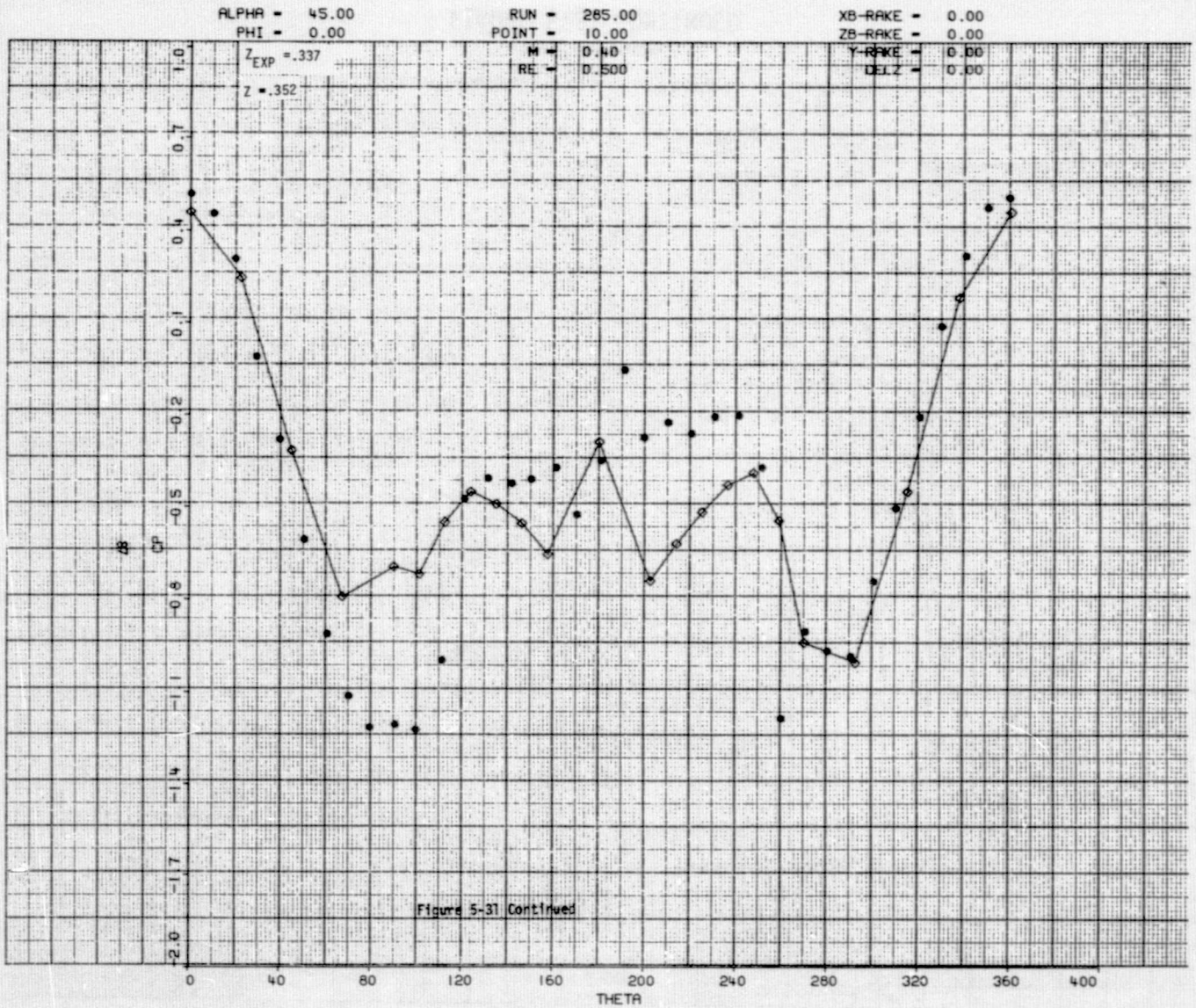

Figure 5-31 Continued

FIGURE 5-31 CONTINUED

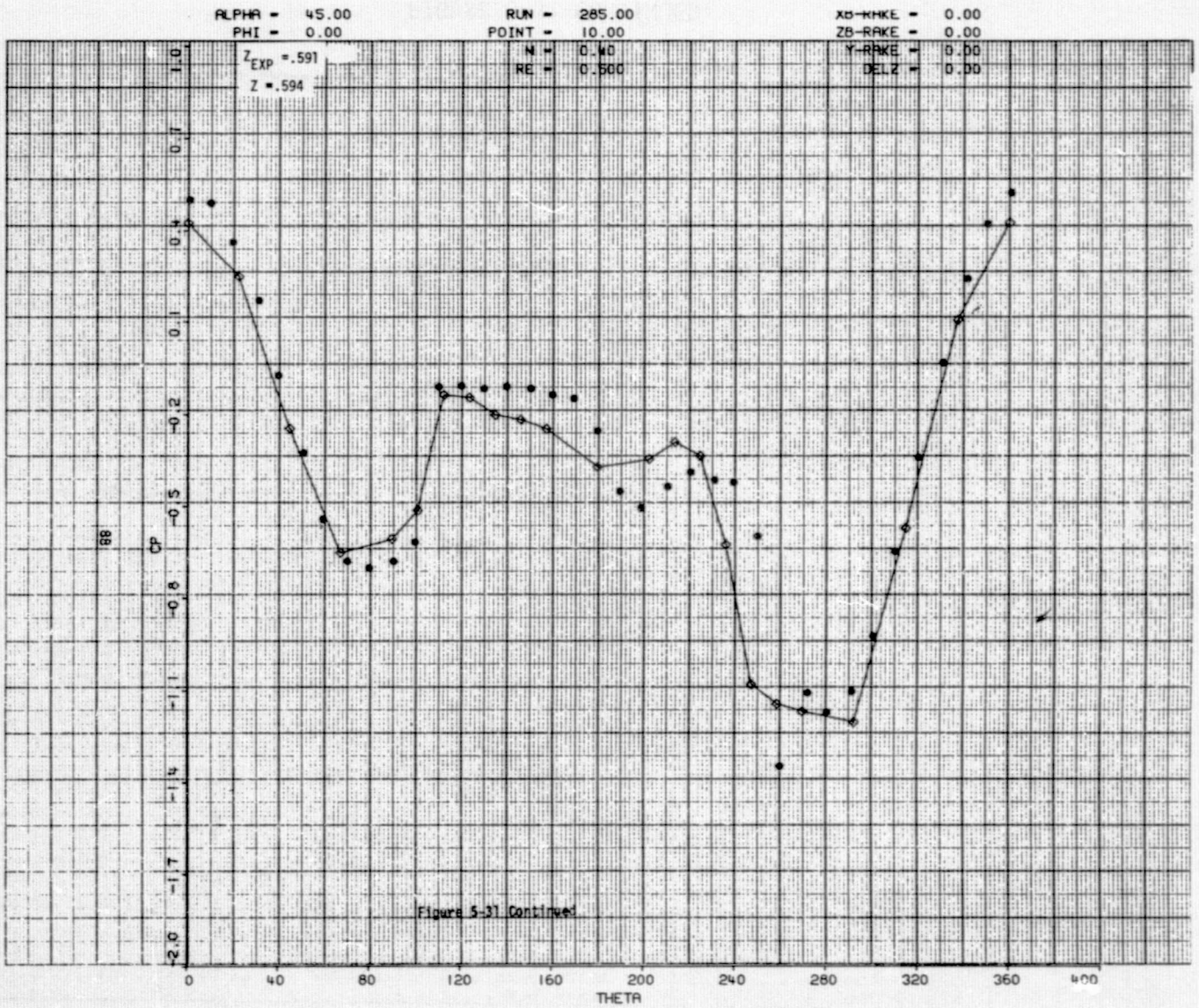

Figure 5-31 Continued

FIGURE 5-31 CONTINUED

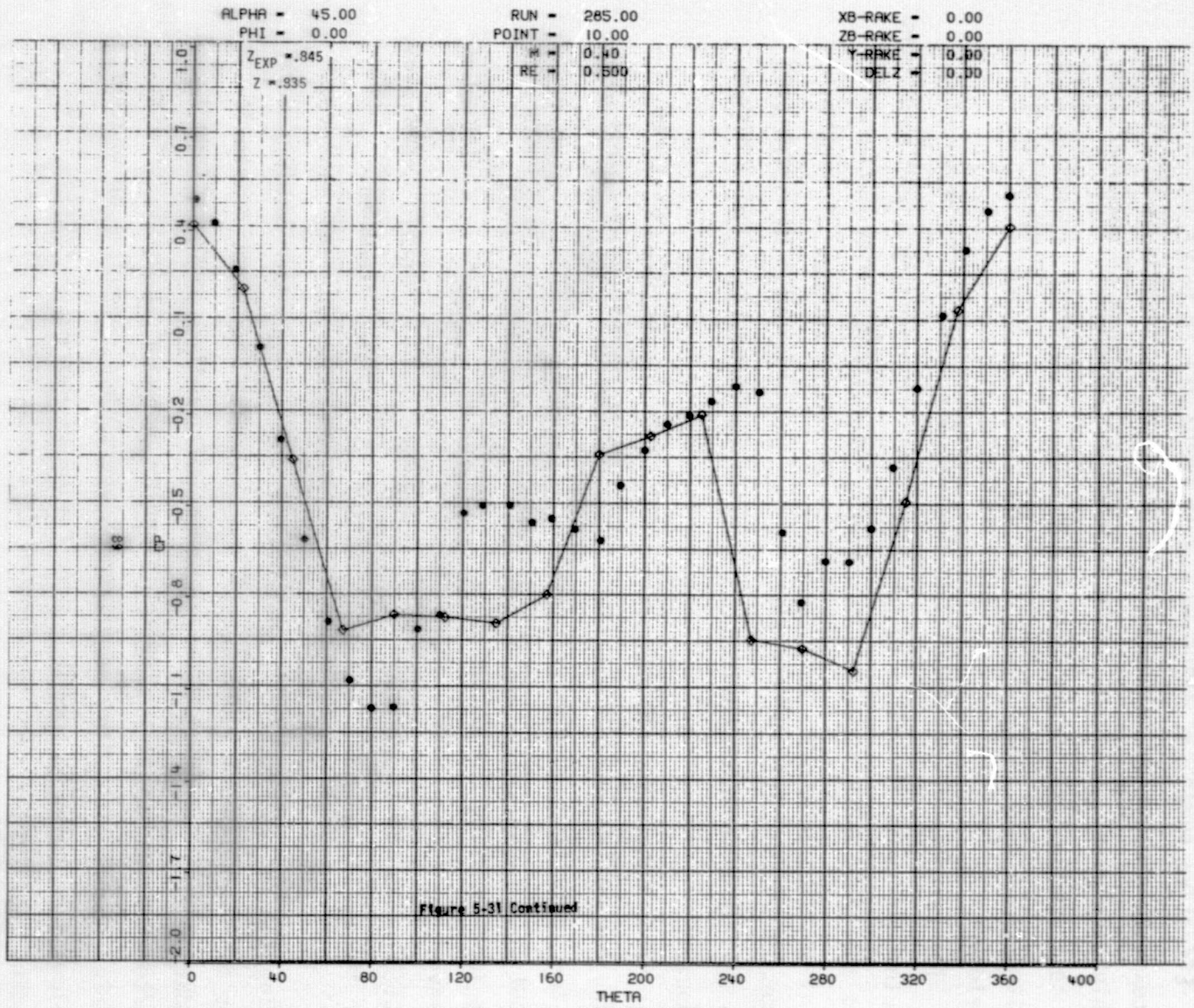

Figure 5-31 Continued

FIGURE 5-31 CONTINUED

6.0 DISCUSSION

Effective numerical algorithms were developed to apply the discrete vortex wake cross flow method of Ref. (9) to high fineness ratio bodies at high angles of attack of 30 to 50 degrees. Because of computer time and cost limitations the method had been used previously only on a very limited basis to demonstrate capability for predicting asymmetric wake development.

The required computational ability was achieved by (1) developing a method to solve the unsteady integral momentum boundary layer equations on a changing radius cylinder to replace the current finite difference solution, (2) restructuring the program to take advantage of Vector Processor Architecture in the vortex array computations, (3) optimizing the FORTRAN code which could not be vectorized, and (4) using a bigger computer.

After converting CDC6600 (RUNX) run times to CDC7600 run times using the optimizing FTN compiler, the increase in execution speed of the vectorized program over the original program was found to be about 30 percent. A 30 percent difference in execution speed alone does not justify using the method now, whereas it was too costly before. However, coupled with the increased speed of the CDC7600, over TRW's CDC6600, the method was able to be tested on various missile geometries, and the effect of numerical and empirical parameters examined.

Only about 12 percent decrease in computation time was achieved using the vector processing instruction set. Larger time savings were not achieved primarily because of two reasons. The first reason is linked to the fact that discrete vortex wake methods must include a vortex core radius to modify the singular behavior of point vortices. The vortex computations involve different operations depending on whether a calculation point is within a core radius of any point vortex. This core radius check interrupts the flow of data into the pipeline and results in minimal vector performance.

Probably 60% of the computation time is spent in the point vortex computations. The other 40% of the code could not be efficiently vectorized.

The FTN compiler optimizes CDC 7600 code very well. To gain speed over the very efficient serial code, a significant portion of the code may have to be vectorized.

The results obtained using the vectorized code, and the serial code were found to be slightly different. To examine this further, the serial program was stopped with about 1200 vortices in the flow. The vector program and the serial program were then started using the same 1200 vortex positions and strengths. The results were identical out to about the 12th significant digit. However, if the runs were continued for some time, slight differences would develop.

Predicted normal forces and moments in general agreed well with experiment. Increasing the vortex strength parameter, σ, resulted in better agreement with Jorgensen's (28) M = .6 data.

Probably the most significant aspect of the present work was the discovery of the extreme sensitivity of the side force development on the numerical and empirical parameters used in the method. Perhaps this result should not be surprising since experimental side force data is also extremely sensitive to perturbations in the flow.

Sarpkaya (29), in a recent experiment using a vertical water tunnel measured the time dependent drag and lift force acting on impulsively started circular cylinder. Experimentally Sarpkaya found that in impulsive flow the development of lift is strongly dependent on the initial disturbances which give rise to asymmetry and subsequent vortex shedding. In some runs Sarpkaya found that the vortices continue to grow symmetrically and result in small lift forces while for repeated runs at the same Reynolds number the asymmetry develops rapidly and the lift force not only starts at smaller values of t but also reaches larger amplitudes.

The predicted results of the present study indicated the same type of randomness in the early development of lift that Sarpkaya observed experimentally.

It is possible that the discrete vortex wake problem is not well posed, ie., a small change in the initial conditions result in a large change in the answer. However, it may be possible to bound the problem. By varying the parameters in the method within reasonable limits, it may not be possible to obtain a value larger than a certain maximum value.

7.0 CONCLUSION AND RECOMMENDATIONS

The viscous cross flow analogy was employed using a two dimensional discrete vortex wake cross flow solution to predict the flow field around high fineness ratio bodies of revolution at high angles of attack up to fifty degrees. A method was developed to solve the unsteady integral momentum boundary layer equations for the expanding radius circular cylinder started from rest in laminar flow. Since the integral momentum equation is valid for either laminar or turbulent flow, an extension of the present solution technique using a modification of Thwaites shape factor could be developed to extend the method to high Reynolds number turbulent flows.

Predicted normal forces and moments agreed well with experimental data. Predicted side forces and moments fell within the range of the experimental data but were found to be extremely sensitive to small perturbations. The maximum value of predicted side force was generally about half of the maximum experimental value. The predicted maximum values also occurred at different angles of attack.

The distribution of side force is mostly affected by the numerical perturbation applied to the method to induce asymmetric vortex development and by the vortex strength parameter. Increasing the vortex strength parameter always results in an increase in normal force coefficient, but not necessarily in side force coefficient. A physical explanation of the vortex strength parameter may be found by considering that the probability that only part of the total vorticity shed from a three dimensional separation line ends up in the cross flow plane. Experimental and theoretical investigations of the three dimensional flow separation on a typical missile shape needs to be undertaken to determine the cross flow component of vorticity.

Forcing a small asymmetric change in the strength of the newly introduced vortices for a portion of the missile nose has a significant effect on the side force development. Forcing the separation angles to be slightly asymmetric would be a similar perturbation mechanism. The

C-2

initial disturbance may be due to asymmetries which develop first in the wake (ie., free stream turbulence) and then feed back to the boundary layer. The physics of the initial instability needs to be better understood in order to determine how to model the initial disturbance.

REFERENCES

1 Allen, J. J., and Perkins, E. W., "A Study of Effects of Viscosity on Flow Over Slender Inclined Body of Revolution," Rept. 1048, 1951, NASA.

2 Jorgensen, Leland H., "Prediction of Static Aerodynamic Characteristics for Space-Shuttle-Like and other Bodies at Angles of Attack from 0^{0} to 180^{0}," NASA TN D-6996, Jan. 1973.

3 Jorgensen, Leland H., "A Method for Estimating Static Aerodynamic Characteristics for Slender Bodies of Circular and Non-Circular Cross Section Alone and with Lifting Surfaces at Angles of Attack from 0^{o} to 90^{0}," NASA TN D-7228, April 1973.

4 Jorgensen, Leland H., "Prediction of Static Aerodynamic Characteristics for Slender Bodies Alone and With Lifting Surfaces to Very High Angles of Attack," NASA TR R-474, Sept. 1977.

5 Saffel, B. F. Jr., Howard M. L., and Brooks, E. N. Jr., "Method For Predicting the Static Aerodynamic Characteristics of Typical Missile Configurations for Angles of Attack to 180 degrees, "NSRDC Report 3645, March 1971.

6 Thompson, K. D., "The Estimation of Viscous Normal Force, Pitching Moment, Side Force and Yawing Moment on Bodies of Revolution of Incidences Up to 90^{0}," WRE-Rep.-782 (Wr&D), Australian Defense Scientific Service, Melbourne, Aus., Oct. 1972.

7 Sarpakaya, T., "Separated Flow About Lifting Bodies and Impulsive Flow About Cylinders," AIAA J., Vol. 4, No. 3, Jan.-April, 1966, pp. 414-420.

8 Angelucci, S. B., "A Multivortex Method for Axisymmetric Bodies at Angle of Attack," Journal of Aircraft, Vol. 8, No. 12, Dec. 1971, pp. 959-966.

9 Marshall, F. J. and Deffenbaugh, F. D., "Separated Flow Over Bodies of Revolution Using an Unsteady Discrete-Vorticity Cross Wake. Part 1-Theory and Applications," NASA CR-2414, June 1974.

10 Wardlaw, A. B., "Multivortex Model of Asymmetric Shedding on Slender Bodies at High Angles of Attack," AIAA Paper No. 75-123, Pasadena Ca., Jan. 20-22, 1975.

11 Deffenbaugh, F. D., and Koerner, W. G., "Asymmetric Vortex Development on Missiles at High Angles of Attack," AIAA Journal of Spacecraft and Rockets, Vol. 14, No. 3, March 1977, pp. 155-162.

12 Saffman, P. G., and Baker G. R., "Vortex Interactions", to appear in Annual Reviews of Fluid Mechanics.

13 Dushane, T. E., "Convergence for a Vortex Method for Solving Eulers equations." Math. Comput. Vol. 27, 1973, pp. 719-728.

14 Hanson, F. G., Kozak, S. H., and Richardson, P. D., "Velocity Spikes in Separated Flows," J. Fl. Mech. Vol. 25, Part 1, May 1966, pp. 43-50.

15 Fage, A. and Johansen, F. C., "The Structure of Vortex Sheets," R & M 1143, Brit. Arc., 1927.

16 Hall, M. G., "A Numerical Method for Calculating the Unsteady Two Dimensional Laminar Boundary Layer," Ing-Arch, Vol. 38, 1969, pp. 558-586.

17 Stratford, B. S., "The Prediction of Separation of the Turbulent Boundary Layer," Ingenieur-Archivum, Vol. 38, 1969, pp. 97-106.

18 Rosenhead, L. (ed.), Laminar Boundary Layers, Oxford University Press 1963, pp. 324-329.

19 Thwaites, B., "On the Momentum Equation in Laminar Boundary Layer Flow. A New Method of Uniparametric Calculation," R & M 2587, Brit. Arc, 1952.

20 Thwaites, B., "Investigations into the Effect of Continuous Suction on Laminar Boundary-Layer Flow Under Adverse Pressure Gradients," R & M 2514, Brit. Arc, 1952.

21 Thwaites, B., "On the Flow Past a Flat Plate With Uniform Suction," R & M 2431, Brit. Arc., 1952.

22 Thoman, D.C., and Szewczyk, A. A., "Time-Dependent Viscous Flow Over a Circular Cylinder," Phys. Fluids Supp. II, 1969, pp. 1176-1186.

23 Mendenhall, R. M., and Spangler, S. B., "Further Studies of Aerodynamic Loads at Spin Entry." ONR Report CR212-225-3, 1977.

24 Einstein, S., "A High-Speed Software Vector Processing Subroutine Library for the Control Data Corporation 7600," RDA Report TR-3400-001, Sept. 1977.

25 Brode, B., Brode, R., and Grass, O., "Description and Use of RDALIB," R & D Associates Unpublished Report.

26 Baker, D. C., and Reichenau, D. E. A., "Aerodynamic Characteristics of an MX Missile at Free-Stream Mach Numbers from .3 to 1.3 and Angles of Attack up to 180 Deg," AEDC-TR-75-34, April 1975.

27 Keener, E. R., and Chapman, G. T., "Effects of Mach Number and Afterbody Length on Onset of Asymmetric Forces on Bodies at Zero Sideslip and High Angles of Attack," AIAA Paper No. 76-66, AIAA 14th Aerospace Sciences Meeting, Washington, January 26-28, 1976.

28 Jorgensen, L. H., and Nelson, E. R., "Experimental Aerodynamic Characteristics for a Cylindrical Body of Revolution with Various Noses at Angles of Attack From 0^0 to 58^0 and Mach Numbers From .6 to 2.0." NASA TMX - 3128, Dec. 1974.

29 Sarpkaya, T., "Impulsive Flow About a Circular Cylinder", Naval Postgraduate School Report, NPS-69SL-78-008, Monterey, California, March 1978.